Static Recrystallization Behaviour of AISI 304 Stainless Steel during Hot Rolling Intervals

A thesis submitted to the Faculty of Engineering and the Built Environment, University of Cape Town, in fulfilment of the requirements for the degree of Master of Science in Engineering

By
Martin Sheen
Centre for Materials Engineering
2001

Acknowledgements

I wish to thank all those who have assisted me throughout this project, but in particular:

My supervisor, Professor R.D. Knutsen, for his valuable guidance and encouragement.

Columbus Stainless for their financial and practical support, in particular Altus Jordaan for his prompt and informative replies to the many questions regarding hot rolling.

The University of Pretoria, IMMRI, for the use of the Gleeble 1500.

The financial support provided by the NRF is greatly appreciated.

Janet Basson for her encouragement and the many hours spent discussing material processing.

Glen Newins for the meticulous specimens that he prepared.

Julie-Ann Henry, thanks for all the administrative support and your constant sense of humour.

James Buchanan for his assistance with finite element modelling applications.

The staff and students in the Centre for Materials Engineering for their assistance, good humour and motivation.

To Claire for her boundless support.

Dedicated to my family.

Abstract

Modelling microstructural evolution during industrial hot rolling is beneficial to the manufacturer as it enables improved quality control and an increase in productivity. It is, however, a complex problem to develop an online model that can accurately predict microstructural evolution for all conditions encountered during the production process. There is on-going research on this topic to develop and improve the modelling process for hot rolling applications. Columbus Stainless initiated this project to obtain an improved understanding of the modelling process and to develop a protocol for modelling any particular material. Thus, this study was not aimed at formulating predictive equations but rather at developing an approach for modelling a material's behaviour during rolling.

The Avrami equations have been used in this study to glean an understanding of the material's annealing behaviour following deformation. The deformation and annealing conditions were chosen to simulate the conditions encountered during the industrial hot rolling application. An important aspect of the modelling process is determining the extent of recrystallization that has occurred within the deformed material for a given annealing time. Hardness tests and Electron Backscattered Diffraction (EBSD) techniques were used in this study to measure the fraction of material recrystallized for given annealing times. The fraction material recrystallized versus annealing time data is a fundamental aspect in the modelling procedure. It enables the Avrami constants to be determined and provides valuable information on the material's annealing response for given deformation conditions and annealing temperatures.

Attempts to model the recrystallization behaviour has shown that the deformed state is of significant importance. Furthermore, high annealing temperatures resulted in rapid recrystallization kinetics and it was thus difficult to glean representative data of the microstructural response at these temperatures. It is proposed that in order to develop an online model based on the Avrami approach that an understanding between the mill operator and metallurgist is established. A single Avrami equation, with universal constants, cannot describe all of the conditions encountered during rolling and thus multiple equations, and certain conditions that cannot be described by an equation, need to be incorporated into an online predictive model.

Table of Contents

List of Abbreviations

AISI	American Iron and Steel Institute
SEM	Scanning Electron Microscope
EBSD	Electron Backscattered Diffraction
HAGB	High Angle Grain Boundary
RD	Rolling Direction
TD	Transverse Direction
ND	Normal Direction
RaD	Radial Direction
$t_{0.5}$	Time to 50% recrystallization
n	Avrami constant
Z	Zener-Hollomon parameter
FCC	Face Centred Cubic
FE	Finite Element
X_s	Volume fraction softened
X_v	Volume fraction recrystallized
σ_p	Peak stress
σ_s	Hypothetical saturation stress
ε_c	Critical strain for recrystallization
ε_p	Peak strain
ε_x	Strain required for completion of recrystallization
H_f	Hardness value at point of complete recrystallization

Chapter 1

Introduction

Hot rolling is an industrial application used to reduce a cast metal slab to either plate or sheet. During hot rolling operations the material is deformed in a series of passes and microstructural properties, which include grain size, stored energy and texture, are affected both during deformation and subsequent holding periods. The microstructure produced by the deformation process is unstable, due to the accumulation of dislocations, and softening mechanisms such as recovery and recrystallization are responsible for reducing the stored energy.

Control of microstructure during hot rolling has a significant effect on mechanical properties such as tensile strength, yield strength, elongation and toughness. The quality of the final rolled product is determined on the basis of the material properties satisfying the customer requirements. Thus it is desirable to control the thermo-mechanical conditions, which include strain, strain rate and temperature, to produce microstructures for optimal material properties. The mill operator has traditionally relied on obtaining samples during production to monitor the microstructural development for a particular rolling process. However, this method is expensive and time consuming. This necessitates the need to have a method whereby it is possible to predict the microstructure as a function of the deformation conditions via an on-line computer model. An on-line model would be able to control deformation conditions to satisfy the customer's material requirements efficiently without expensive plant trials being necessary. Other advantages of on-line prediction and control would be an increase in productivity, reduction in manufacturing costs and a support system in the diagnosis of processing irregularities.

The complexity of the deformation variables during industrial hot rolling requires careful attention. Temperature, strain and strain rate transients exist within the plate and directly influence microstructural evolution. Thus, microstructural, mechanical and temperature models are required to operate in tandem to effectively achieve fully automated on-line prediction. This study is concerned with the microstructural

aspects but it should be borne in mind that the accuracy of any predictive model will be dependent on the quality of the input data during the rolling process.

There are some well accepted algorithms, containing material dependent constants, that have been developed which describe the recrystallization kinetics of a material. However, there is often disagreement on the exact value of the constants and limited information has been published on the derivation method that was used to obtain the values. The purpose of this study was therefore to develop a suitable methodology for predicting the static recrystallization behaviour of AISI 304 stainless steel as a function of hot rolling conditions. The validity of the algorithms, for predicting microstructural evolution on an industrial scale, was also considered in terms of extending the model to predict microstructural evolution for different materials. Thus, it was not proposed that new algorithms would be developed to improve upon existing algorithms, but rather on establishing a procedure that could be followed to effectively model any particular material.

Chapter 2

Literature Review

2.1 Material

2.1.1 Introduction

The group of iron based alloys with a high chromium (Cr) content, not usually less than 11 weight percent (wt%) are classified as the stainless steels. Cr is essential in the stabilisation of the passive film and considerably enhances corrosion resistance in comparison to carbon (C) and low alloy steels[1]. In addition to excellent corrosion resistance, the following properties are also required of the stainless steels: ease of fabrication, excellent formability, weldability, good strength and toughness. Specific service conditions favour certain material requirements and this has led to the development of a series of stainless steel types. A convenient means for classification of the types of stainless steels is according to their crystallographic structure. The four principal types are categorized as ferritic, austenitic, martensitic and duplex stainless steels[2].

2.1.2 Austenitic Stainless Steels

The material under investigation was a face centred cubic (f.c.c.) AISI 304 austenitic stainless steel, with major alloy additions being Cr and nickel (Ni). Figures representing the Cr and Ni contents are commonly used to designate the various austenitic stainless steels, such as 18-8 or 18-10 (Cr-Ni respectively) for the most widely used grades[1]. The extensive engineering applications of the austenitic stainless steels are attributed to a number of desirable properties; excellent corrosion resistance being the most significant. Other properties include good formability, easily weldable, non-magnetic and the ability to handle both cryogenic and elevated temperature applications[3]. Typical examples of AISI 304 applications include piping in boiling water nuclear reactor, seagoing chemical tankers, heat exchangers and storage tanks for the wine industry[4].

2.1.3 Effect of Alloy Additions

The addition of Ni in sufficient quantities to stainless steel changes the crystal structure to austenite by enlarging the f.c.c. gamma loop, hence the term austenitic stainless steels. Ni also has the effect of decreasing the martensite start temperature to below room temperature so that stable austenite is retained after cooling from the solution-treatment regime to room temperature. Quenching to room temperature, therefore, cannot harden the austenitic stainless steels[5]. In addition to stabilising the austenitic structure, Ni also improves mechanical properties and fabrication characteristics. The influence of Ni and Cr on the structure of the austenitic stainless steels at high temperatures is shown in figure 2.1. Cr stabilises the ferrite (δ or α depending on temperature) and Ni stabilises the austenite (ϒ).

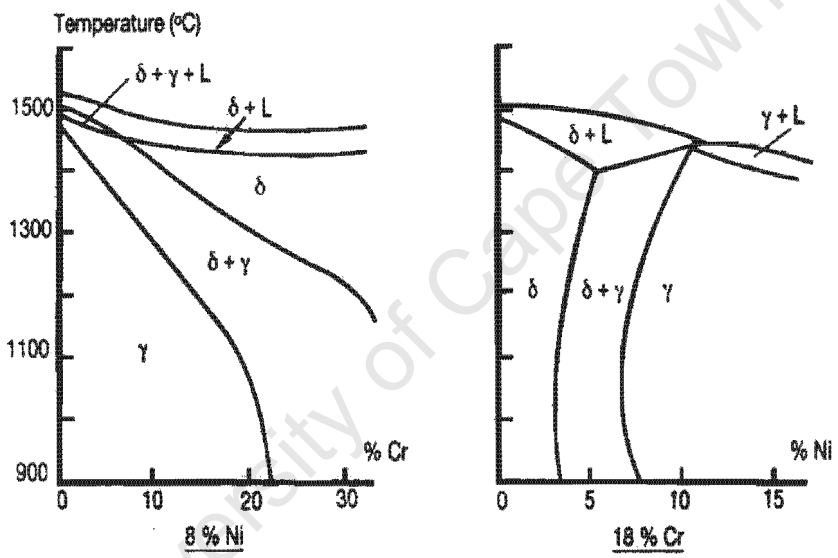

Figure 2.1: **Diagram showing the stabilising effect of Cr and Ni on ferrite and austenite respectively[1].**

2.1.4 Chromium-Carbides

Another strong austenite former is C, which is added in very small quantities to AISI 304 stainless steel. The solubility of C decreases as the stainless steel is cooled from high temperatures and this can lead to the formation of Cr rich carbides. The C in the stainless steel alloy combines with Cr in the ratio $M_{23}C_6$ and precipitates along grain and twin boundaries[1]. Figure 2.2 illustrates the appearance of $M_{23}C_6$ precipitates at grain boundaries in a 304 stainless steel. In deformed materials, dislocations provide favourable sites for intragranular precipitation[4]. The precipitation of $M_{23}C_6$ occurs when austenitic stainless steels are subjected to temperatures in the range of 480^0C to

815^0C. The extent of carbide precipitation depends on the time at precipitation temperature and the C content[1,4].

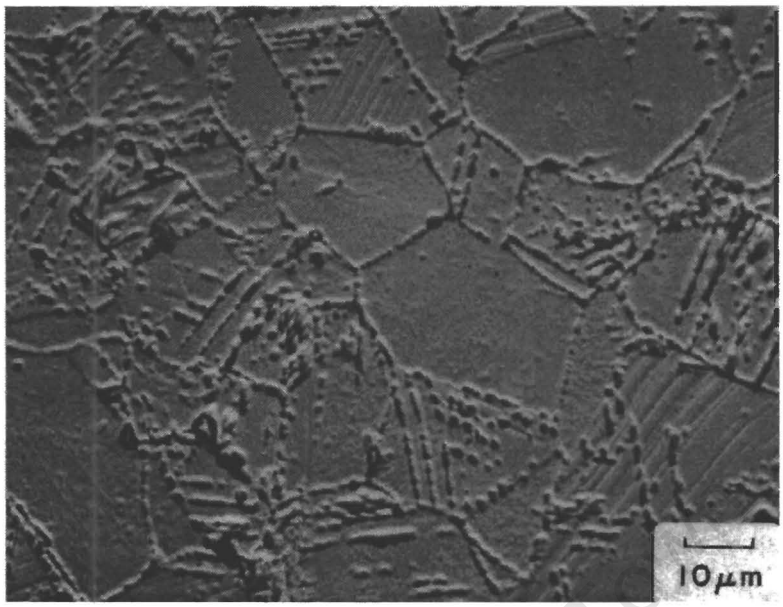

Figure 2.2: Microstructure of austenitic stainless steel type 304 with $M_{23}C_6$ precipitation at grain boundaries[4].

To prevent carbide precipitation, which is deleterious to the corrosion resistance as surrounding areas are depleted of Cr, the C content is minimised and should not exceed 0.08 wt% in austenitic stainless steels. Ideally, the C content should be reduced to below 0.03 wt%. However, the reduction in C content only delays the formation of carbides and precipitation can occur after extended exposure[6]. Solution annealing treatments (1100-1150^0C) will dissolve carbide precipitates and rapid quenching suppresses further precipitation[7]. The austenite formed at high temperatures is conserved at room temperature and the carbide precipitates are prevented from forming due to rapid cooling through the precipitation temperature range. However, on reheating in the range of 480 to 815^0C, $M_{23}C_6$ is reprecipitated[4,7].

2.1.5 Sigma Embrittlement

Sigma phase is a hard, brittle intermetallic compound that usually forms from ferrite but can also form directly from austenite. Sigma phase forms in the same temperature range as $M_{23}C_6$ but requires extended time at temperature (up to 1500 hours) for full development[7]. An increase in Cr above 20 wt% promotes sigma formation, with type 25Cr-20Ni-0.2C being the most prone austenitic stainless steel[4]. Ferrite forming

elements such as molybdenum and titanium further accelerate sigma phase formation. However, the times available during production processes are usually insufficient for sigma formation[1]. The deleterious effects of sigma phase, embrittlement and loss of creep-rupture strength, should be avoided[4,6].

2.1.6 Additional Alloy Elements

Less major alloy additions, in terms of weight percentage, to AISI 304 stainless steel include molybdenum, manganese, silicon, titanium, niobium and vanadium. All of these elements are ferrite formers, except for manganese, which stabilises the f.c.c. structure upon cooling but does not increase the gamma boundary at high temperatures[8]. The alloying elements are generally added to improve the materials performance for specific service requirements, such as molybdenum, which improves corrosion resistance and high temperature mechanical properties[8].

2.2 Microstructural Prediction during Hot Rolling

2.2.1 Model Requirements

Hot rolling of stainless steel involves multiple passes to reduce the original slab to final plate thickness. Optimisation of material properties requires a complete understanding of the thermomechanical process and its effect on the microstructure. The process of predicting microstructure behaviour of stainless steel plate in the rolling mill is complicated by the variation in deformation parameters through the thickness and length of the rolled plate[9]. The constantly changing deformation variables, which determine microstructural behaviour, need to be accurately calculated using computational methods such as finite element analysis. Temperature and mechanical models are thus required to determine the deformation values that will provide the input for a microstructural prediction model. Figure 2.3 illustrates the series of models and their inter-dependence required for accurate prediction of final material properties.

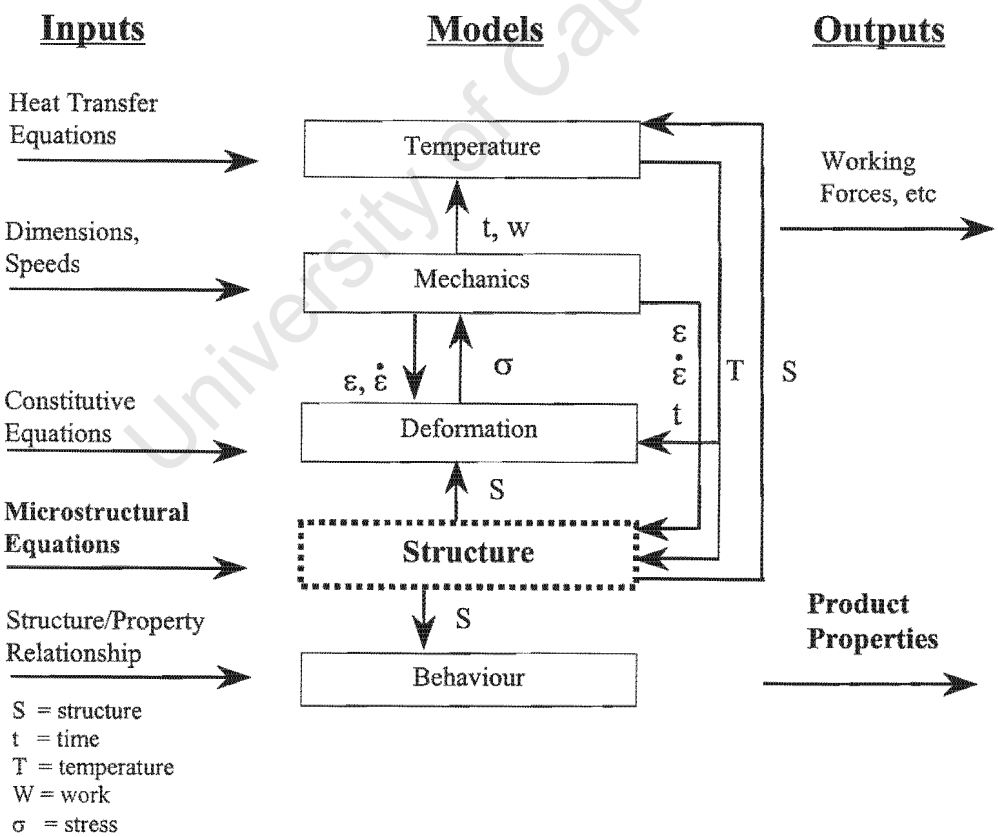

Figure 2.3: **Schematic diagram illustrating the inter-dependence of the various models required in predicting final material properties[10].**

The approach to predicting microstructural development involves a combination of models for online control during industrial processing. However, an all-encompassing model first requires each component to be separately developed.

The following sections present the microstructural changes associated with hot rolling, their effect on the materials properties and equations to predict material response to deformation conditions.

2.2.2 The Deformed State

An understanding of the deformation microstructure is a fundamental aspect in determining softening processes that will occur during rolling and subsequent holding intervals. Accumulation of dislocations within the material during plastic deformation provides the driving force for recovery, recrystallization and grain growth mechanisms. In addition to the dislocation accumulation within the grains, the stored energy of deformation is also increased by the "pancaking" of the grains during rolling, which increases grain boundary energy[11]. However, approximately 95% of the energy expended in deforming the metal is given out as heat.

2.2.3 Dynamic Processes

During deformation under hot working conditions, such as rolling where the strain rate is greater than zero, all metals exhibit characteristics of work hardening as dislocation accumulate within the grains. The stored energy is alleviated by dynamic recovery and in some materials dynamic recrystallization occurs[12]. The dynamic processes are so called to differentiate from the static softening mechanisms that occur during stages when deformation ceases; this would be the inter-pass time when referring to hot rolling.

Recovery and recrystallization are competing processes as increased recovery, which is usually initiated prior to recrystallization, reduces the stored energy available for recrystallization[11]. However, processing parameters coupled with material properties determine which softening process will dominate[13]. The effect of processing parameters consisting of temperature, strain rate and strain along with material properties such as grain size and stacking fault energy (SFE) will be discussed in the proceeding sections in terms of their effect on the softening mechanisms.

2.2.4 Dynamic Recovery

Recovery refers to the change in the deformed materials microstructure prior to recrystallization[11,14,15,16]. There is a structural change associated with recovery comprising the annihilation and rearrangement of dislocations into lower energy configurations, formation of subgrains and their subsequent growth. The subgrains formed during recovery lead to a curvature in the lattice typically between 1^0 and 10^0. The migration of high angle grain boundaries, arbitrarily defined as a boundary with a misorientation greater than 15^0, is not involved and there is no essential change in the crystallographic orientation of the material[14,15]. Formation of the low angle boundaries is due the glide and cross-slip of the dislocations. SFE has a significant influence on recovery mechanisms and since a low SFE hinders dislocation cross-slip, the role of recovery is limited in such materials[17,18].

2.2.5 Stacking Fault Energy

The dissociation of a perfect dislocation into two partial dislocations is known as a stacking fault[19]. The dissociation causes a local change in the stacking sequence such that the normal arrangement in the f.c.c. array, ABCABCABC, changes to ABCACABCA. The occurrence is energetically favourable, as the total energy of the two partial dislocations is less than the energy associated with a perfect dislocation[1].

The extent of separation of the partial dislocations is related to the SFE. The width of the fault is inversely proportional to the metals SFE. Therefore, low SFE metals produce wide stacking faults during deformation, with the result that cross-slip is hindered and slip distances are short[20]. Dislocation annihilation and rearrangement is consequently easier in high SFE metals than those with a low SFE. In terms of recovery and recrystallization, the SFE of the metal is an important parameter, as the behaviour of the dislocations will determine which mechanism will predominate.

Austenitic stainless steel type 304 has a low SFE, with a typical value being in the region of $13mJm^{-2}$, the precise value being dependent on the alloying elements[21,22]. Thus in the study of softening processes associated with AISI 304 stainless steel the role of recovery is limited, subgrain formation is usually not well defined and recrystallization is consequently the dominant process of replacing deformed grains[23,24]. However, there has been evidence of stainless steel type 304 exhibiting

characteristics of dynamic recovery under suitable conditions[23,25]. Furthermore, poorly developed subgrains have been found to produce areas where dynamic recrystallization is initiated[16,23,26]. Although recovery acts to suppress recrystallization, due to reduction in stored energy, the situation where recovery is insufficient leads to a non-uniform substructure. The sub-boundary dislocation density increases and is unable to retain its low misorientation as straining continues; the local difference in dislocation density and increasing misorientation satisfies conditions for nucleation of recrystallization[23,26,27]. In contrast to AISI 304 stainless steel with a low SFE, work done by McQueen[26] on pure aluminium with a high SFE, dynamic recovery occurred readily and prevented nucleation of recrystallization. Thus, the recovery process completely balanced the effect of dislocation accumulation and work hardening, leading to a steady state flow.

2.2.6 Effect of Recovery on the Flow Curve

The characteristics of the stress-strain curve are determined by the deformation conditions and the associated softening mechanisms. During initial stages of deformation, work hardening occurs as the dislocation density increases, and there is a consequential rise in the flow stress. The onset of recovery, assuming favourable conditions for initiation, reduces the flow stress until a steady state flow stress (σ_s) is established[16]. Ryan et al[28] studied the effects of recovery on the stress-strain curve for AISI 317 stainless steel. The characteristics of type 317 are similar to type 304; both have a low SFE but 317 is slower to dynamically recover and recrystallize. Figure 2.4 illustrates the shape of the stress-strain graphs due entirely to recovery by extrapolating the curves before the effects of recrystallization have commenced. The extrapolation determines a hypothetical saturation stress, σ_s^*, which would result from dynamic recovery alone.

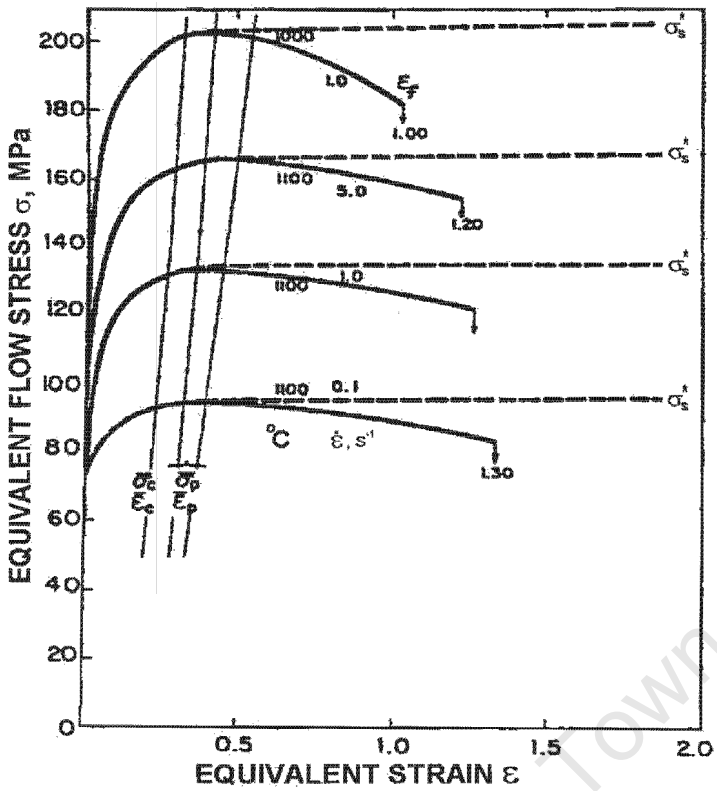

Figure 2.4: **Effect of dynamic recovery on the equivalent stress-equivalent strain curves for type 317 deformed at different temperatures and strain rates. The theoretical curves (- - -) and σ_s^* resulting from dynamic recovery alone are also shown[28]. ε_c represents the critical strain for dynamic recrystallization and ε_p is the strain corresponding to the peak on the stress-strain curve.**

Dynamic recovery is a thermally activated process and thus more effective at high temperatures as dislocations are more mobile. The dislocation generation rate is also reduced as the effective stress in the material is lowered with higher temperatures and/or lower strain rates[26,28]. Figure 2.4 illustrates the decrease in strain hardening and peak stress, σ_p, due to dynamic recovery occurring more effectively at higher temperatures or lower strain rates i.e. lower σ_s^*.

2.2.7 Relationship between Recovery and ε_c

The critical strain for dynamic recrystallization, ε_c, is also shown in figure 2.4 and it is clear that it increases as σ_s^* increases. The increase in ε_c as temperature decreases is attributable to the decreased rate of recovery, and thus recrystallization nucleation sites, at lower temperatures[16]. There appears to be a contradiction between rate of recovery and nucleation of recrystallization as temperature increases; intuitively it

would be expected that increased recovery reduces the stored energy and thus prevents nucleation of dynamic recrystallization. However, it should be borne in mind that the subgrains provide the nucleus for recrystallization. Thus, at high temperatures the subgrains will develop more rapidly and act as nucleation sites for recrystallization. In other words, the rate of recovery is indeed increased, but since the subgrains provide the nucleation sites for recrystallization, the critical strain for initiation of the dynamically recrystallized grains is also reduced.

An increase in strain rate is shown in figure 2.4 to increase the value of ε_c. A rise in the strain rate actually decreases the time required for recrystallization to begin, but the reduction is insufficient to offset the effect of strain rate on the flow curve. Thus, the value of ε_c is increased. It should be taken into account that recovery is limited in the material under discussion. The curves in figure 2.4 are thus useful in demonstrating the effect of recovery on the shape of the flow curve and the relationship between recovery and the initiation of dynamic recrystallization.

2.2.8 Temperature-Compensated Strain Rate

It has been shown in the preceding section that strain rate and deformation temperature, in addition to the strain, affect the restoration process during thermal deformation applications. The effect of strain rate and temperature can effectively be combined and described in terms of the Zener-Hollomon Parameter, Z, given by:

$$\mathbf{Z = \dot{\varepsilon} \exp\left(\frac{Q}{RT_{def}}\right)} \qquad \textbf{Equation 2.1}$$

Where: $\dot{\varepsilon}$ = strain rate

Q = activation energy for deformation

R = gas constant

T = temperature of deformation

The size of the subgrains formed during dynamic recovery can be related to Z. It has been observed[16,26,28] that there is an increase in subgrain size with a decrease in Z i.e.

low strain rate and high temperature. During steady state deformation the equilibrium subgrain diameter can be described by the following relation:

$$d_s^{-1} = a + b.\log Z \qquad \textbf{Equation 2.2}$$

Where **a** and **b** are empirical constants. Thus, the size of the subgrains increase as dynamic recovery becomes more effective at lower Z values. Figure 2.5 illustrates the effect of Z on the subgrain diameter for type 317 and 304 stainless steel.

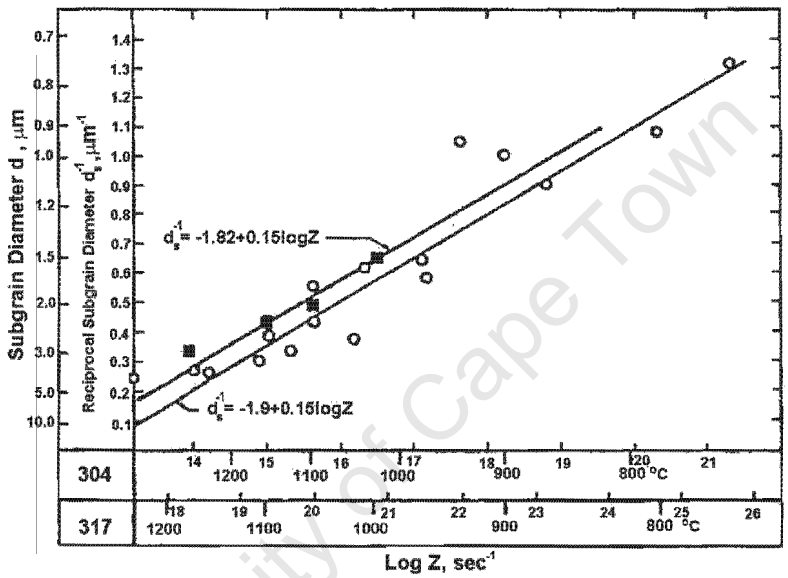

Figure 2.5: **Effect of Z on the dynamically recovered subgrain size for type 317(■) and type 304(○) austenitic stainless steels[28].**

2.3 Dynamic Recrystallization

2.3.1 Introduction

Recrystallization involves the annihilation of dislocations in large quantities and differs to recovery in that the latter process involves the annihilation of single dislocations in individual events. The formation of a new grain structure within a deformed metal by the migration of high angle grain boundaries, generally a 15° or higher misorientation, is defined as recrystallization[14,15,16]. The driving force for migration of the new high angle grain boundary is provided by the stored energy of deformation. Dynamic recrystallization refers to the occurrence of recrystallization during deformation i.e. strain rate greater than zero. The steady state stress, which results from dynamic recrystallization, is significantly less than that which would result if dynamic recovery were the only softening mechanism[16].

2.3.2 Effect of Dynamic Recrystallization on the Flow Curve

The stress-strain curve of a metal deformed at high temperatures is affected by the initiation of dynamic recrystallization[29]. The high temperature regime typically refers to temperatures greater than $0.6T_m$, where T_m (Kelvin) is the material's melting point. During continuous plastic deformation, in a metal that exhibits limited recovery, the density of dislocations increases until a peak stress, σ_p, is attained. The onset of dynamic recrystallization causes the stress to drop as dislocation annihilation commences. The peak strain, ε_p, is used to describe the strain value that corresponds to σ_p. It should be noted that dynamic recrystallization is usually initiated at strain value prior to ε_p, which is termed the critical strain for recrystallization, ε_c. However, the effect of recrystallization on the shape of the flow curve only appears after the ε_p value has been exceeded[12]. The relationship between the critical strain, ε_c, and ε_p for AISI 304 has been found to be given by the relation[29], $\varepsilon_c=0.73\varepsilon_p$.

The flow curves associated with dynamic recrystallization have been shown by Luton and Sellars[30] to exhibit cyclic or single peaks during high temperature deformation. They found the cyclic or single peak behaviour, associated with dynamic recrystallization, to be dependent on the kinetics of deformation, namely strain rate and temperature. The cyclic curve arises when ε_c is greater than the strain required

for the completion of recrystallization, ε_x, i.e. at low strain rates and high temperatures. Thus, once recrystallization has commenced, it is completed before the regions which first recrystallized can work harden and nucleate a second cycle. At high strain rates and low temperatures, ε_x is greater than ε_c and regions which first recrystallized reach the critical strain for a second nucleation before the first cycle of recrystallization is complete. Therefore, the metal is always in a partly recrystallized state, with more than one cycle of recrystallization occurring. This results in an equilibrium distribution of regions having different strains, which creates an average flow stress and a single peak on the flow curve. Figure 2.6 illustrates both the cyclic and single peak behaviour associated with dynamic recrystallization.

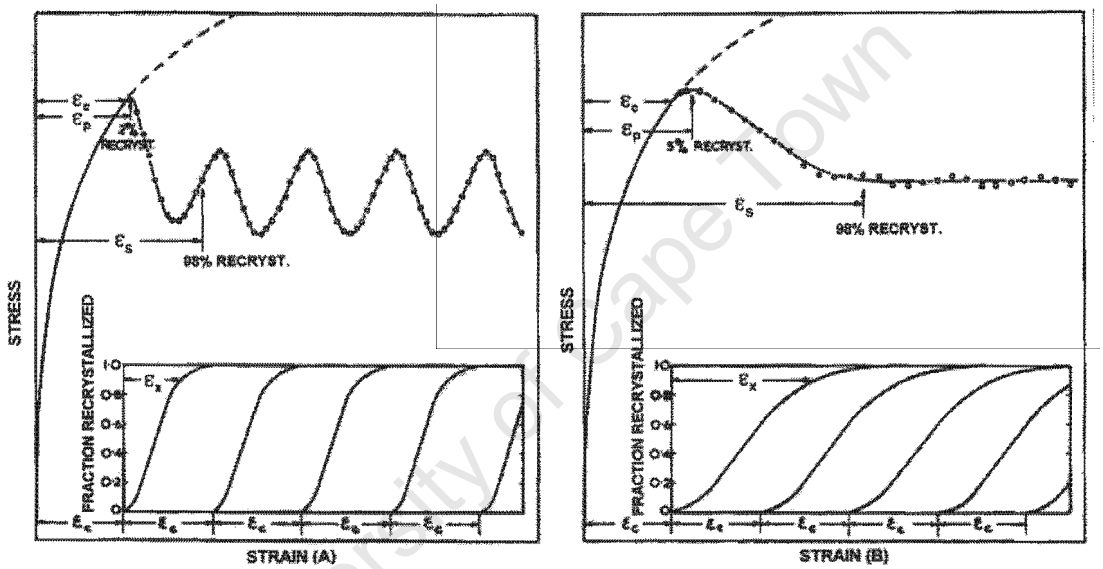

Figure 2.6: **Predicted stress-strain curves for dynamic recrystallization. (A) Cyclic curve when the critical strain to initiate recrystallization ε_c is greater than the strain required for completion of recrystallization, ε_x. (B) Single peak curve when $\varepsilon_x > \varepsilon_c$. ε_s is defined as the strain required to complete the first cycle of recrystallization. The difference between ε_s and ε_c is used to calculate ε_x[30].**

Sakai and Jonas[31,32] found the kinetic model proposed by Luton and Sellars to be insufficient during high temperature deformation of f.c.c. metals in tension and compression. They showed the shape of the flow curve to be dependent on the ratio of the initial grain size, D_o, to stable recrystallized grain size, D_s. The transition from cyclic to single corresponds to a 2:1, or greater, reduction in grain diameter. Thus, when $D_o/D_s > 2$ nucleation was found to occur at existing grain boundaries and the "necklace" mechanism of recrystallization operates. Figure 2.7 illustrates the

necklacing phenomenon that evolves during dynamic recrystallization. Deformation occurring within the first layer of dynamically recrystallized grains reduces the boundary migration driving force before complete recrystallization can occur. A second layer of recrystallized grains nucleates ahead of the first layer, as the dislocation density is high in that region[12]. Thus, the material is only in a partly recrystallized state and a single peak flow curve results. In the second scenario, when $D_o/D_s < 2$ there are sufficient nucleation sites for all the new grains to develop and complete the recrystallization in one cycle (see figure 2.7e). The material is therefore completely recrystallized before further deformation and work hardening is repeated, giving rise to the cyclic flow curve.

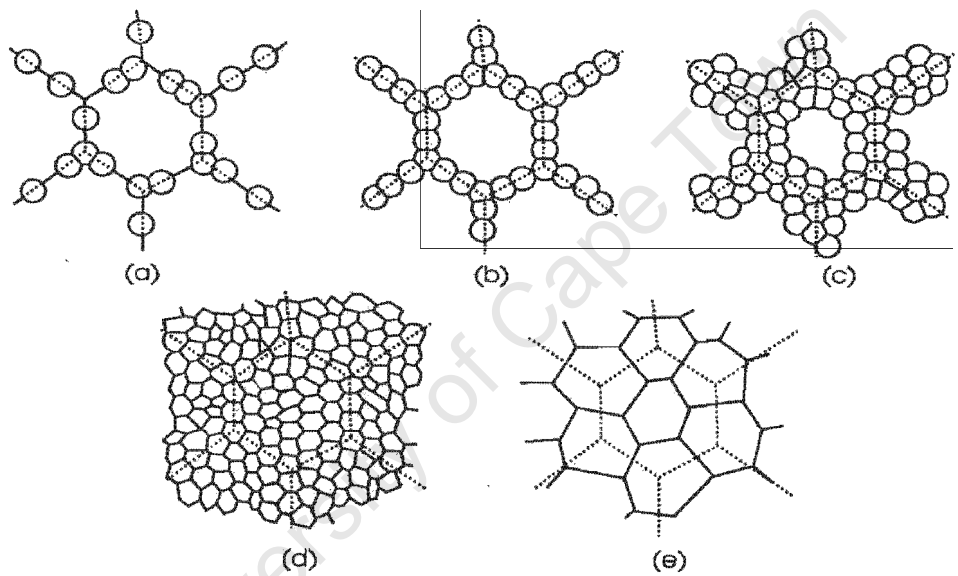

Figure 2.7: **(a-d) The development of the necklace structure during dynamic recrystallization in a material with D_o greater than twice D_s. (e) For small D_o recrystallization is complete in a single nucleation event[11].**

2.3.3 Effect of D_o on Recrystallization Kinetics

In the previous section, the effects of D_o where discussed with reference to the shape of the flow curve. However, the kinetics of dynamic recrystallization are also affected by the size of D_o. It has been shown that as D_o increases the dynamic recrystallization kinetics decrease[12,33]. A reduction in D_o promotes an increase in dislocation accumulation at grain boundaries and thus a steeper rise in the work-hardening rate. The ε_c for dynamic recrystallization, which depends on the dislocation density, is therefore attained at a relatively lower strain. Roberts et al[12] studied the influence of

D_0 on the kinetics of dynamic recrystallization at a particular temperature and strain rate and showed the increase in kinetics for a reduction in D_0. Figure 2.8 illustrates their results for type 304 and 4439 austenitic stainless steels.

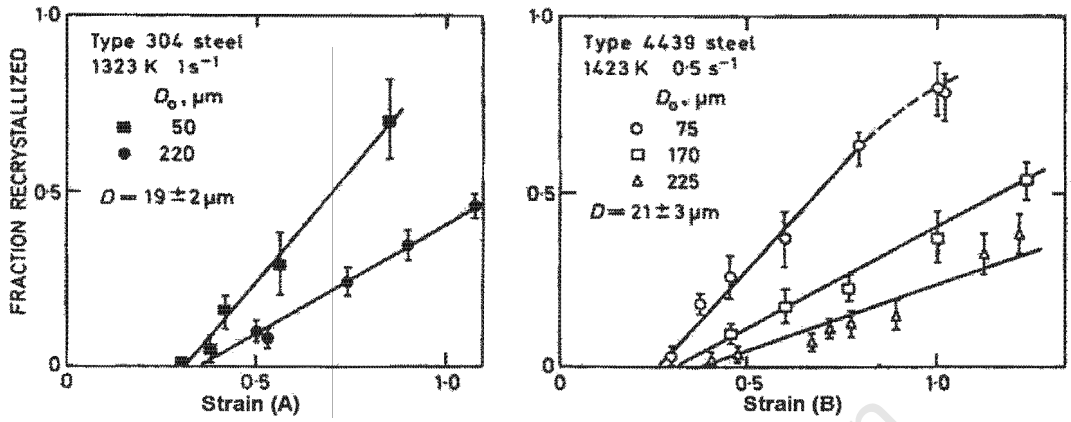

Figure 2.8: **Volume fraction dynamically recrystallized as a function of strain for different values of D_0 (A) Type 304 (B) Type 4439 austenitic stainless steel[12].**

2.3.4 Industrial Considerations

The dynamic softening mechanisms discussed above are an important aspect of industrial hot rolling processes. They lower the flow stress of the material, reducing the roll forces required for the production of metal plate[11]. Dynamic recrystallization also affects the static softening processes following hot rolling. There exists a distribution of strain in the metal due to the characteristics of dynamic recrystallization. The strain distribution, or deformed state, will determine the static recrystallization behaviour of the rolled material. Since deformation is occurring during nucleation and growth of new dynamically recrystallized grains, the recrystallized grains are being deformed as they grow. Thus, the task of visually identifying dynamically recrystallized grains is complicated. However, the effects of dynamic recrystallization need to be borne in mind when studying static recrystallization mechanisms.

2.4 Static Processes

2.4.1 Introduction

Thus far, the softening processes involved during hot rolling have referred to the dynamic events. However, the softening processes are not limited to the dynamic stages and further microstructural changes occur during intervals of hot working. Static softening can occur by either recovery or recrystallization mechanisms depending on material properties, prior deformation conditions, time and the temperature of the material during the static period[34]. The driving force for the static softening processes are provided by the stored energy of deformation and facilitated by relatively easy diffusion at high holding temperatures. During industrial hot rolling schedules, the extent of static softening is important as it determines the material flow stress and thus the roll forces for subsequent passes.

2.4.2 Metadynamic Recrystallization

Unique to hot worked metals is the softening process of post-dynamic or metadynamic recrystallization. When deformation is stopped during dynamic recrystallization the grain boundaries continue to migrate and nuclei are already present within the deformed material[16]. A prerequisite for metadynamic recrystallization is that dynamic recrystallization was occurring in the previous pass, hence its distinctiveness to hot worked metals. Thus, during the annealing interval there are certain areas of the material that do not require a nucleation period and recrystallization occurs rapidly. In regions where there are no dynamic nuclei, the nucleation of static recrystallization can still take place. The difference in the rates of metadynamic and static recrystallization, which can be up to two orders of magnitude, need to be taken into account when studying pure static recrystallization kinetics[35].

2.4.3 Critical Strain for Static Recrystallization

The predominant softening mechanism for type 304 austenitic stainless steel during the hot rolling interval is static recrystallization[36,37]. The amount of static recovery is limited, as is the case with the dynamic events, due to the low SFE of the steel[34]. It has been suggested that there is a critical strain of approximately 10% required for static recrystallization to be initiated; if the critical strain is not attained then softening by static recovery can only take place[16,35]. During industrial hot rolling of austenitic

stainless steel, the average reduction per pass exceeds the critical strain, so it is expected that static recrystallization will occur during the interval[38]. However, the time required for static recrystallization to commence is also sensitive to other parameters such as strain rate and holding temperature. A further variable is the reversing sequence of the steel plate during hot rolling which affects the time available for recrystallization. The front end of the plate will exit the roll bite first and thus have more time for recrystallization to occur than the end section. Immediately the end section of plate exits the roll bite it returns for the second pass, allowing a limited time for nucleation of static recrystallization. Thus, in the intervals of hot rolling, it is possible that the percentage of material statically recrystallized will vary along the plate length. Figure 2.9 illustrates the effect of prior strain on the softening curves for a 0.68% C steel. The graphs in figure 2.9 illustrate that a prior strain of 0.055 (curve A) was followed by a recovery period that lasted approximately100 seconds and softening did not go to completion. Thus, it illustrates that the critical strain for static recrystallization was in excess of 0.055. In curve B, for a prior strain of 0.098, recovery was complete after 100 seconds, followed by an incubation period and then the commencement of static recrystallization. The incubation period is due to the formation of nuclei and the time required depends on the kinetics of the recovery and recrystallization mechanisms[39]. It is important to recognise that even if the critical strain for static recrystallization is exceeded, it is possible that it will not have commenced/or completed in the time interval between the rolling passes.

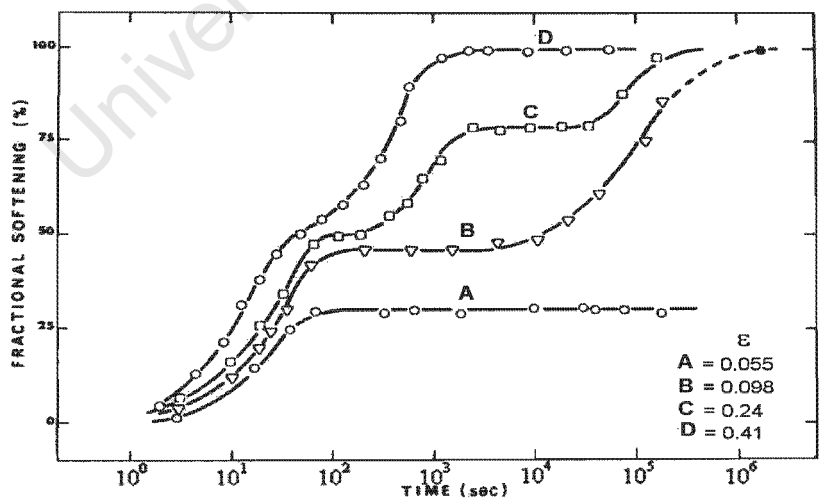

Figure 2.9: **Effect of strain on static softening behaviour of a 0.68% C steel at 780°C. The first plateau in the curves represents the completion of static recovery and nucleation period of static recrystallization. The second plateau in curve c represents the finish of metadynamic recrystallization (section 2.4.2)[39].**

2.4.4 Nucleation of Recrystallization

The nucleation and growth mechanisms that occur during recrystallization have been the subject of extensive research and discussion[11,40,41,42]. It is not within the scope of this study to review the various mechanisms, but to rather introduce the concept of the recrystallization nuclei and its growth. It has been established that the recrystallized grains do not nucleate as new grains by the atom-by-atom construction, but rather from small regions, recovered subgrains or cells that are already present in the deformed microstructure[11,14]. Thus, the orientation of each new grain is the same as the orientation of the deformed microstructure. As discussed by Hatherly[40], new orientations are formed in materials with low SFE by twinning of the growing grain. Subgrains are required to have a high misorientation angle to the adjacent microstructure to enable a sufficient driving force for growth. Thus, nucleation only occurs in regions that have a high local misorientation[11,40]. In the review by Doherty et al[14] regions with high local misorientations include:

- Pre-existing high angle grain boundaries;
- a misoriented transition band within a grain (the activation of different slip systems within a grain can cause different lattice rotations, producing high misorientations);
- deformation zones around large particles;
- regions within shear bands (formed during rolling; extensive shear occurs locally as a planar region orientated at approximately 30° the rolling plane[43]).

The growth of the migrating boundary is provided by the stored energy in the deformed microstructure. The velocity of the migrating boundary can be described by the following equation:

$$v = \mathbf{M}.\Delta f \qquad \textbf{Equation 2.3}$$

where M is the mobility term and Δf is the driving force. From equation 2.3, an increase in the stored energy, provided by increased deformation, enables greater mobility of the migrating boundary and thus less time required for the material to fully recrystallize.

2.4.5 Static Recrystallization Kinetics

The kinetics of softening in austenitic stainless steels are dominated, in most instances, by the kinetics of static recrystallization due to the limited recovery. Recrystallization kinetics have been extensively studied using the approach developed independently and simultaneously by Johnson and Mehl, Avrami and Kolmogorov, which is referred to as the JMAK theory[11]. The theory assumes that nucleation sites are randomly distributed, growth is isotropic and growth rate is constant. The JMAK theory will then predict the volume fraction of material recrystallized, X_v, in a given annealing time, t, according to the equation:

$$X_v = 1 - \exp\left[-B\left(\frac{t}{t_f}\right)\right]^n \qquad \textbf{Equation 2.4}$$

Where X_v = volume fraction of material recrystallized

t_f = time for a specified fraction of recrystallization, f

B = -ln(1-f)

n = Avrami constant (material property)

In equation 2.4, the value of **f** is often used by researchers[36,37,38,44] to equal 0.5, where $t_{0.5}$ is referred to as the time for 50% recrystallization. Thus, equation 2.4 is given by the following expression:

$$X_v = 1 - \exp\left[-0.693\left(\frac{t}{t_{0.5}}\right)\right]^n \qquad \textbf{Equation 2.5}$$

The JMAK equation, although extensively used among researchers, has certain shortcomings that need to be considered when studying recrystallization kinetics. The failure of the JMAK equation to accurately describe certain recrystallization kinetic behaviour is due to the deviations between theory and experimental data. An essential feature of the JMAK equation is that nucleation sites are randomly distributed within the microstructure. However, deviations arise due to the inhomogeneous deformation microstructure that occurs experimentally, producing non-random distribution of nuclei[11,36,45]. The preferred nucleation sites such as prior grain boundaries, transition bands and shear bands contribute to the non-random distribution[46]. The inhomogeneous microstructure also gives rise to variations in the nuclei growth rate,

assumed constant in the JMAK theory. Areas of higher stored energy, due to inhomogeneous microstructure, nucleate first and growth rate is rapid. However, once the areas of stored energy are depleted, growth rate decreases as nuclei grow into regions of lower stored energy. Figure 2.10 provides a schematic representation of the variation in growth rate due to areas of higher stored energy. Recovery can also effect the growth rate as the driving force for recrystallization is reduced, causing deviation in the JMAK theory[45].

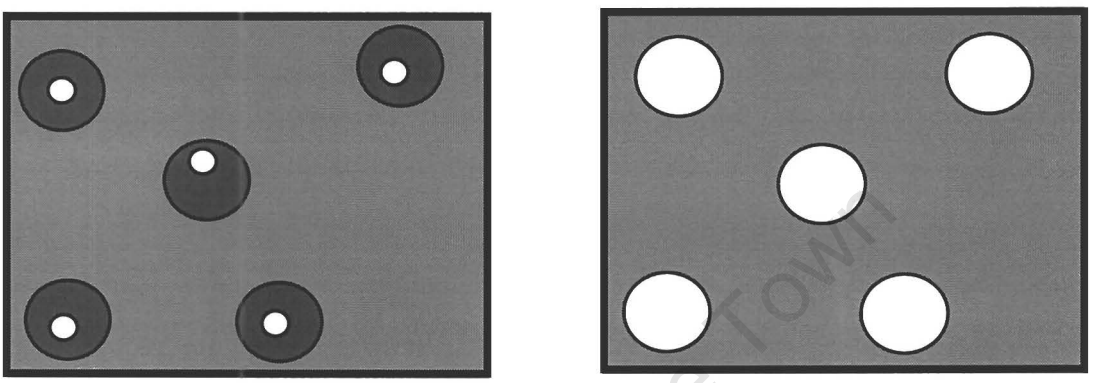

Figure 2.10: **(a) Areas of high stored energy (dark grey areas) are the first to nucleate (white areas) and growth is rapid. (b) High stored energy areas are soon depleted and growth is sluggish as grains grow into areas of lower stored energy (light grey areas)[11].**

The shortcomings noted above emphasise that the JMAK equation is accurate only under limiting conditions. The limitations, however, do not void the use of the JMAK equation but its application should be used with discretion. Modelling the kinetics of recrystallization are complicated by the inhomogeneous nature of most annealing phenomena and thus an all encompassing analytical equation is difficult to derive. Although the JMAK equation is not faultless, it does provide a foundation for the understanding of the materials kinetics. The advantage of using the JMAK equation when studying recrystallization kinetics is that extensive work by previous researchers enables comparisons to be made between the experimentally determined Avrami constant, n. The deviation of n from the predicted value can provide information regarding the material's response during static recrystallization. Attempts to develop improved Avrami models are established on the original theory and thus a base understanding of the material's behaviour, in terms of JMAK, is essential.

2.4.6 Effect of Deformation Conditions on Kinetics

The $t_{0.5}$ variable in the JMAK equation 2.5 incorporates the effect of deformation conditions on the recrystallization kinetics. It is thus a measure of the rate of recrystallization and depends on the deformation conditions, temperature during the inter-pass interval and the material properties. Sellars and Whitman[13] found that the effect of the variables on $t_{0.5}$ could be given by the following:

$$t_{0.5} = A.D_o^{\,a} Z^{-b} \varepsilon^{-c} \exp\left(\frac{Q_{rex}}{RT}\right) \qquad \textbf{Equation 2.6}$$

Where: A = material constant
D_o = initial grain size
a = material constant
Z = Zener-Hollomon parameter
b = material constant
ε = strain during the previous pass
c = material constant
Q_{rex} = activation energy for recrystallization
R = gas constant
T = annealing temperature

Equation 2.6 has been used extensively by researchers to describe the relationship between recrystallization kinetics and the deformation conditions. Table 2.1 lists the values of the material constants for austenitic stainless steels determined by various researchers.

Researcher	Material	Equation
Towle & Gladman[37]	Type 304 & 316	$X = 1\text{-}\exp(-Bt^n)$ $n = 0.5$ to 1.5 (304) $t_{0.5} = A.Z^{-0.375}\varepsilon^{-2}D_o^{\,2}\exp\left(\frac{Q}{RT}\right)$ $Q_{rex}^{304} = 365\text{kJ/mol}$; $Q_{rex}^{316} = 525\text{kJ/mol}$
Barraclough & Sellars[36]	Type 304	$X = 1\text{-}\exp(-Bt^n)$ $n = 1$ to 2 $t_{0.5} = 3.72.10^{-15}Z^{-0.38}D_o^{\,2}\exp\left(\frac{Q}{RT}\right)\frac{1}{f(\varepsilon)}$ $f(\varepsilon) = 1-\exp\left(-1.5\left(\frac{\varepsilon-0.08}{\varepsilon_p}\right)^2\right)$ $Q_{rex} = 425\text{kJ/mol}$
Barbosa & Sellars[47]	Type 316L	$X = 1\text{-}\exp(-Bt^n)$ $n = 0.5$ to 1 $t_{0.5} = 4.10^{-15}.Z^{-0.38}\varepsilon^{-3.6}D_o^{\,1.33}\exp\left(\frac{Q}{RT}\right)(\varepsilon \le \varepsilon_c)$ $t_{0.5} = 1{,}8.10^{-7}.Z^{-0.6}\exp\left(\frac{Q}{RT}\right)(\varepsilon \ge \varepsilon_c)$ where $\varepsilon_c = 7{,}5.10^{-3}Z^{0.06}D_o^{\,0.37}$ $Q_{rex}^{316} = 475\text{kJ/mol}$
Vieira, Santos & Barbosa[38]	Type 304	$X = 1\text{-}\exp(-Bt^n)$ $n = 0.4$ to 1.6 $t_{0.5} = A.Z^{-0.32}\varepsilon^{-4}D_o^{\,2}\exp\left(\frac{Q}{RT}\right)$ $Q_{rex} = 400\text{kJ/mol}$
Ryan, McQueen & Evangelista[48,49]	Type 301, 304, 316, 317	$X = 1\text{-}\exp(-Bt^n)$ $n = 1.1$ to 1.66 $t_{0.5} = A.Z^{-0.375}\varepsilon^{-2}D_o^{\,2}\exp\left(\frac{Q}{RT}\right)$
Karjalainen et al[50]	Type 304	$t_{0.5} = 6.10^{-14}.Z^{-0.3}\varepsilon^{-2.2}D_o\ \exp\left(\frac{Q}{RT}\right)$ $Q_{rex} = 400\text{kJ/mol}$

Table 2.1: Material constants, determined by various researchers, for $t_{0.5}$ equation.

2.4.7 Temperature of Deformation and Strain Rate

Static recrystallization is driven by the stored energy provided by deformation, with the recrystallization rate increasing with an increase in the stored energy. During hot rolling the total stored energy would be determined by the amount of strain per pass, the strain rate and the temperature of deformation. Equation 2.6 is effective in quantitatively determining the effect of deformation parameters on recrystallization rate. The effect of strain rate and temperature of deformation are included in equation 2.6 using the Z parameter. An increase in strain rate will raise the Z value, which reduces the $t_{0.5}$ value (exponent of Z parameter is negative). The Z value is lowered by an increase in the deformation temperature reducing the driving force for static recrystallization. Barraclough and Sellars[36] studied the effect of Z on the static recrystallization kinetics for type 304 stainless steel. Their results, presented in figure 2.11, illustrate the dependence of time for 50% recrystallization on the Z parameter.

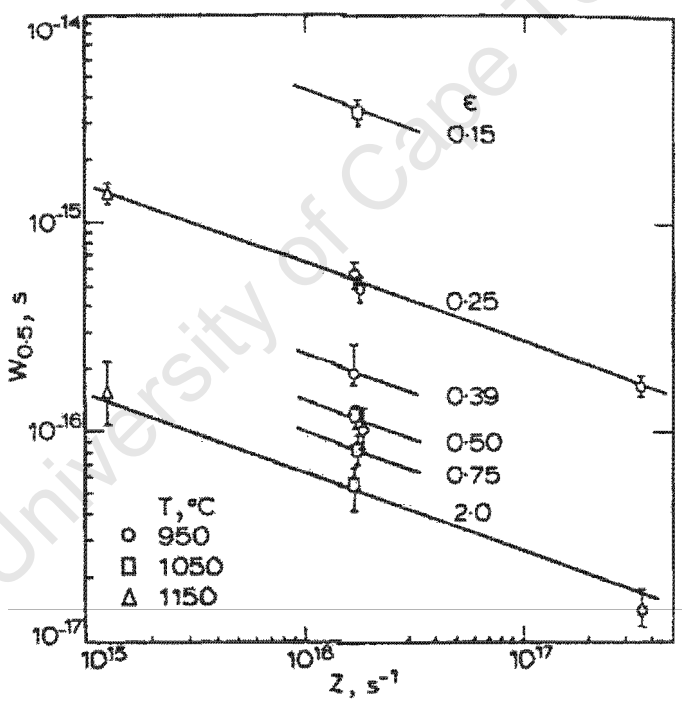

Figure 2.11: The effect of Z on the temperature-compensated time to 50% recrystallization*, $W_{0.5}$, for 304 stainless steel[36].

* The temperature-compensated time parameter, W, takes into account the effect of changing temperature during non-isothermal annealing conditions, for example, following an industrial rolling schedule the stock temperature will decrease with holding time and thus affect $t_{0.5}$.

2.4.8 Strain

Recrystallization time is reduced by increasing the strain during deformation. However, it has been observed that the effect of strain on $t_{0.5}$ decreases as the flow curve approaches ε_p and has zero effect by the onset of steady state deformation[36,37]. Towle and Gladman[37] have explained the decreasing effect of strain on $t_{0.5}$ in terms of the position that interruption occurs on the flow curve. The commencement of steady state deformation implies that the strain energy will effectively remain constant and thus as strain increases the stored energy, which is the driving force for recrystallization, will remain constant. Figure 2.12 illustrates the effect of strain on $t_{0.5}$. The rate of recrystallization increases rapidly with an increase in reduction of area from 15-30% (true strain = 0.2-0.45), but little effect as reduction increased from 30%-50%. They thus concluded that the strain exponent in the $t_{0.5}$ equation depends on the strain range that is examined.

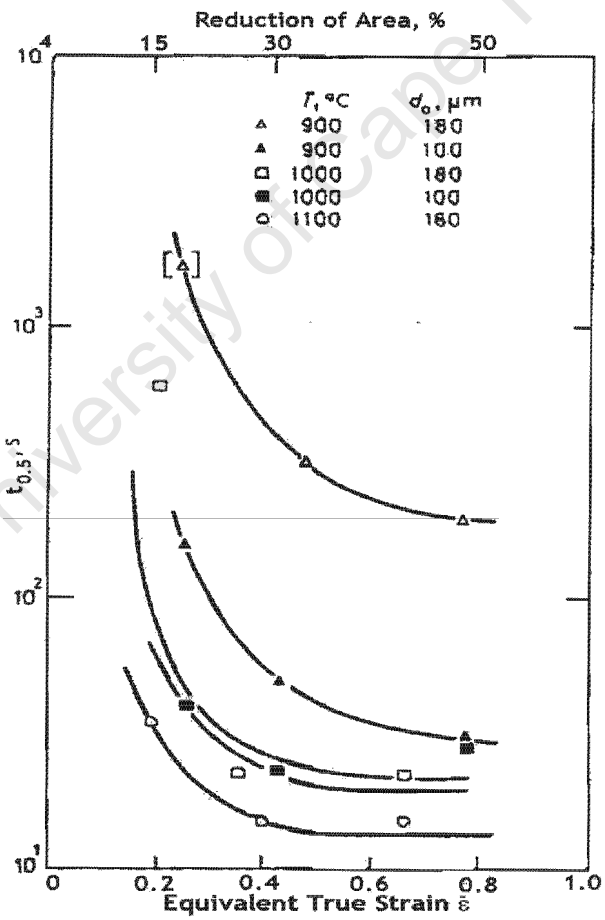

Figure 2.12: The effect of strain on the $t_{0.5}$ for 304 stainless steel[37].

Barraclough and Sellars[36] found a similar effect of increasing strain on $t_{0.5}$. The increased effect of dynamic softening processes and metadynamic recrystallization as strain approaches the peak rapidly decrease the effect of strain on $t_{0.5}$. Owing to the discrepancy, they developed an alternate method to describe the effect of strain on $t_{0.5}$ given by:

$$t_x \alpha \left[1 - \exp -1.5\left(\frac{\varepsilon - 0.08}{\varepsilon_p}\right)^2\right]^{-1} \qquad \textbf{Equation 2.7}$$

They do not claim that equation 2.7 has a physical significance, but it does recognise that the peak strain, ε_p, is important and that a critical strain for static recrystallization, given as 0.08, does exist.

2.4.9 Annealing Temperature

The annealing temperature has a significant effect on the recrystallization kinetics. Figure 2.13 shows that for an increase in temperature of 100^0C there is an approximate order of magnitude decrease in the time for complete recrystallization. An increase in the annealing temperature provides the activation energy for nuclei to grow into the deformed microstructure at a faster rate, thus reducing the time for complete recrystallization.

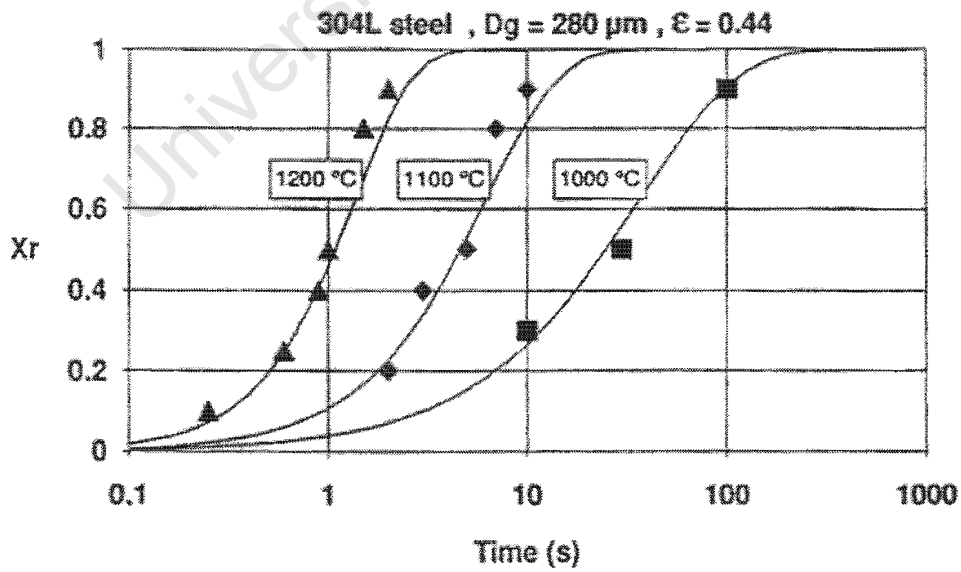

Figure 2.13: The effect of annealing temperature on the static recrystallization kinetics of 304L stainless steel[51].

Chapter 3

Experimental Methods

3.1 Approach to Microstructural Prediction

3.1.1 Introduction

The Avrami and $t_{0.5}$ equation (equation 2.5 and 2.6 in Chapter 2 respectively) have been used in this study to determine microstructural behaviour of AISI 304 stainless steel during hot rolling intervals i.e. static processes. It is realised that there are limitations to the equations as outlined in section 2.4.5 of Chapter 2. However, the "Avrami" approach contributes to an improved understanding of the material's annealing behaviour and provides valuable insight for future microstructural evolution applications. It was thus decided that the Avrami equations were appropriate as a preliminary foundation for gaining an understanding on predicting microstructural evolution. The equations enable an empirical relationship to be developed based on experimental data obtained on a laboratory scale. An understanding of the procedure to determine the material constants was required prior to formulating an experimental matrix. The following section introduces the method used to derive the various material constants for each equation.

3.1.2 The Avrami Equation

The Avrami constant can be determined from the experimental data relating volume fraction of material recrystallized versus annealing time during isothermal annealing. The method used to determine the recrystallized volume fraction is an important aspect of the modelling process. Microhardness measurements provide a good indication of annealing behaviour and the results are often used to calculate the extent of recrystallization. This method is based on the rationale that metals become softer during recrystallization. However, microhardness measurements are unable to account for other softening mechanisms such as recovery or metadynamic recrystallization that may occur during the annealing period. An assumption of the Avrami equation is that softening is due entirely to recrystallization. Thus,

microhardness measurements only provide an indication of the total softening as opposed to actual static recrystallization.

In certain instances a material's softening kinetics are equal to the recrystallization kinetics. This situation might arise in a material that exhibits limited recovery and no prior dynamic recrystallization. Stainless steel type 304, with a low SFE, exhibits limited recovery during annealing and thus for certain conditions the softening kinetics will equal the recrystallization kinetics. However, this relationship needs to be established prior to assuming equal softening and recrystallization kinetics. Traditionally light microscopy was used to calculate the percentage of recrystallization that had occurred during the annealing treatment. In such instances, the fraction recrystallized was based on visual identification and subject to user interpretation. More recently, Electron Backscattered Diffraction (EBSD) provides a more accurate method for determining fraction recrystallized (see section 3.8). Therefore, based on microhardness and EBSD data, a quantitative relationship between softening and recrystallization can be established to determine the correlation.

Once a reliable method has been established to calculate fraction recrystallized the sigmoidal graph of recrystallized fraction versus annealing time can be plotted. From this information the Avrami constant, n, can be determined by rearranging equation 2.5 into a straight line format (y = mx + c) given by the following:

$$\log\left(\ln\left[\frac{1}{1-x_v}\right]\right) = \log 0.693 - n\log(t_{0.5}) + n\log(t) \qquad \textbf{Equation 3.1}$$

where:

$$Y = \log\left(\ln\left[\frac{1}{1-X_v}\right]\right)$$

$$mX = n\log(t)$$

$$c = \log 0.693 - n\log(t_{0.5})$$

The volume fraction of material recrystallized versus annealing time is plotted according to equation 3.1. The Avrami exponent can be calculated from the gradient of the straight line.

3.1.3 Equation for $t_{0.5}$

A similar approach as to the one outlined above is used to determine the material constants for the $t_{0.5}$ equation. The material constants, ***–a***, ***b***, ***-c***, which are the exponents of ε, D_o and Z in equation 2.6 respectively, each need to be determined on an individual basis. The experimental matrix required to determine all the material constants for $t_{0.5}$ is extensive. Therefore, in this study, the experimental matrix was formulated specifically to determine the strain exponent. Of importance, however, was the procedure and annealing characteristics of the material in determining the validity of the exponent for given deformation conditions.

To determine the exponent of strain, ***-a***, the graph of log $t_{0.5}$ needs to be plotted with respect to log ε. The graph has a straight-line format given by the following:

$$\log t_{0.5} = -a \log \varepsilon + \log\left[A.Z^{-c}.D_o^b.\exp\left(\frac{Q_{rex}}{RT}\right)\right] \qquad \textbf{Equation 3.2}$$

where:

$$Y = \log t_{0.5}$$

$$mX = -a \log \varepsilon$$

$$c = \log\left[A.Z^{-c}.D_o^b.\exp\left(\frac{Q_{rex}}{RT}\right)\right]$$

The strain exponent, ***-a***, can be determined from the gradient of log $t_{0.5}$ versus log ε, according to the above equation. For a given set of strain values, the number of lines plotted on the graph of log $t_{0.5}$ versus log ε can be increased by using different annealing temperatures and different Z parameters. Figure 3.1 illustrates the change in log $t_{0.5}$, for a single strain value, by varying Z or annealing temperature.

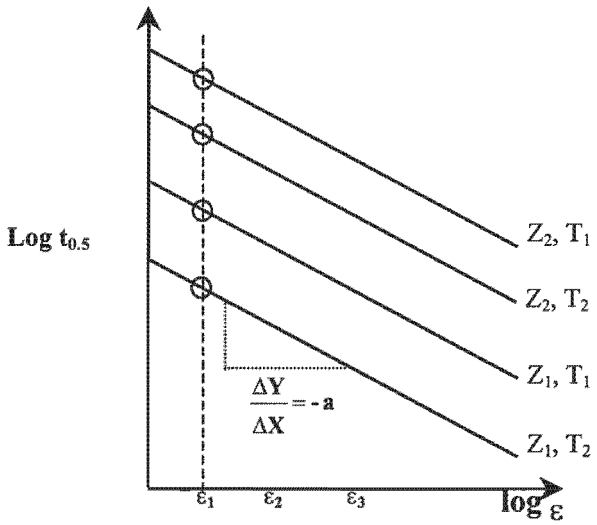

Figure 3.1: **Graph showing the set of lines that can be plotted by varying the Z parameter and the annealing temperature.**

The advantage of plotting a set of lines on the graph is that for each line the gradient can be calculated to determine the strain exponent. This allows for a good statistical average in determining the exponent value. Furthermore, a deviation from the average value, for a specific condition, will provide evidence of annealing behaviour that does not comply with expected Avrami predictions. In such instances, this will provide valuable information relating to the material's annealing phenomena and/or the investigation technique.

3.2 Material Selection

The material under investigation was an AISI 304 austenitic stainless steel containing approximately 18 wt% Cr and 8 wt% Ni. Selection of AISI 304 stainless steel, as the case study material, was motivated by specific material properties that are beneficial in the study of static recrystallization kinetics. These material properties include:

- Addition of Ni promotes the formation of austenite by increasing the gamma loop and prevents transformation to ferrite during cooling from the hot rolling temperature. The single-phase structure limits the variables that effect static recrystallization*.
- Quenching 304 does not produce martensite due to Ni additions decreasing the martensite start temperature to below room temperature. Thus, it is possible to "freeze" the deformed microstructure immediately following high temperature deformation by quenching in water.
- The low stacking fault energy of 304 limits recovery and consequently recrystallization is the dominant softening mechanism.

Table 3.1 provides the chemical composition of the AISI 304 stainless steel that was supplied by Columbus Stainless.

Ni	Cr	Mn	Mo	Si	P	C	Va	Cu	Fe
8.13	18.18	1.38	0.15	0.44	0.02	0.04	0.11	0.09	Balance

Table 3.1 The chemical composition of AISI 304 stainless steel (values given in weight %)

* It should be noted that the presence of ferrite stringers is commonly observed in AISI 304 stainless steel. However, the small fraction of ferrite should not have a significant effect on the recrystallization behaviour.

3.3 Material Processing History

The material was supplied by Columbus Stainless, South Africa, in the form of a strip of metal sectioned from the plate following rolling in the rougher mill and represents what is known as the transfer gauge. Prior to rolling in the roughing mill, the 200mm thick slab was heated to 1200^0C over a four-hour period to homogenise the microstructure. The steel is malleable at 1200^0C and hence the slab can be easily formed into the required thickness during rolling in the rougher mill. The rougher mill is a standard reversing mill where the slab is rolled in a series of reversing passes. The slab is reduced to a thickness of 25 mm, from the original entry gauge of 200mm, in seven passes. The temperature of the plate was approximately 1070^0C on exit from the final reduction pass in the roughing mill. A strip of stainless steel was taken at this stage for experimental purposes. The Steckel Mill is the second stage in the rolling schedule and the plate is further reduced in thickness from 25mm to 6mm. Rolling in the Steckel Mill is a unique process where the plate is rolled back and forth, similar to the rougher mill, but on exit from each pass the plate is rolled up onto coiler drums. The coiling of the plate on either side of the rolling stand provides good temperature retention and eliminates the rapid loss in temperature experienced in standard reversing mills.

This study is concerned with the microstructural processes occurring during hot rolling in the Steckel Mill. The deformation conditions used in the experimental compression tests were thus based on the Steckel Mill rolling schedule. Appendix A provides a typical deformation schedule for rolling of AISI 304 stainless steel.

3.4 Compression Testing

3.4.1 Introduction

Simulation of the industrial rolling process on a laboratory scale is typically performed using plane strain compression (PSC), torsion or uni-axial compression testing techniques. The specifications of the PSC testing machine located at the University of Cape Town did not meet the requirements needed to simulate hot rolling of stainless steel. Thus, uni-axial compression tests were performed using a Gleeble 1500 thermomechanical simulator at the Industrial Metals and Minerals Research Institute (IMMRI), University of Pretoria.

Specimens were machined to specified dimensions, required for Gleeble compatibility, from AISI 304 rolled plate of 25mm thickness (transfer gauge). The axisymmetric specimens (10mm length and 8mm diameter) were sectioned from the same plane to ensure that the microstructure was homogeneous through the dimensions. Figure 3.2 illustrates the orientation and dimensions of the specimens that were removed from the plate.

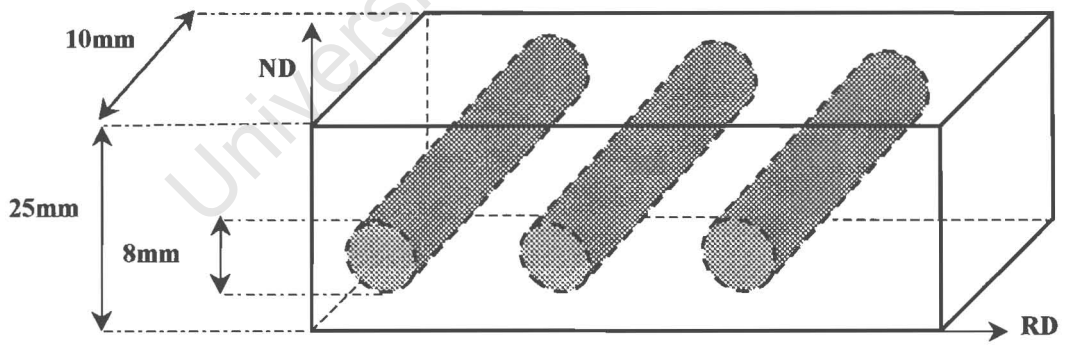

Figure 3.2: Specimen orientation and dimensions sectioned from rolled plate of 25mm thickness.

A suitable annealing treatment was performed, following machining, to homogenise the microstructure and remove any residual deformation. Temperatures in the range of 1050-1150^{0}C are generally used as $M_{23}C_6$ precipitates are in solution and grain

growth is optitmised[4]. A series of annealing treatments were initially performed to determine an adequate time that produced a deformation free microstructure. A time of twenty minutes at 1050^0C was found to produce a suitable microstructure (see Chapter 4, section 4.1.2 for microstructural details). The specimens were water quenched following the annealing treatment.

3.4.2 Gleeble Compression Testing

The Gleeble 1500 is able to simulate various industrial applications, including hot strip rolling and plate rolling, on a laboratory scale. The Gleeble is thus effective in the study of the influence of processing parameters on the microstructure of a material. Specific specimen dimensions (see section 3.4.1) were required for the Gleeble compression tests. High temperature compression testing was performed between two tungsten carbide anvils. The specimen is resistance heated, in a vacuum chamber, by means of a twelve-volt a.c. supply. The vacuum limits the formation of an oxide layer on the surface of the specimen. Prior to testing a tantalum foil strip, which acts as a lubricant, is placed between the specimen and the anvil. The tantalum strip also prevents the diffusion of carbon at the interface.

An 80kN electro-hydraulic actuator deforms the specimen to the user-specified strain and strain rate. Figure 3.3 illustrates the set-up of the Gleeble for compression testing while photographs of the Gleeble equipment are shown in figures 3.4a and b.

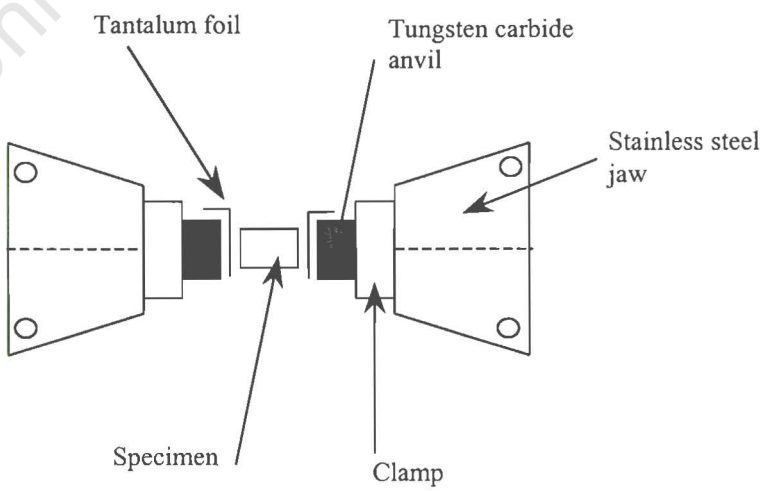

Figure 3.3: Set-up for Gleeble compression testing.

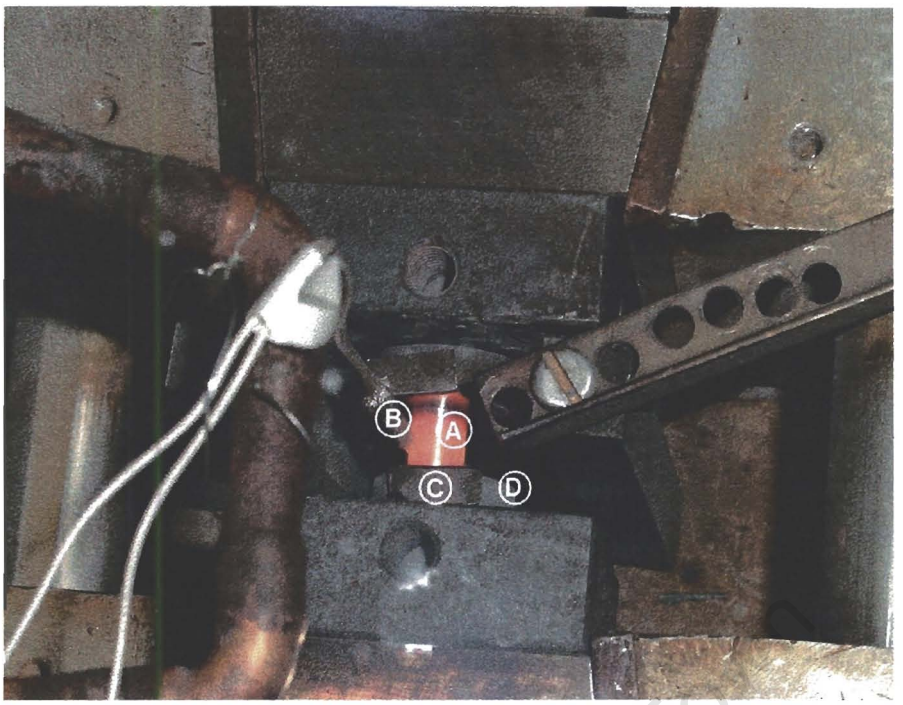

Figure 3.4a: **Photograph of the specimen prior to compression in the Gleeble 1500: (A) Heated specimen (B) Thermocouple (C) Tantalum strip (D) Tungsten-carbide anvil.**

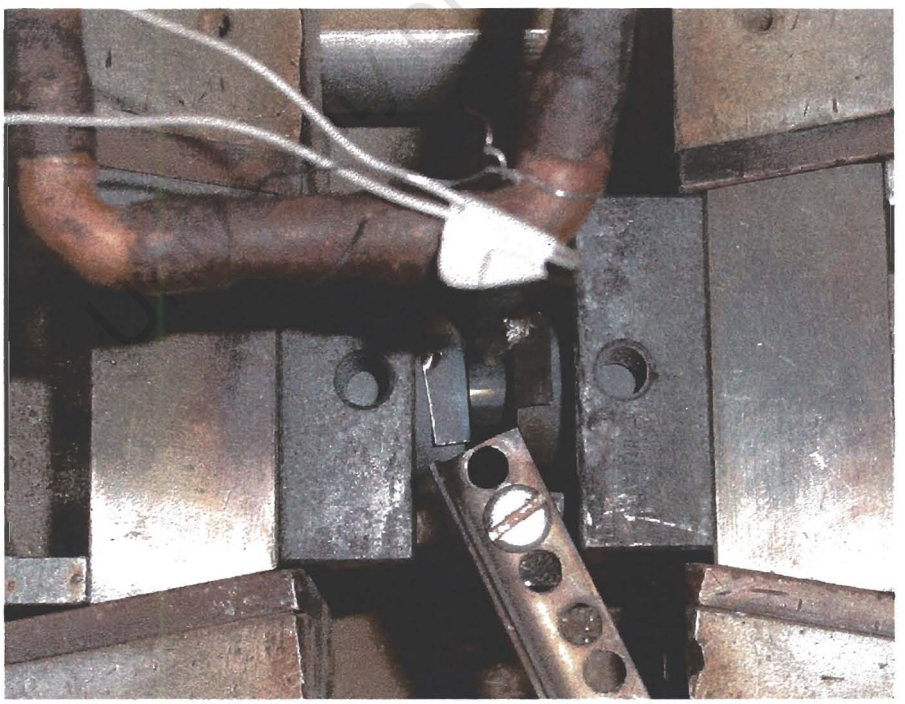

Figure 3.4b: **The specimen immediately after compression and cooling.**

The temperature of the specimen during testing was measured via a platinum thermocouple spot welded to the specimen. A pre-compression was required to hold the specimen between the anvils. Care was taken to ensure that the compression force was sufficient to hold the specimen between the anvils whilst avoiding plastic deformation during heating as the specimen expands. The specimen was held at the deformation temperature for one minute to ensure uniform temperature distribution through the thickness. Immediately following deformation, cooling was effected by helium gas blowing onto the specimen. The time taken for the specimen to cool to a temperature of approximately 150^0C was between 5 and 10 seconds.

3.4.3 Gleeble Deformation Conditions

Initially, simulation in the laboratory was planned to follow the industrial rolling deformation schedule (Appendix A). However, laboratory simulation was limited by the Gleeble deformation parameters. The Gleeble had a maximum strain rate of $1s^{-1}$, whereas industrial strain rates can reach $100s^{-1}$. It was therefore decided that the Zener-Hollomon, Z, parameter would be calculated from the industrial roll schedule and these values would be simulated in the laboratory. Temperatures of over 1500^0C can be obtained using the Gleeble so the Z parameter (which combines strain rate and temperature) was easily obtainable. Each specimen was subjected to a single compression pass to study the effect of the deformation conditions on the initial annealed microstructure. Table 3.2 provides information on the various deformation schedules for testing on the Gleeble.

Z1	Strain Rate (s^{-1})	Temperature (^{0}C)	Strain	Number of Tests	Zener-Hollomon Parameter (s^{-1})
Test 1a	1	850	0.3	6	$3.5x10^{19}$
Test 2a	1	850	0.45	6	$3.5x10^{19}$
Test 3a	1	850	0.65	6	$3.5x10^{19}$
Z2					
Test 1b	1	950	0.3	6	$8.86x10^{17}$
Test 2b	1	950	0.45	6	$8.86x10^{17}$
Test 3b	1	950	0.65	6	$8.86x10^{17}$

Table 3.2: Gleeble 1500 deformation conditions for uni-axial compression testing of AISI 304. Note that the Zener-Hollomon parameters represent values that would be experienced during Steckel Mill rolling.

A shortcoming of the Gleeble 1500 was that it was not possible to produce a uniform strain rate during compression testing. Strain rate is calculated using the equation:

$$\dot{\varepsilon} = \frac{\text{cross-head speed}}{\text{specimen length}} \qquad \textbf{Equation 3.3}$$

During compression testing the specimen length will decrease and thus to maintain a constant strain rate a decreasing cross-head speed would be required to compensate for the change in specimen length. The limitation of the Gleeble 1500 was that the cross-head could only move at a constant speed and consequently a uniform strain rate could not be obtained. To obtain consistency between compression tests it was necessary to decide if the initial specimen length or the final length would be used to calculate the cross-head speed to give either an initial or final strain rate value of 1^{-s}. Table 3.3 shows the variation in the initial and final strain rates depending on which value of length is used in equation 3.3. The initial specimen length was 10mm (specimen dimension) and the final length would correspond to the value that would produce the required amount of strain.

Specimen Length	Strain	Cross-head speed (mms^{-1})	Initial strain rate (s^{-1})	Final strain rate (s^{-1})	Initial less final strain rate (s^{-1})
Initial	0.3	10	1	1.36	0.36
Initial	0.45	10	1	1.57	0.57
Initial	0.65	10	1	1.92	0.92
Final	0.3	7.4	0.74	1	0.26
Final	0.45	6.4	0.64	1	0.36
Final	0.65	5.2	0.52	1	0.48

Table 3.3: Variation in the initial and final strain rates depending on the value of specimen length used in equation 3.3.

It was decided to calculate the cross-head speed for the final length of the compressed specimen. This enabled consistent final Z values to be maintained for each deformation temperature. Therefore, for each of the three different strains, the initial strain rate would be different but at the end of the compression stroke the strain rate would be constant for each deformation condition. Following compression the specimen was removed from the Gleeble and measured, using vernier callipers, to ensure that the desired level of strain had been obtained.

3.5 Annealing Treatments

Each compressed specimen was cut in half (through thickness in the normal-radial direction) to increase the number of annealing treatments that could be performed to study the effect of the deformation history. Figure 3.5 illustrates the directions used to describe the orientation of the specimen.

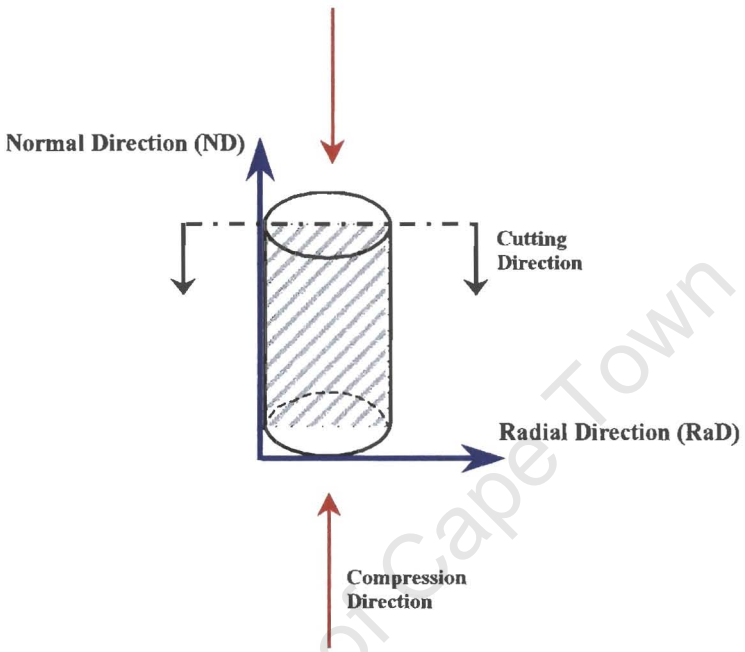

Figure 3.5 Schematic defining the directions used to represent the orientation of specimens.

The deformed specimens were examined using the Reichert light microscope to study the effect of the deformation conditions on the microstructure. The "barrelling" of the specimens during compression produces inhomogeneous deformation conditions through the thickness and it is important that consideration is given to these variations. Lateral spread of the specimen at the anvil-specimen interface is constrained due to friction causing barrelling.

Annealing treatments were performed using the salt bath as this provided rapid isothermal heating of the specimen to the required temperature. Annealing treatments were carried out at temperatures of 800^0C and 900^0C to study the static recrystallization behaviour of the stainless steel. A suitable range of annealing times was essential to produce a complete graph of volume fraction recrystallized i.e. from

0-100% recrystallized. Figure 3.6 illustrates the series of annealing times for the two deformation temperatures and Z parameters. Following annealing the specimen was immediately quenched in water.

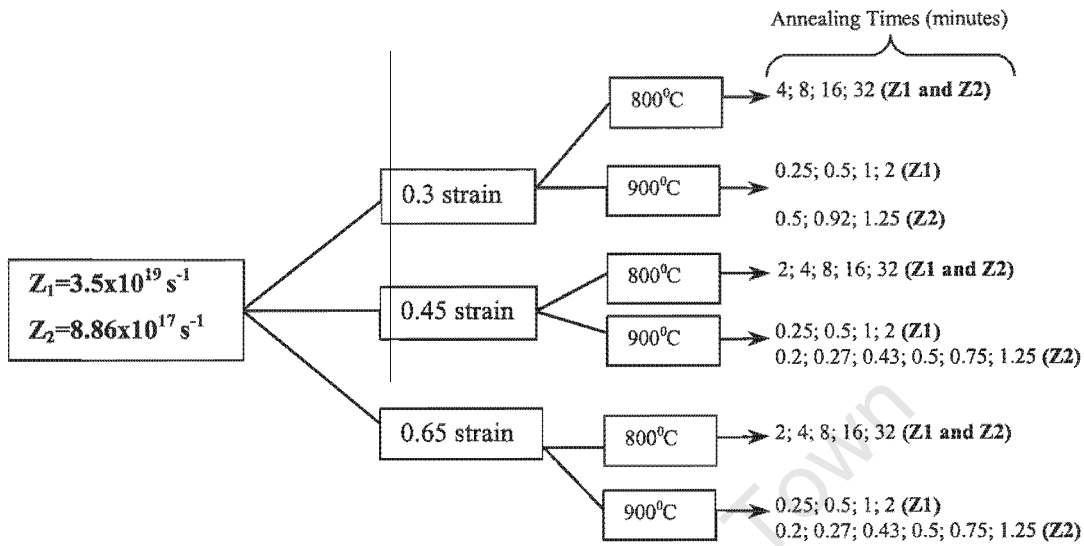

Figure 3.6: **Schematic of the experimental matrix and the sequence of annealing times required to produce a graph of volume fraction recrystallized versus annealing time.**

3.6 Specimen Preparation

The samples were hot mounted in resin to facilitate the grinding and polishing process. Samples were ground and polished using the *Struers* automatic polisher. The *Struers* MD-System™, Method C, was the selected technique used to prepare the specimen surface. Grinding of the specimen was done in two stages: first plane grinding using a silicon carbide abrasive, followed by fine grinding carried out using a 9 μm diamond suspension. A diamond polish, using particles of 3 μm in size, was followed with the final polishing stage being carried out using a suspension of fine colloidal silica. Following polishing, the samples were etched using an electrolytic reagent consisting of 10g oxalic acid in 100ml H_2O, with an applied current of 10V for 45 seconds.

In addition to mechanical polishing, the specimen can be further prepared to increase the quality of the surface. Microstructural examination methods that require a specimen to have a highly polished surface, such as EBSD, need to be electropolished as a final preparation stage. The electropolishing technique removes any residual surface deformation remaining after the final mechanical polishing process has been completed. An electrolyte composition of 133ml glacial acetic acid, 7ml of water and 25 grams of chromic acid (CrO_3) is commonly used to electropolish austenitic stainless steels. The specimen is connected to the circuit and made anodic. A suitable voltage for electropolishing the austenitic stainless steel specimens was 20 volts. Electropolishing for one minute gave a desirable surface finish; however, continuous stirring of the electrolyte solution was necessary to prevent bubble formation, which could cause uneven polishing. Continued use of the same electrolyte can lead to an increase in current density and less efficient polishing as the temperature of the electrolyte increases. After one minute of electropolishing, each specimen was examined using the Reichert MeF3-A light microscope to ensure that the polishing conditions were producing the same results.

Micrographs were taken at a specified location using the Reichert MeF3-A light microscope. Due to the inhomogeneous deformation microstructure resulting from barrelling, it was important that micrographs, hardness tests and EBSD maps were performed at consistent locations. Figure 3.7 illustrates the selected area of examination.

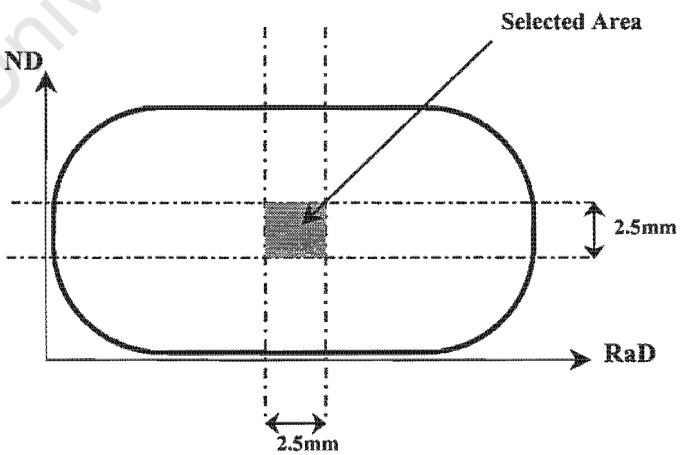

Figure 3.7: **Through-thickness section of deformed specimen showing the area selected for microstructural examination.**

3.7 Determining Softening Kinetics

3.7.1 Hardness Testing

Hardness tests were performed using the Matsuzawa MXT α7 digital microhardness tester. To ensure consistency, indentations were performed in the specified area (see figure 3.7). A Vickers indentor of 1000gf was selected as this provided an adequate indentation area. Individual indents were spaced at least three diagonals away from each other to ensure that readings were not affected by the plastic zone that surrounds an indentation. Seven indentations were performed per specimen and the average value was plotted against annealing time to determine softening behaviour.

3.7.2 Grain Growth Effects

The relationship between hardness and annealing time provides an indication of the materials softening kinetics for a particular annealing temperature and prior deformation condition. However, once complete softening has been achieved the graph continues to exhibit a decline in hardness with annealing time due to growth of the recrystallized grains. The relationship between grain size and strength/hardness can be given by the Hall-Petch equation[1]:

$$\sigma_y = \sigma_o + k_y d^{-1/2} \qquad \textbf{Equation 3.4}$$

Where: σ_y is the yield strength

σ_o is the strength of the material with infinite grain size

k_y is a material constant

d is the grain size

Therefore, there will exist a transition point on the graph where the hardness decrease is based on the relationship between hardness and grain size and not softening kinetics related to recrystallization. Figure 3.8 illustrates the two regimes for a hypothetical graph of hardness versus annealing time. Regime 1 represents the reduction in hardness due to recrystallization. There is a transition point and then regime 2, which represents grain growth effects.

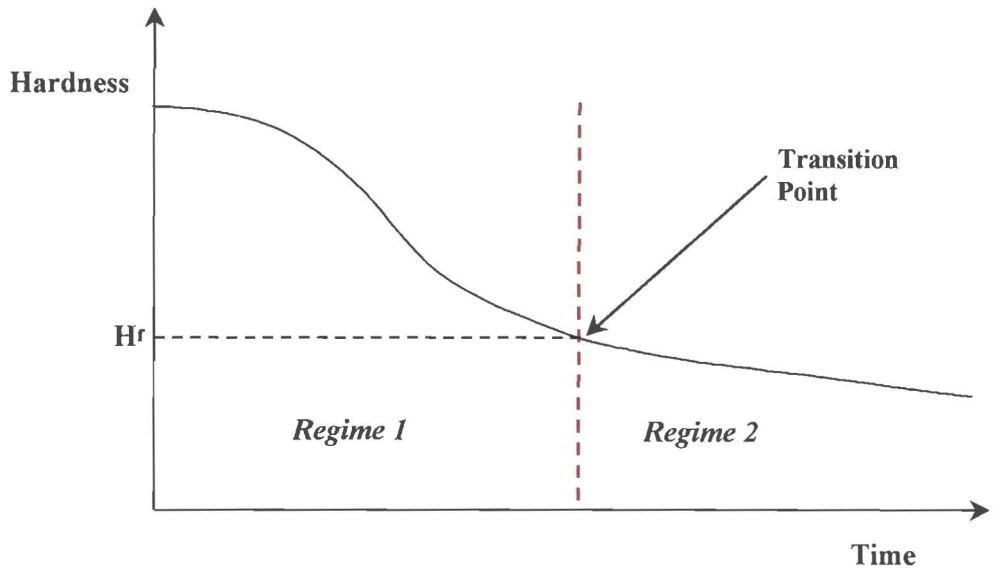

Figure 3.8: **Schematic illustrating the hypothetical relationship between hardness and annealing time. Regime 1 is due to recrystallization, whilst the hardness decrease in regime 2 is the result of grain growth. H_f would be the hardness value at the point of complete softening by recrystallization, but before grain growth effects.**

The final hardness value due exclusively to recrystallization, H_f, is an important parameter in the interpretation of softening kinetics. The fraction of material softened, X_s, is calculated from the hardness versus time data using the following relationship:

$$X_s = \frac{H_i - H}{H_i - H_f} \qquad \textbf{Equation 3.5}$$

Where: H_i = initial value of deformed hardness
H = instantaneous value of hardness
H_f = final value of hardness

To experimentally determine the accurate value of H_f, the specimen would need to be annealed for the precise time that produced 100% softening, but before grain growth. This would be an arduous task and unlikely to yield precise results. Therefore, an alternative method was used in this study to determine the approximate hardness value at the point of complete softening for each deformation condition and annealing temperature.

3.7.3 Calculating H_f

It would be expected that the graph of hardness versus annealing time would exhibit a shape change at the transition point due to different mechanisms governing the hardness decrease. This is a reasonable method to assume, as the hardness decrease during recrystallization is greater than the decrease in hardness associated with grain growth for a given annealing period. Therefore, a type of "reverse extrapolation" method was used to determine the transition point between the two regimes. A straight line is plotted, beginning at the point of final annealing time, such that it traces the plateau region of the hardness versus time graph, as shown by the black line in figure 3.9. The deviation point, of the straight line from the graph, is considered the transition point due to the abrupt shape change. This method of determining final hardness was consistent for each deformation condition and annealing temperature.

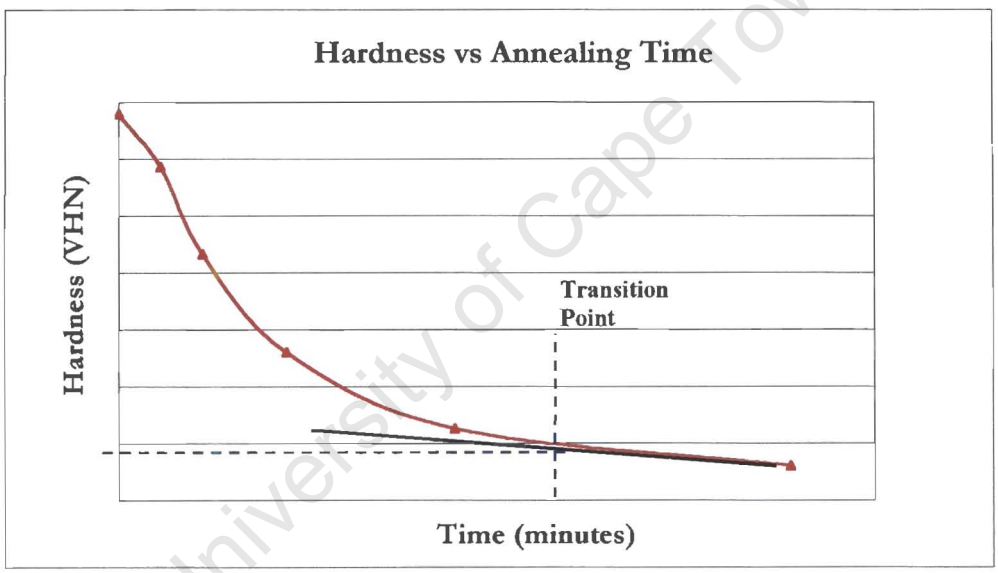

Figure 3.9: **Method used to calculate the approximate hardness value at the point of complete softening before the effects of grain growth. The black line is plotted to identify the deviation point corresponding to the annealing time at which complete softening is achieved. Final hardness, H_f, is then determined from the graph at that point.**

3.8 Electron Back-Scattered Diffraction

3.8.1 Introduction

Electron back-scattered diffraction (EBSD) is a technique involving the formation of diffraction patterns that represent the geometry of a material's crystal planes. Kikuchi[52] was the first to observe these patterns in 1928 while studying the electron diffraction patterns from thin films of mica. However, work done by Venables et al[53] in 1973 introduced the technique of electron back-scattered diffraction to the scanning electron microscope (SEM). Since that time there has been a significant improvement in EBSD technology and in recent years it has become an established method for microtexture measurement[54]. EBSD is also a useful method for distinguishing between recrystallized, recovered and deformed regions in a material but this technique is still in its infancy and is only beginning to gain popularity[55, 56, 57].

The electron back-scattered pattern (EBSP) is formed when electrons impinge on crystal planes and satisfy the Bragg condition, which is given by the equation:

$$2d\sin\theta_B = n\lambda$$

where d is the interplanar spacing, θ_B is the Bragg angle, n is the order of reflection and λ is the electron wavelength. Electrons that satisfy the equation are diffracted through the Bragg angle and this produces two cones of electrons radiating from a single set of planes as shown in figure 3.10.

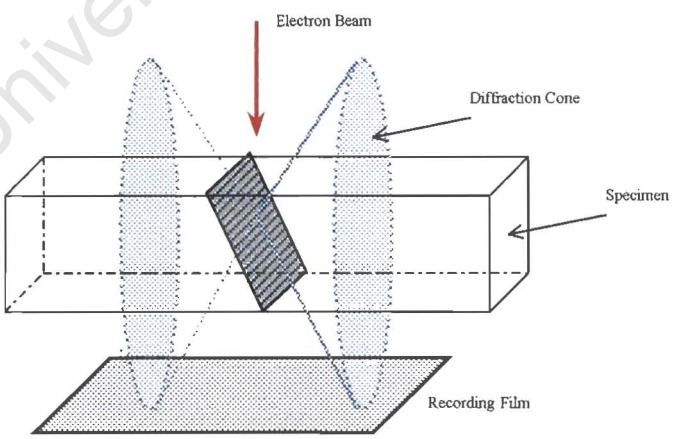

Figure 3.10: Diffraction cones formed by electrons impinging upon crystal planes and satisfying the Bragg condition.

If an imaging capturing device, such as a phosphor screen, is placed such that it intersects the cones of radiating electrons a diffraction pattern will be produced. The reflected cones have a large apex angle, hence a pattern imaged on a phosphor screen will only represent a small section of the cone, and these appear as a pair of parallel lines known as Kikuchi bands. Figure 3.11 shows the Kikuchi bands imaged on a monitor.

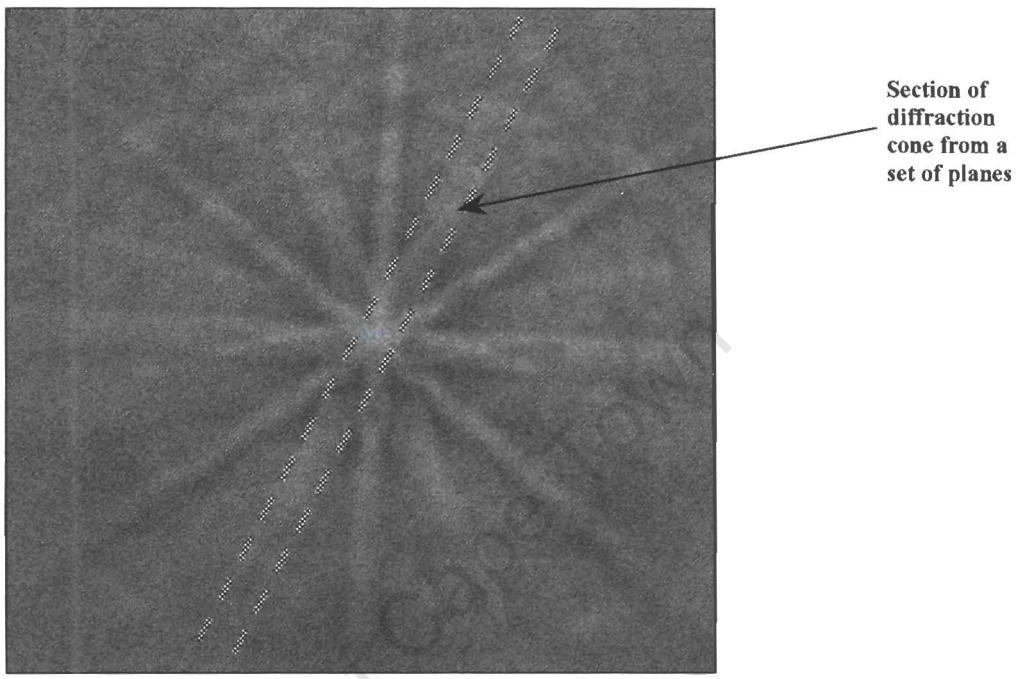

Figure 3.11 **Example of an electron back-scattered pattern for AISI 304 stainless steel (f.c.c. structure) showing the linear features known as Kikuchi bands.**

3.8.2 Determining EBSP

Specimen preparation is an important aspect in obtaining a diffraction pattern. A highly polished surface is required to remove any deformation that will be deleterious to the pattern formation. A highly strained or deformed material contains dislocations that distort lattice planes and prevent pattern formation due to the electrons being scattered away from the Bragg condition. The sensitivity of pattern quality on the amount of strain extends to the degree where conventional grinding and mechanical polishing introduces too much strain into the top layer of the specimen surface. Thus, it is required that the specimen is electropolished to remove residual deformation following the mechanical polishing stage (see section 3.6 for electropolishing procedure).

The Leica Stereoscan 200 SEM located at the Electron Microscope Unit, University of Cape Town, was used to perform EBSD analysis. A low-light television camera is mounted on the side of the SEM chamber behind the phosphor screen. The phosphor screen is approximately 50mm in diameter and positioned directly in front of the specimen surface to capture the diffracted electrons. The EBSD camera records the pattern imaged on the phosphor screen and the data is transferred to a Hamamatsu ARGUS-20 image processor where the recorded pattern can be enhanced. In addition to the electrons that satisfy the Bragg condition and form clear Kikuchi bands, there is also a significant amount of inelastic scattering of electrons that contribute to a diffuse background. The EBSD software has a background correction feature that improves the signal-to-noise ratio and enhances Kikuchi bands on the image processor (see figure 3.11). The ARGUS-20 image processor is connected to a computer where HKL-EBSD acquisition software will automatically index the diffraction pattern; a set of Euler angles is assigned to the indexed point and the data is saved to a file. As the beam crosses into a different orientated lattice plane the image will alter and a new diffraction pattern will be indexed and saved which forms a map of the materials microstructure, known as an orientation map. The EBSD imaging software assigns a colour to each set of Euler angles to enable clear visual distinction between adjacent grains. Figure 3.12 illustrates an orientation map and the effective use of colour to produce a clear representation of the material's microstructure.

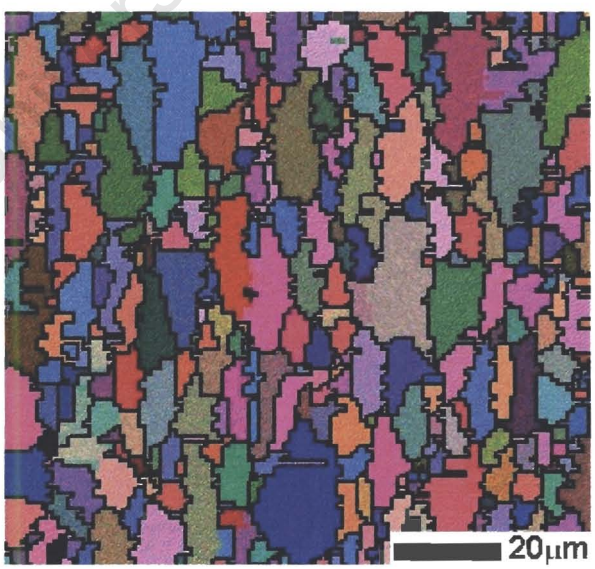

Figure 3.12: Orientation map of AISI 304 stainless steel using Euler colours.

An orientation map is automatically produced by the EBSD system controlling either the electron beam or the specimen stage during acquisition. Beam scanning was selected as the method to obtain the orientation maps as it is less time consuming than stage scanning but the disadvantage is that for a larger scanning area beam focussing problems develop. For a specimen with a small grain size beam scanning is adequate, as a relatively small scan area will provide suitable information regarding the microstructure. A scan area of 200μm x 200μm, where the beam is scanned over the specimen surface, was found to be suitable and required a time of approximately 4.5 hours to complete. HKL acquisition software is able to capture, index and store diffraction pattern data in approximately 0.38 seconds for each point. Thus, in a 4.5 hour map a total of 43000 points will be indexed. The time for a map to be completed also depends on the step size; defined as the distance the beam will move from one indexed point to the next indexing position. A small step size provides a more detailed map of the microstructure but increases the time of acquisition. A step size of 1μm was found to give a good compromise between pattern quality and acquisition time.

The specimen is positioned in front of the phosphor screen at a predetermined angle of tilt. A large angle of tilt is required to obtain a high percentage of back-scattered electrons. If the angle of tilt is too small, the electrons tend to be absorbed by the specimen instead of diffracted. It is for this reason that the specimen was tilted at 70^0 from the horizontal. However, a drawback of having the specimen tilted at 70^0 means that only a limited area of the specimen is in focus and this limits the area that can be mapped using the beam scanning method. This was taken into account when the scan area was set on the computer. The surface prepared for analysis was the normal-radial direction as this allows through thickness measurements to be performed on the specimen. Figure 3.13 shows the positioning of the specimen in the SEM chamber.

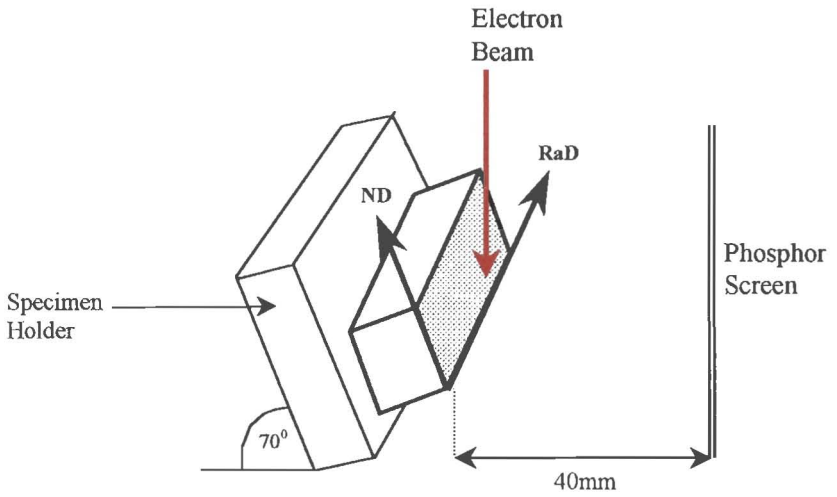

Figure 3.13: Schematic showing the specimen positioning inside the SEM chamber.

The HKL software acquisition programme requires information relating to material properties and SEM operating conditions in order to define the diffraction pattern. Optimal pattern imaging was obtained by setting the accelerating voltage to 25kv and an objective aperture of 50μm. The working distance was set to 23mm with a stage tilt of 70^0. The user specifies SEM information and specimen crystallographic structure prior to EBSP acquisition.

3.8.3 Evaluating Fraction Recrystallized

The above section introduced the procedure to obtain the raw EBSD data. However, to glean information from the data, a post processing software application is required to interpret the results. Post-processing analysis of the EBSD maps was performed using VMAP* software. VMAP is able to determine, amongst other microstructural features, the percentage of material recrystallized from the sampled area. The ability of VMAP software to provide a determination of fraction recrystallized is an essential component of this study, enabling a comparison to be made between fraction softened and fraction recrystallized.

Prior to determining fraction recrystallized, the VMAP software performs a "grain reconstruction" routine, enabling the program to recognise deformed and recrystallized areas. Each data point (or pixel) has an associated orientation value that

* VMAP is a program for displaying and analysing data obtained from EBSD. The program was written by John Humphreys, Manchester Materials Science Centre.

forms the basis of the reconstruction method. A grain is constructed by identifying a reference pixel and then classifying whether adjacent pixels belong to the same grain or subgrain based on the misorientation. If the misorientation of adjacent pixels is greater than the high angle grain boundary (HAGB) setting then the pixels are deemed to belong to a different grain. The "new grain" pixel is then classified as the reference pixel and the process continues until the complete map is constructed. VMAP allows two methods to reconstruct the acquired EBSD map depending on user preference.

3.8.4 Relative Referencing

This method of reconstruction classifies a grain or subgrain based on the misorientation between adjacent pixels. This is illustrated schematically in figure 3.14. The misorientation is measured between the reference pixel and pixel 2. If the misorientation is less than the HAGB setting then the pixel is deemed to belong to the same grain. The next misorientation is then measured between pixel 2 and 3 i.e. pixel 2 now becomes the reference pixel. A grain boundary will be inserted where the misorientation between adjacent pixels is greater than the HAGB setting. Using this method of reconstructing, if a deformed grain has a gradual change in orientation it would be classified as recrystallized, since the reconstruction method only calculates misorientation of adjacent points.

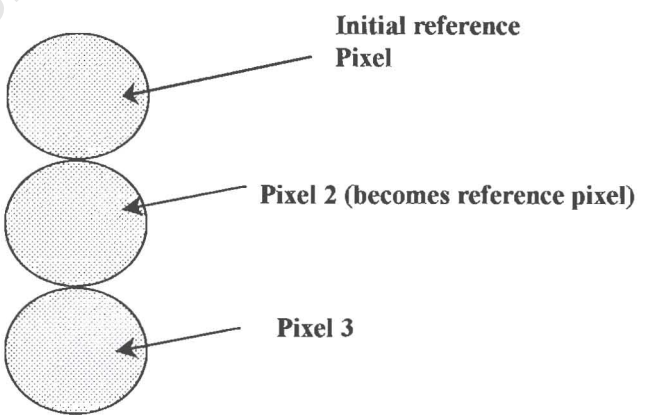

Figure 3.14: **Schematic representation of relative referencing as a grain reconstruction technique. The reconstruction is based on the misorientation between adjacent pixels.**

3.8.5 Absolute Referencing

During reconstruction, a pixel is deemed to belong to a particular grain or subgrain based on the misorientation to the original pixel i.e. the misorientation of pixel 3 in figure 3.14 would be calculated relative to the initial reference pixel and not pixel 2. This method provides a clearer representation of the strain distribution within the grain, which is an essential consideration when calculating recrystallized fraction. Therefore, absolute referencing was used in this study to determine volume fraction recrystallized. Figure 3.15 illustrates the effect of each method on the reconstructed map for identical areas. The Euler colours have been omitted from the EBSD maps in figure 3.15 to more clearly emphasise the grain and subgrain boundaries, which are coloured black and blue respectively.

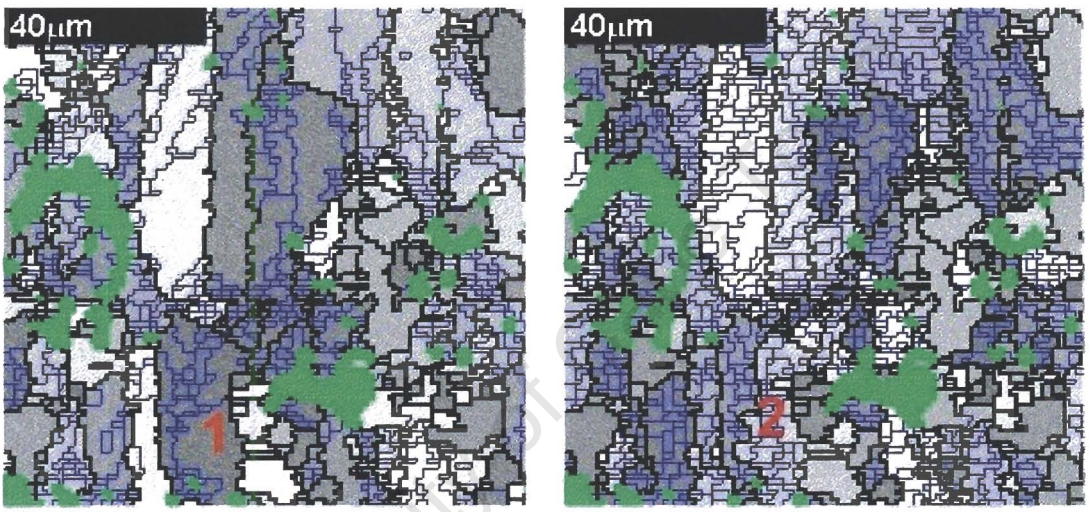

Figure 3.15: **A comparison of the EBSD maps obtained using (a) relative referencing and (b) absolute referencing. Points 1 and 2 illustrate the different positions of a HAGB depending on which method is used for reconstruction.**

Using absolute referencing a point defined on the map as a subgrain or grain boundary may be due to an accumulation in the misorientation within the grain. Therefore, it is essential when using absolute referencing that the position of a boundary on the reconstructed map is not interpreted to be a boundary under the classical definition of a subgrain or grain boundary. Figure 3.15, areas marked 1 and 2, effectively illustrates the difference in boundary positions using absolute and relative methods. It would be expected that relative referencing would provide a more accurate representation of "actual" HAGB as the misorientation is measured between adjacent pixels, but absolute referencing better describes the misorientation (or strain) gradient.

Following grain reconstruction the software can determine fraction recrystallized. VMAP defines a recrystallized grain as one that is surrounded by more than 50% of high angle grain boundaries. This is an arbitrary definition used in the VMAP software and should be used with discretion.

It is normal for an EBSD map to contain areas that have not been indexed due to poor pattern quality at that point. Areas such as grain boundaries, pits or regions out of focus can result in non-indexed points, as the diffraction pattern will be distorted at these positions. Furthermore, highly deformed areas can produce non-indexed points due to the poor pattern quality. The VMAP software excludes non-indexed points from its recrystallized fraction results i.e. it only provides a percentage recrystallized fraction for the areas that have been indexed. However, in terms of studying deformation microstructure, it is important that the non-indexed areas are considered in the final recrystallization calculation. In a highly deformed microstructure, there can be a high fraction of non-indexed points due to deformation. Therefore, an effective method was required to distinguish between non-indexed points due to "normal" microstructural inhomogeneities and genuine deformed areas.

A proposed solution was to use a standard method of eliminating normal microstructural inhomogeneities from the non-indexed fraction. VMAP has a "noise reduction" routine that is able to treat certain non-indexed points as indexed points. The noise reduction routine assigns an orientation to a non-indexed point based on the orientations of the neighbouring indexed points. Level 3 of this routine was used in this study, which means that a non-indexed point needed to have a minimum of five indexed neighbours to be assigned an orientation. It has been assumed that the noise reduction routine will eliminate non-indexed points associated with normal microstructural inhomogeneities. Thus, remaining non-indexed points are regarded as regions that are deformed and are unable to be indexed due to poor pattern quality arising from high dislocation density. It is realized that the remaining non-indexed points are an approximation of the deformed areas and subject to user interpretation. Consistency was therefore essential when using the routine for evaluating recrystallized fraction for each map. The non-indexed points are shown as green areas on the EBSD maps (see figure 3.15).

Chapter 4

Results and Discussion

4.1 Deformation Analysis

4.1.1 Introduction

Specimens were deformed in an attempt to improve the understanding of annealing behaviour following high temperature deformation. Deformation conditions were chosen to simulate the industrial hot rolling schedule used to produce rolled plate (Appendix A). Specimens were deformed at temperatures of 850^0C and 950^0C producing two Z parameters, Z1 and Z2 with values of $3.5x10^{19}$ and $8.86x10^{17}$ s^{-1} respectively. Annealing temperatures, 800^0C and 900^0C, were also selected to imitate interpass temperatures encountered during hot rolling. It was intended that the different temperatures would incorporate the two extremes expected during interpass annealing.

The grain size prior to deformation, D_o, is an important parameter that will affect recrystallization rates during annealing experiments. Therefore, to obtain representative annealing data the D_o value would need to be consistent for each specimen. The following section introduces the annealing treatment that was performed to ensure a consistent D_o.

4.1.2 Microstructure Preparation

The specimens that were sectioned from the 25mm rolled plate, supplied by Columbus Stainless, required an annealing treatment to homogenise the microstructure. A completely strain free microstructure was required prior to testing to ensure that the deformed microstructure was representative of the deformation conditions. The annealing treatments, to homogenise the microstructure, were preformed in a salt bath at a temperature of 1050^0C for twenty minutes. Figures 4.1 and 4.2 illustrate the as received and the fully homogenised microstructure respectively. The initial grain size, 20μm, which is included in the $t_{0.5}$ equation as D_o, was obtained from an EBSD map, see figure 4.3.

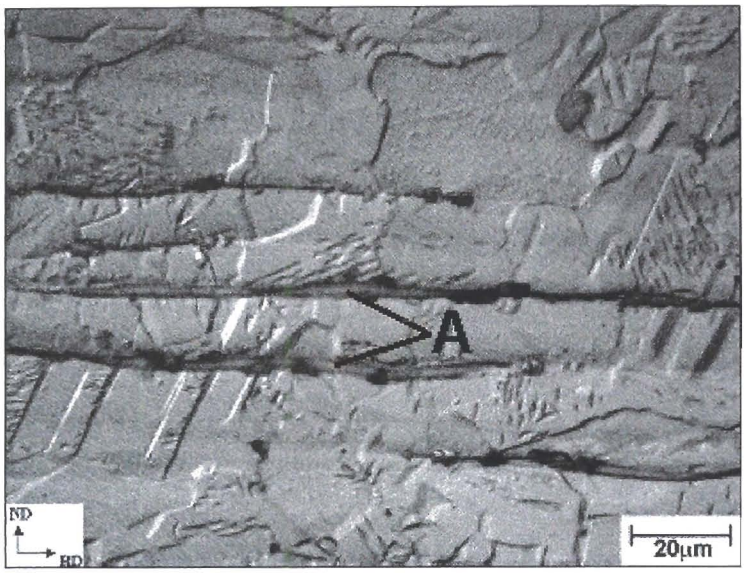

Figure 4.1:
The microstructure of the rolled plate supplied by Columbus Stainless prior to annealing.

A: Ferrite stringers

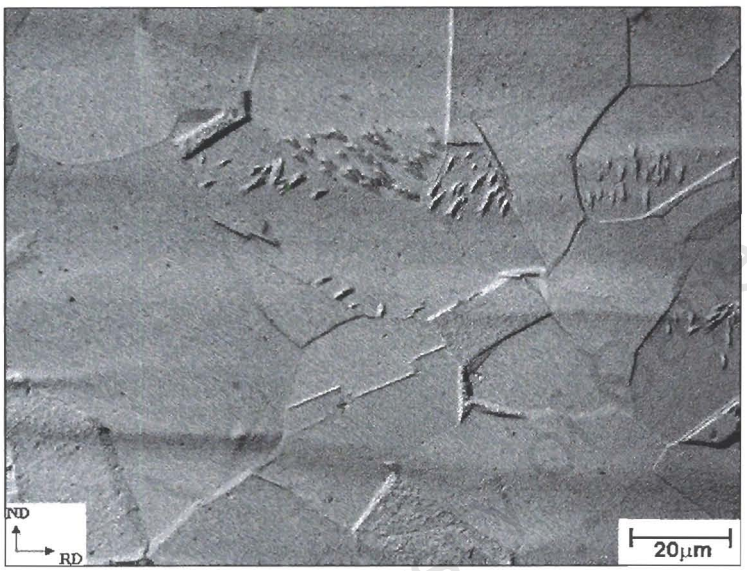

Figure 4.2:
Micrograph of the fully recrystallized microstructure prior to deformation. Annealed for 20 minutes.

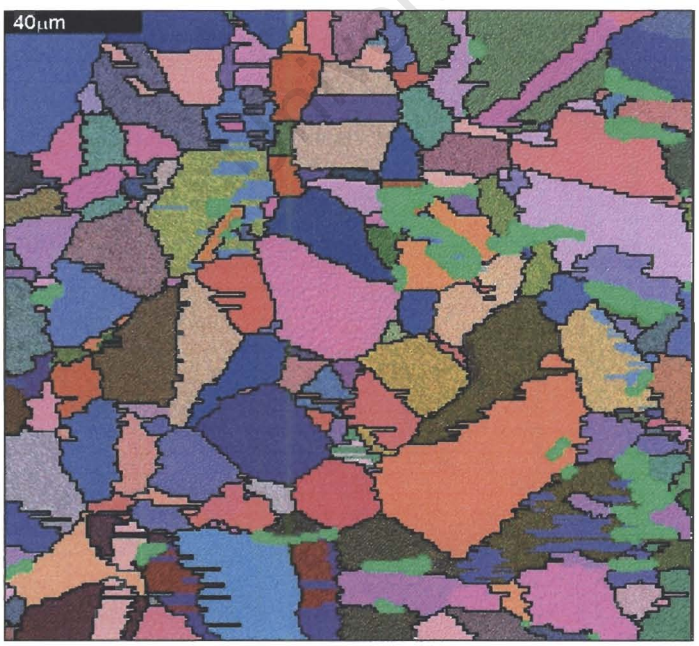

Figure 4.3:
An example of an EBSD map of the annealed microstructure used to calculate initial grain size, D_o.

4.1.3 Inhomogeneous Deformation

A common phenomenon during uni-axial compression testing is barrelling of the specimen due to friction at the specimen-anvil interface. The friction effect restrains lateral movement of the specimen immediately beneath the anvils. For ideal conditions of zero friction at the loading interface, the specimen will deform uniformly without barrelling. However, frictional forces are unavoidable in practice and the specimen acquires a barrelled shape, as shown in figure 4.4. A feature of barrelling is a material "roll over" process at the loading face. Material originally located on the side of the specimen, rolls over and becomes part of the specimen loading face. Therefore, the observed specimen end diameter is increased and consequently the load is distributed over a larger area. A simulation of the roll over effect for a stainless steel specimen compressed uni-axially is shown in figures 4.5a and b. Point A, in figure 4.5a, originally located on the circumference of the undeformed specimen has rolled over and become part of the loaded face as shown in figure 4.5b. The grid pattern in figures 4.5a and b illustrates the flow pattern of the material in the region of roll over.

4.1.4 Barrelling in the Gleeble 1500

The uni-axial compression experiments performed in this study resulted in barrelling of the cylindrical specimens (see figure 4.4). Figure 4.6 illustrates through-thickness microstructural variation in a specimen compressed to a strain of 0.65. The region directly under the loading face shows a relatively undeformed conical region, bordered by a zone heavily deformed in shear. The most heavily deformed zone is at the specimen centre. Hardness tests were performed at areas A-C indicated in figure 4.6 to evaluate the microstructural deformation distribution, whilst micrographs of areas A-C are shown in figures 4.7a-c. A comparison of the hardness results shows that the area directly under the loading face, 218 VHN, was significantly less than the hardness in the centre of the specimen, 261VHN. The limited deformation, area A, is clearly illustrated by comparing figure 4.7a with the region of heavy deformation in the centre, figure 4.7b. The effect of roll over and the accompanying shear effects are shown in figure 4.7c. The high hardness value in region C, 278 VHN, is attributed to the extensive shear during deformation.

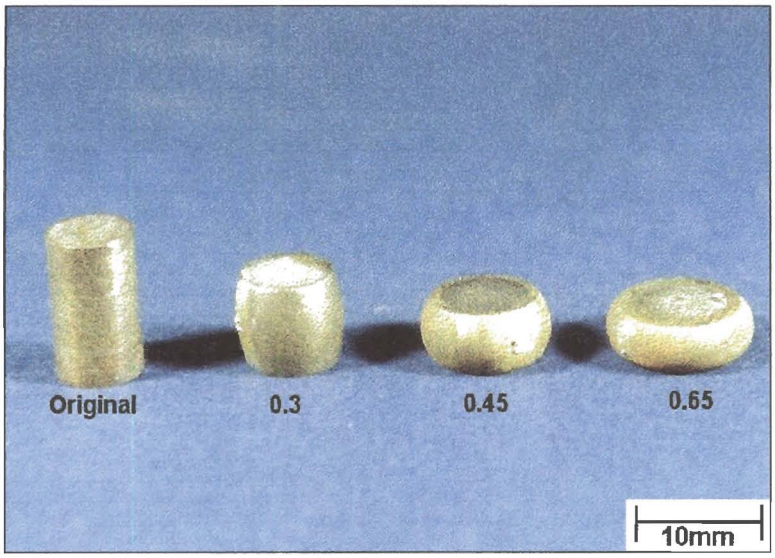

Figure 4.4:
Barrelling of the cylindrical specimens for the three levels of strain used in this study.

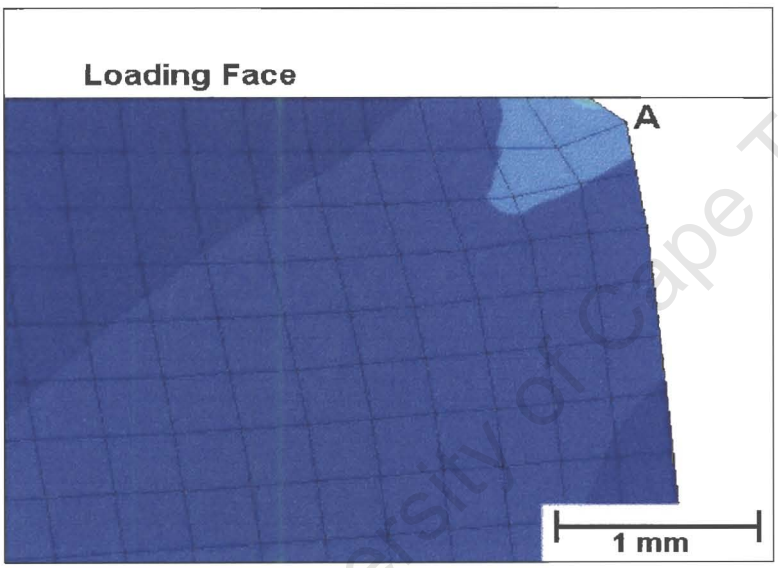

Figure 4.5a:
Simulation illustrating the position of point A prior to deformation. The material at point A is located on the circumference of the loading face.

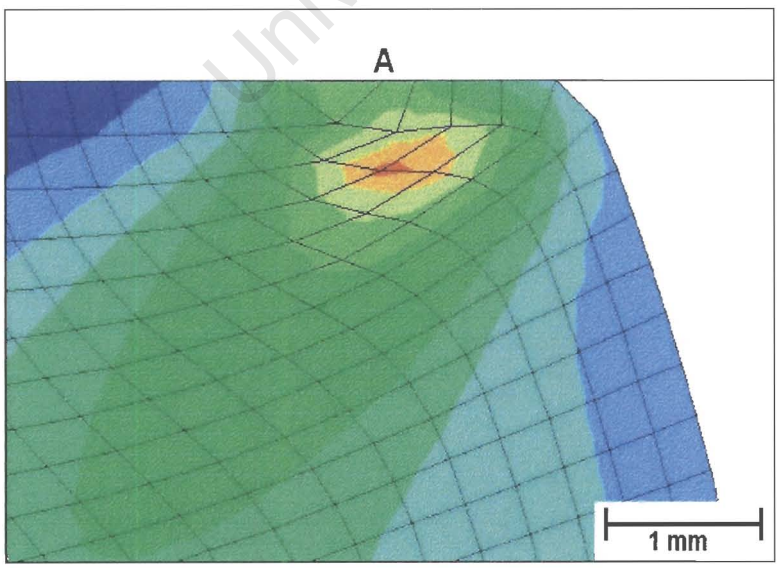

Figure 4.5b:
At a strain of 0.6 the material has rolled over and become part of the specimen loading face.

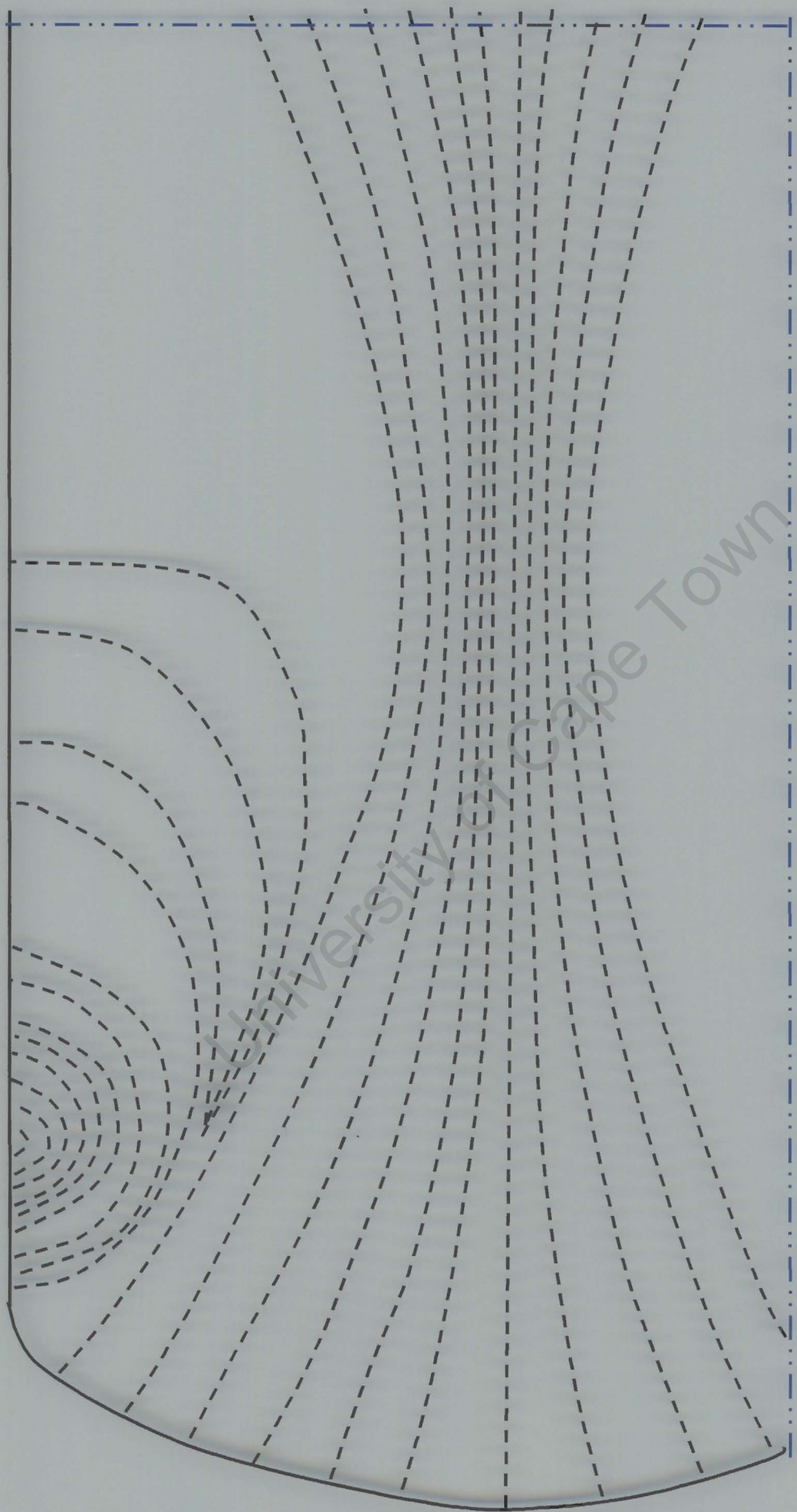

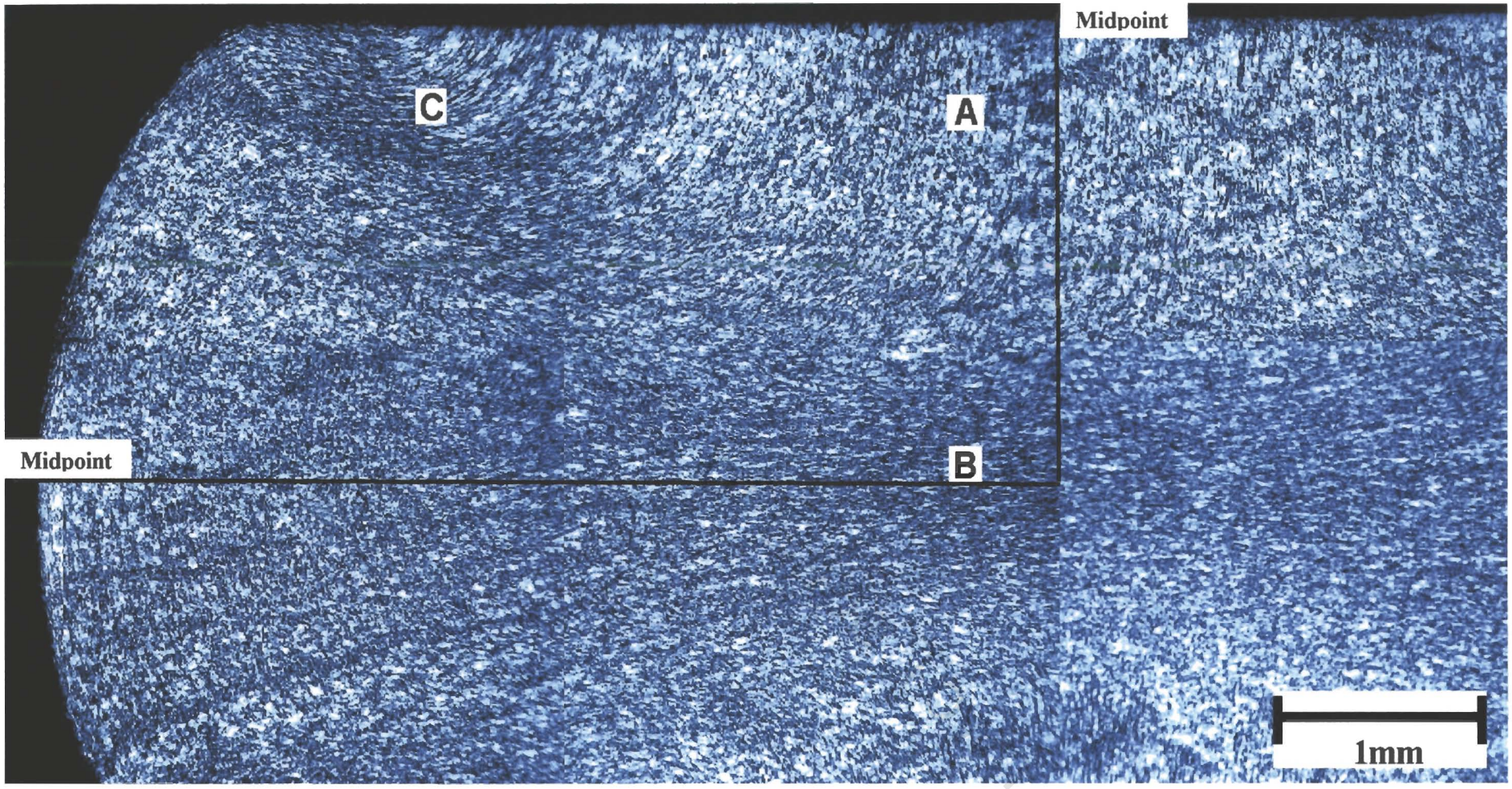

Figure 4.6: Montage of the through-thickness microstructural variation in a specimen deformed to a strain of 0.65. The overlay illustrates the flow pattern that develops due to barrelling. Figures 4.7a-c are more detailed micrographs of areas A-C.
A = 218 VHN
B = 261 VHN
C = 278 VHN

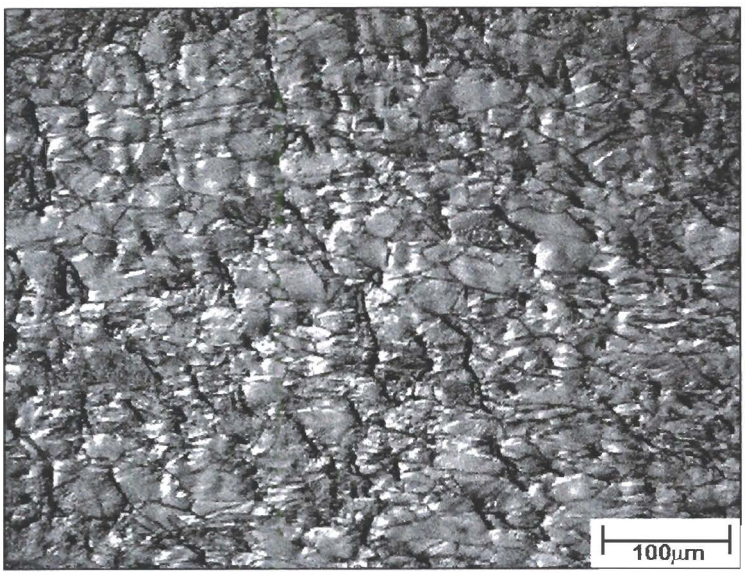

Figure 4.7a:
Region A in figure 4.6. Equiaxed grain structure in slightly deformed region.

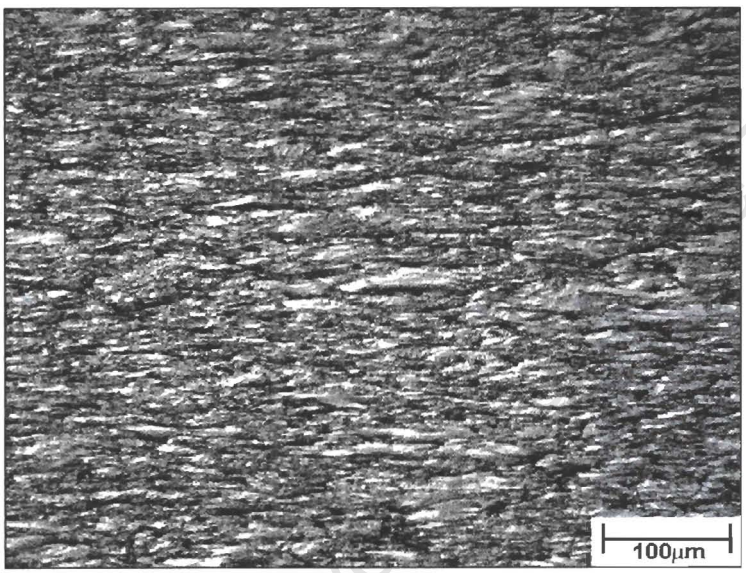

Figure 4.7b:
Heavy deformation in centre of compressed specimen (region B in figure 4.6).

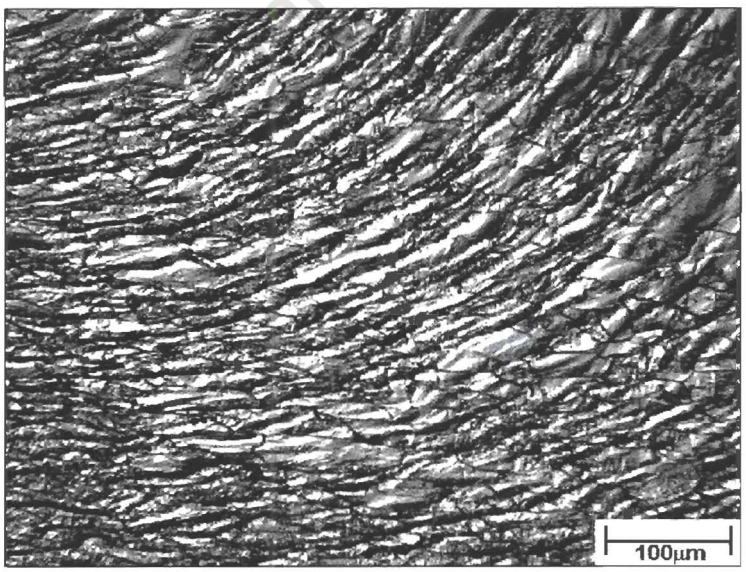

Figure 4.7c:
Extensive shear in the region of material roll over (region C in figure 4.6).

4.1.5 Quantifying Effective Strain in Designated Area

The importance of considering barrelling in this study is that the nominal strain will not be equal to the effective strain due to non-uniform deformation. In terms of quantifying recrystallization kinetics it was imperative that the effective strain was known for each deformation condition. To maintain consistency a designated area of the specimen was selected for all microstructural testing and examination (see figure 3.7 in Chapter 3). A finite element (FE) computer simulation was developed to calculate the effective strain within the designated testing area.

FE simulations are capable of determining material flow, temperature distribution and the effective stress and strain patterns in a deformed specimen. The computer simulation requires data describing the materials flow stress behaviour for the particular deformation temperature and the friction coefficient at the specimen-anvil interface.

The Gleeble 1500 was unable to provide an adequate flow curve for the deformed specimens. Flow curve data was thus obtained using results found by Floweday[58] for high temperature deformation of AISI 304 stainless steel, as shown in figure 4.8. The friction coefficient, f, was calculated by firstly entering an estimated value into the FE simulation. The width of the actual barrelled specimen is then measured and related to the simulated FE model width. Therefore, f can be altered to satisfy the condition of the measured width equalling the simulated width. Based on the comparison of simulated width and actual measured width, the f value was found to equal 0.3. It is realised that the method used to calculate the f value assumes the FE analysis is representative of the experimental data. However, the effective strain result is not sensitive to small changes in the f value and therefore a high degree of accuracy is not required in the determination of f; this will therefore account for any discrepancy in the comparison of simulated and actual barrelled width measurements. Figure 4.9 illustrates the change in the effective strain results for different f values. For comparative purposes the effect of zero f is shown in figure 4.9.

Figure 4.10 illustrates the strain distribution, of the barrelled specimens, obtained from FE simulations. Due to symmetry it is required that only a quarter of the

specimen is modelled to obtain a representation of the strain distribution, as shown in figure 4.10. Table 4.1 illustrates the difference in the nominal strain and the effective strain calculated using FE data. The FE results presented in table 4.1 correspond to the values of strain within the designated testing area.

Nominal strain	Effective strain
0.3	0.52
0.45	0.85
0.65	1.25

Table 4.1: **Difference between the nominal strain and the effective strain due to the inhomogeneous deformation microstructure. The effective strain values in the designated testing area are calculated using FE analysis.**

Based on the above discussion it is apparent that the nominal strain value does not correspond to the effective strain within the testing area. Therefore, strain values are hereafter discussed with reference to the effective strain values presented in Table 4.1.

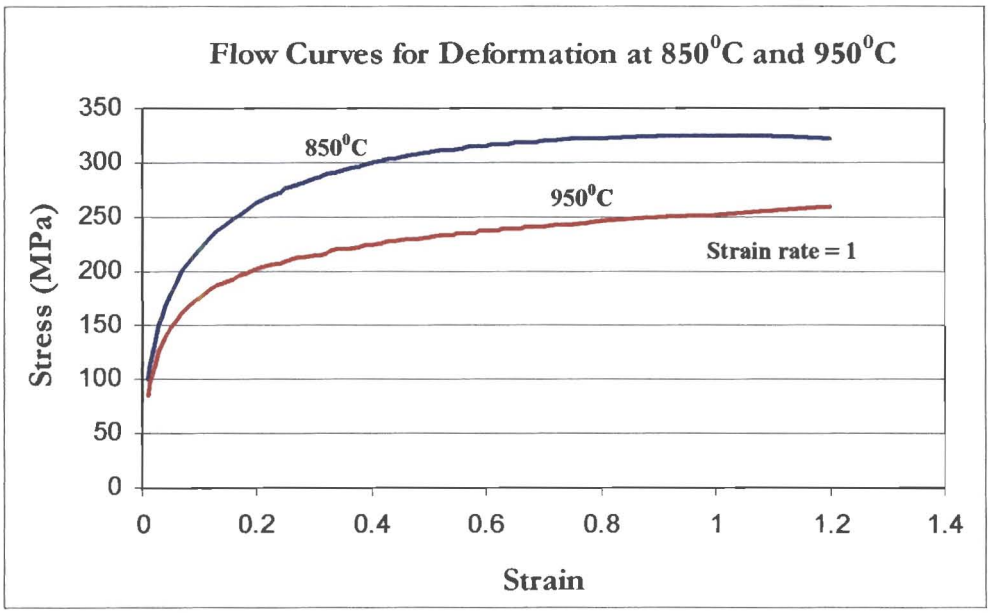

Figure 4.8: **Flow curve data for deformation at the two temperatures and strain rate used in this study[58].**

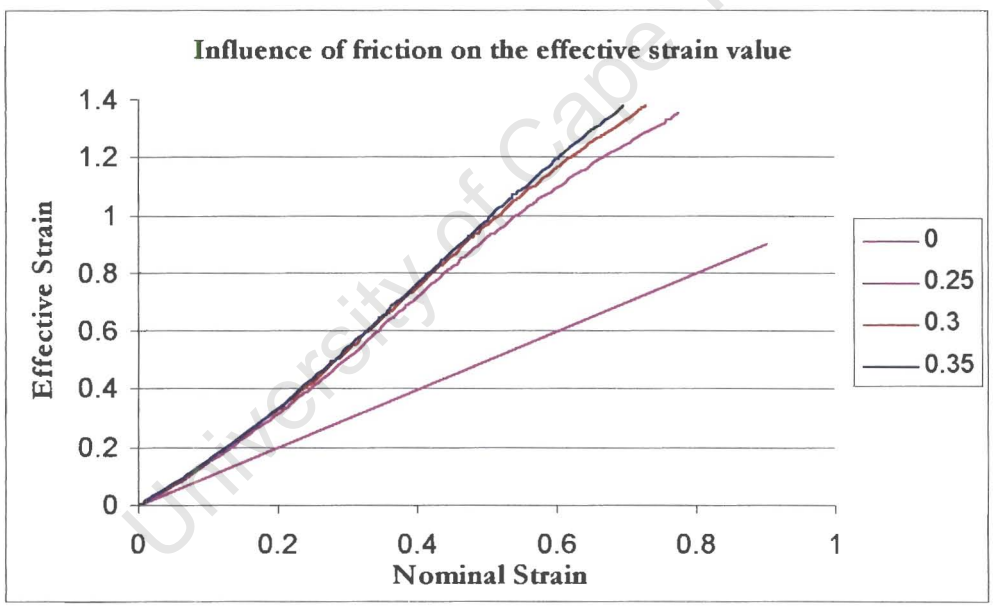

Figure 4.9: **The effect of different *f* values, used in the FEM analysis, on the effective strain values.**

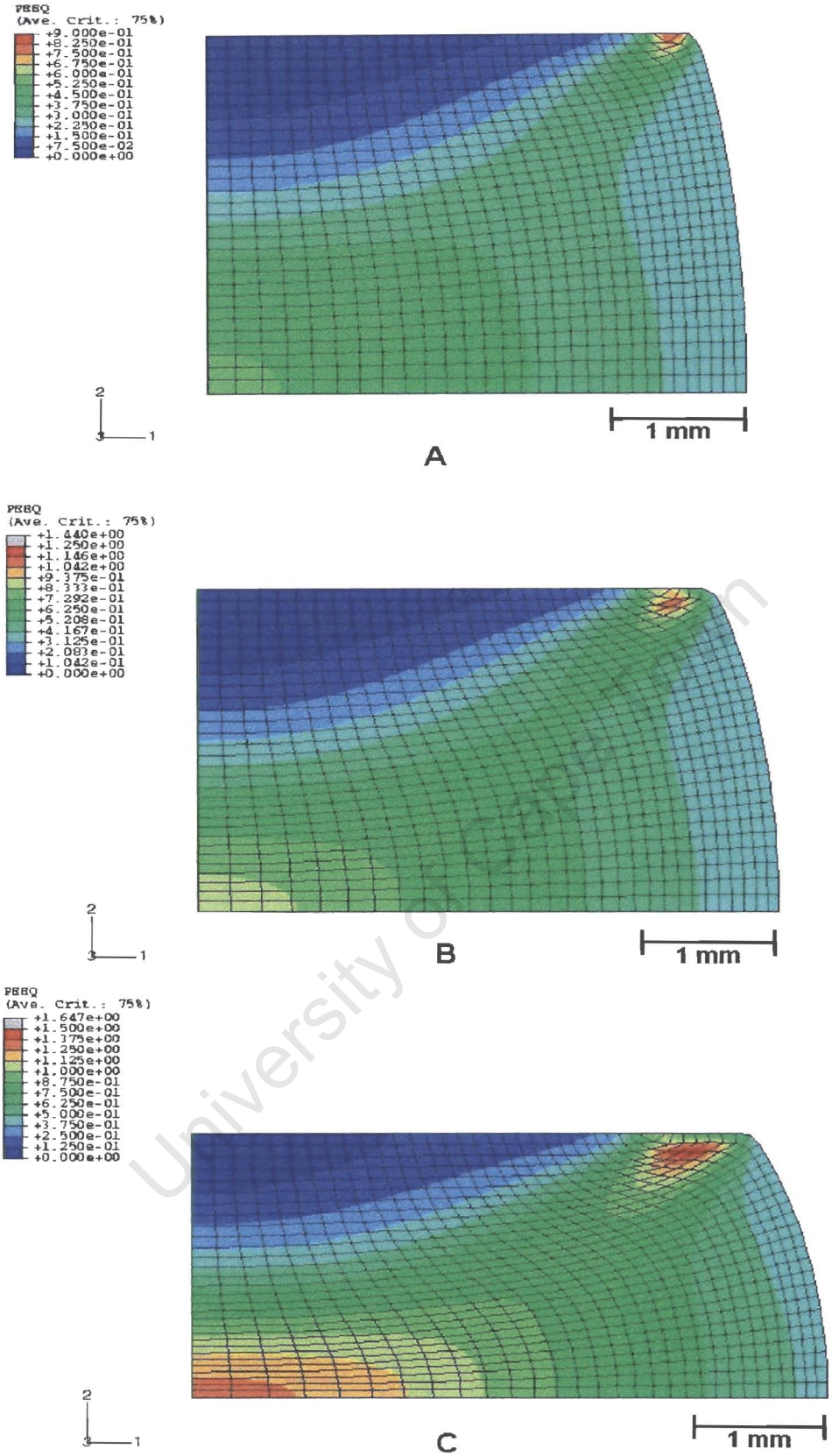

Figure 4.10: **FE schematic of specimens deformed to a nominal strain of (A) 0.3 (B) 0.45 and (C) 0.65. Areas of highest effective strain are located in the centre and at the loading face circumference where roll over occurred.**

4.2 Hardness Results – Z1

Deformation condition Z1 relates to specimens that were deformed at a temperature of 850^0C and a strain rate of 1^{-s}. The decrease in hardness with annealing time for specimens deformed at Z1, to effective strains of 0.52, 0.85 and 1.25, are illustrated in figure 4.11; the annealing temperature was 800^0C. Figure 4.12 shows the results for specimens deformed at Z1 and annealed at a temperature of 900^0C. The error bar in the top corner of the graphs indicates the average scatter in hardness results.

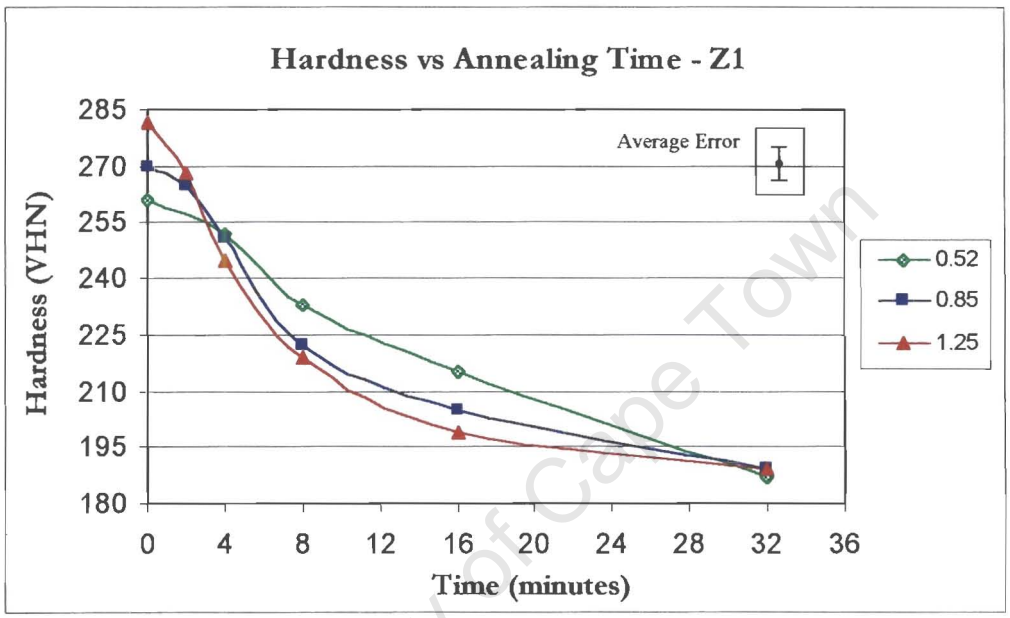

Figure 4.11: The decrease in hardness with annealing time at a temperature of 800^0C.

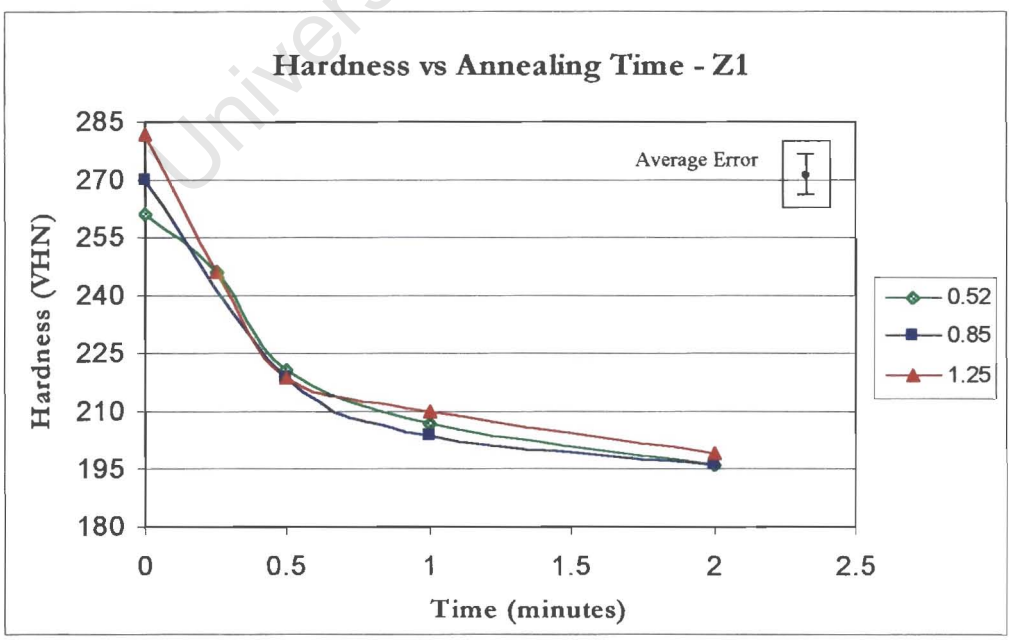

Figure 4.12: The decrease in hardness with annealing time at a temperature of 900^0C.

4.2.1 Strain and Temperature Characteristics

The effect of strain on the hardness versus annealing time relationship is shown in figure 4.11. An increase in strain raises the stored energy and thus accelerates the rate of hardness decrease (softening kinetics) during annealing. It is shown in figure 4.11, that softening kinetics of specimens strained to 1.25 are more rapid in comparison to the two lower strains.

The increase in annealing temperature has a significant effect on softening kinetics. This is clearly illustrated in comparing figures 4.11 and 4.12, for specimens annealed at 800^0C and 900^0C respectively. All specimens in figures 4.11 and 4.12 were deformed at equivalent Z values, Z1 i.e. equal as-deformed hardness. Thus, the comparison of softening kinetics is directly related to the effect of temperature. For specimens annealed at 800^0C, figure 4.11, complete softening is attained between annealing times of 16 and 32 minutes for all strain values. However, complete softening of the equivalent strained specimens, annealed at the higher temperature of 900^0C, is attained between 30 seconds and 1 minute.

4.2.2 Grain Growth Effects

The apparent decrease in softening kinetics, after 30 seconds, of the highest strained specimen (1.25) in figure 4.12 can be explained in terms of grain growth effects (see Chapter 3, section 3.7.1). From figure 4.12 it would appear that the transition point separating regime 1, recrystallization softening, and regime 2, grain growth effects, is attained at approximately 30 second for the specimen strained to 1.25. Micrographs assisted in determining the transition time between the hardness decrease due to softening and the start of grain growth. Figures 4.13 to 4.15 illustrate the microstructural development of specimens strained to 1.25 and annealed at 900^0C. Complete recrystallization is attained prior to 30 seconds, figure 4.14, confirming that anneal data after this time does not represent softening due to recrystallization mechanisms. In comparison, micrographs of the specimen strained to 0.52 suggest that the transition point is in the region of 1 minute. Therefore, the highest strained specimen reaches complete recrystallization prior to the two lower strains. Following the point of transition, regime 2, the hardness decrease is not so dramatic due to the different mechanism governing softening. However, softening in the two lower strains was not complete at 30 seconds and thus kinetics appear to increase in comparison to the highest strained specimen. After the time that all specimens have attained complete softening, and are therefore within regime 2, the kinetics approach equivalent rates and the graphs merge.

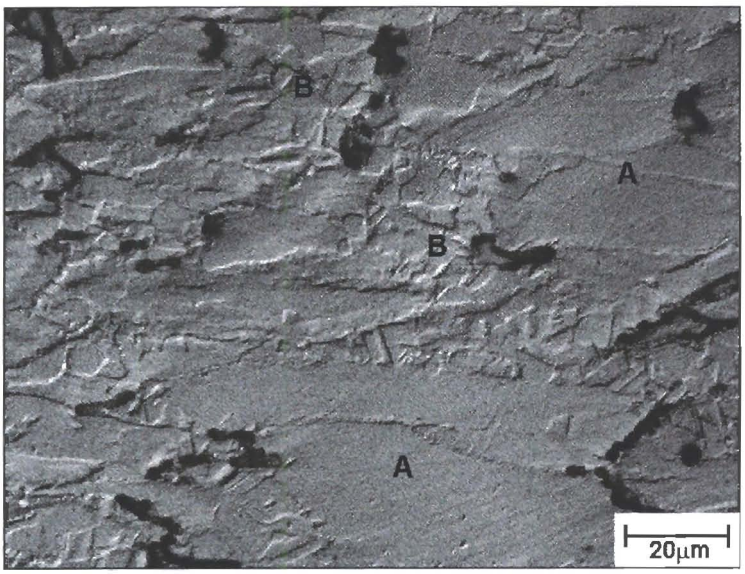

Figure 4.13:
Specimen strained to 1.25 and annealed for 15 seconds at 900^0C.

A: Deformed grains
B: Recrystallized areas

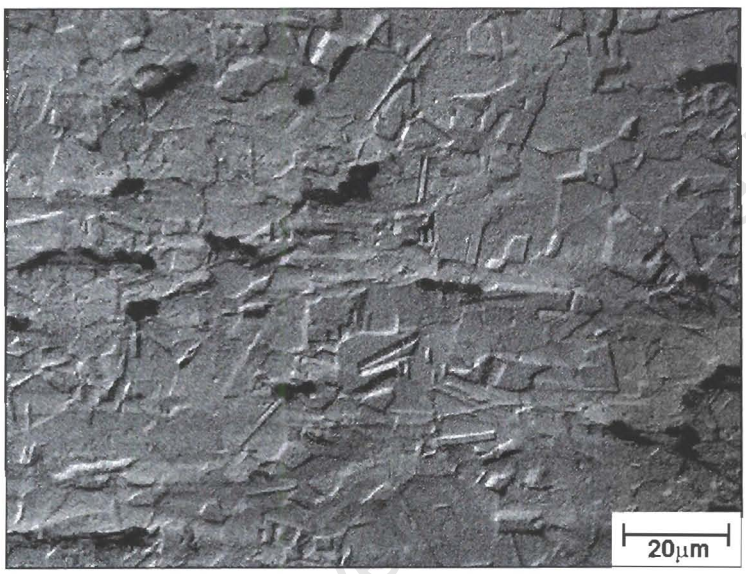

Figure 4.14:
Micrograph confirming 100% recrystallization at a time of 30 seconds. Specimen strained to 1.25 and annealed at 900^0C.

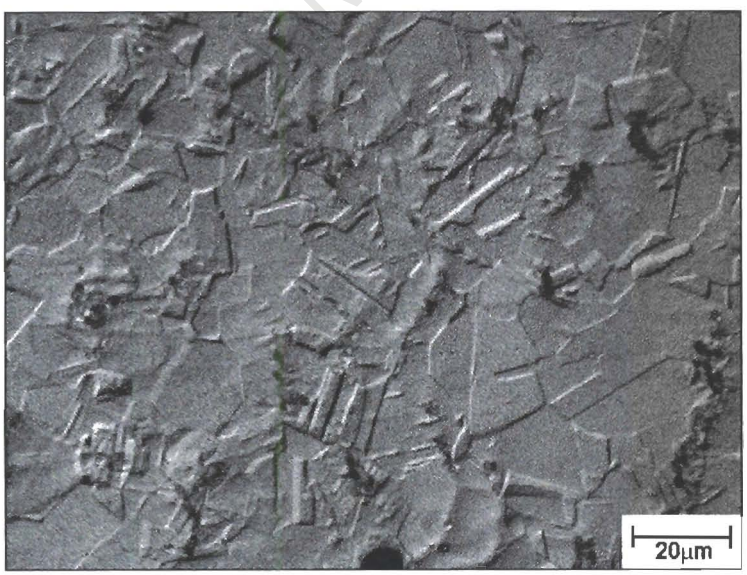

Figure 4.15:
Grain growth following complete recrystallization. Specimen strained to 1.25 and annealed for 2 minutes at 900^0C.

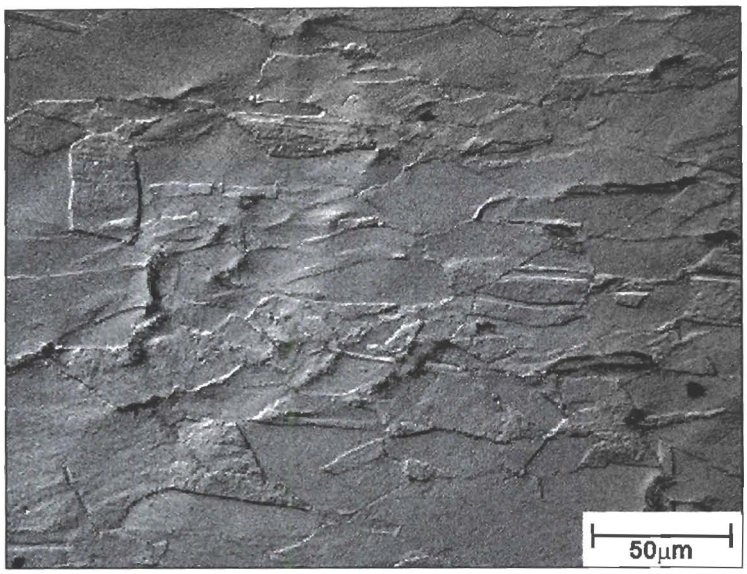

Figure 4.16:
Specimen strained to 0.52 and annealed for 30 seconds at 900^{0}C. Regions of elongated grains suggest that the microstructure is only partially recrystallized.

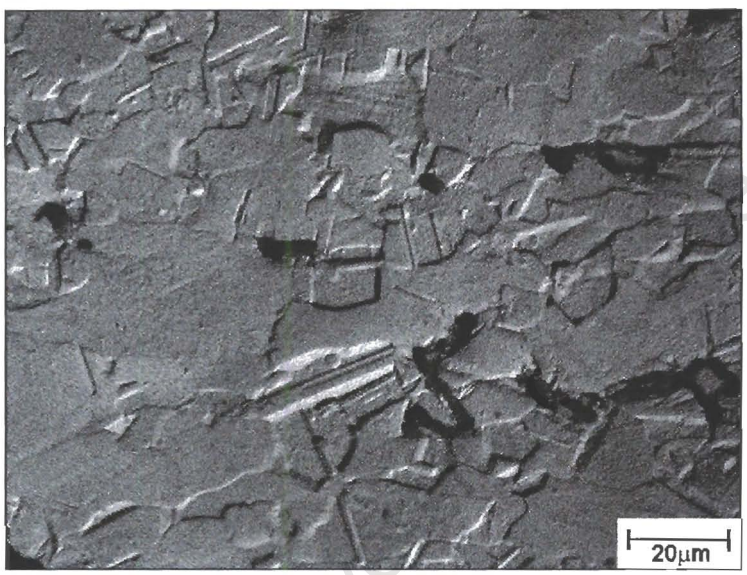

Figure 4.17:
Specimen strained to 0.52 and annealed for 1 minute at 900^{0}C. Approximately 100% recrystallized.

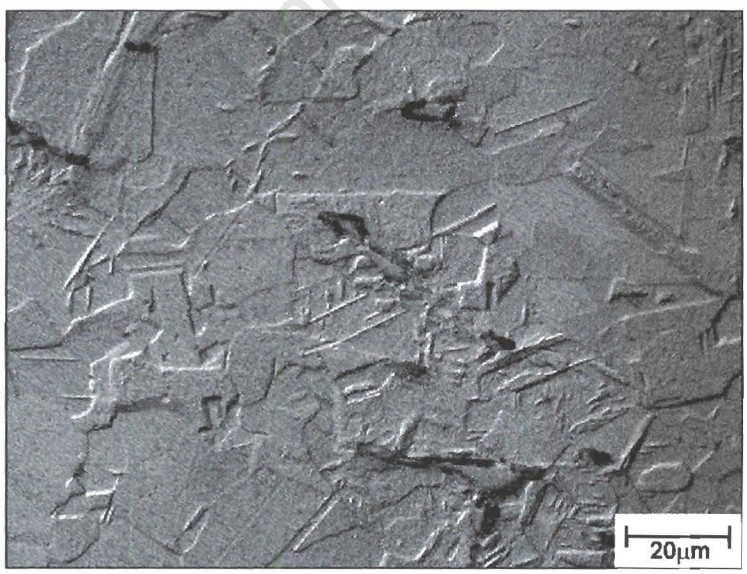

Figure 4.18:
Grain growth, after a time of 2 minutes, for the specimen strained to 0.52 and annealed at 900^{0}C.

4.3 Hardness results – Z2

Deformation of Z2 specimens was performed at a temperature of 950^{0}C and a strain rate of 1^{-s}. The specimen strains, 0.52, 0.85 and 1.25, were the same as those used for Z1 deformed specimens. Figures 4.19 and 4.20 illustrate the relationship between hardness and annealing time for annealing temperatures of 800^{0}C and 900^{0}C respectively.

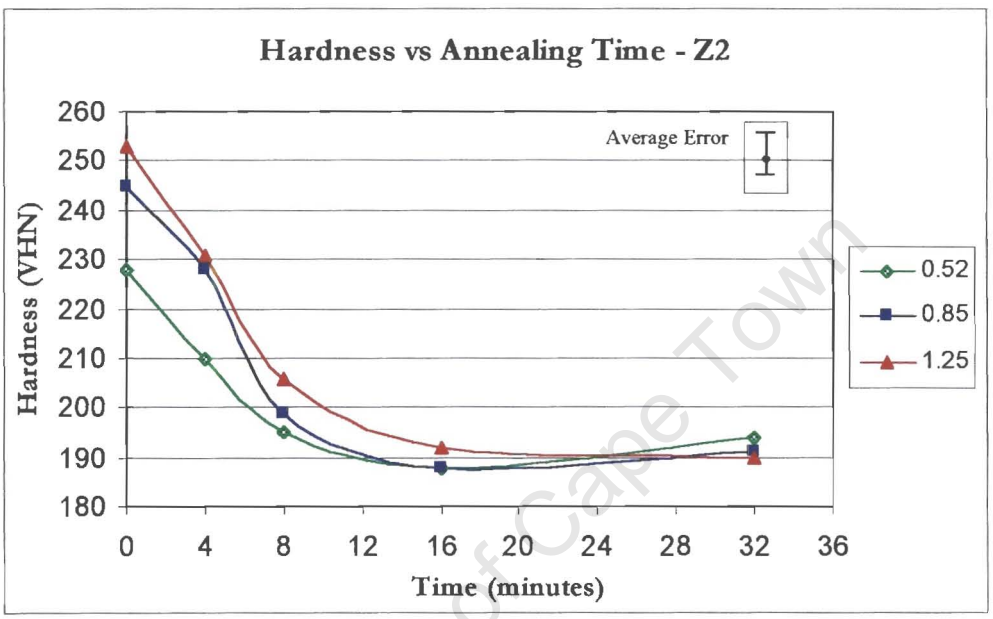

Figure 4.19: The decrease in hardness with annealing time at a temperature of 800^{0}C.

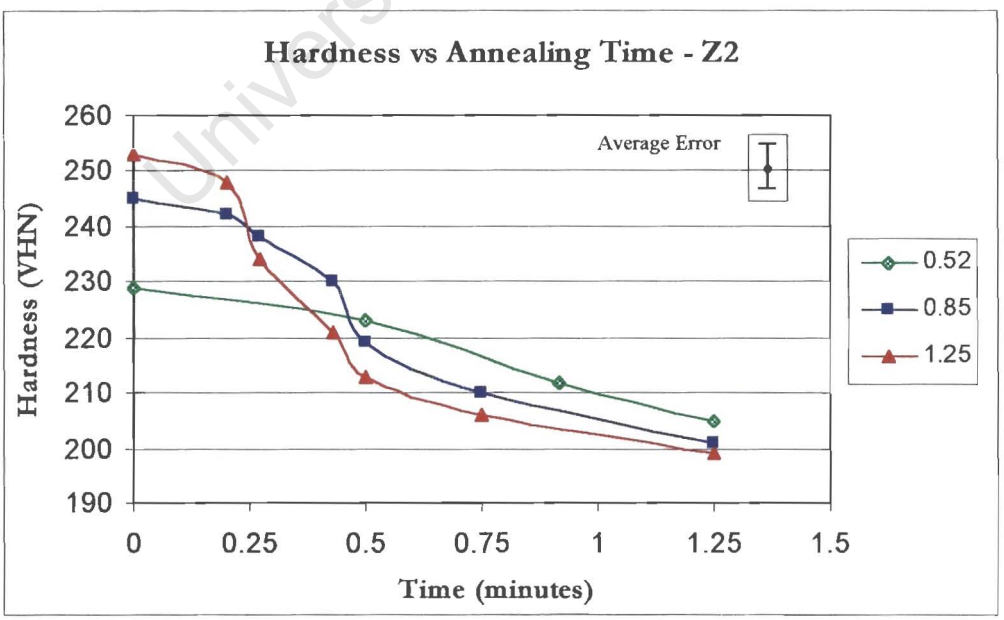

Figure 4.20: The decrease in hardness with annealing time at a temperature of 900^{0}C.

4.3.1 Precipitates

The minor increase in hardness after 16 minutes for specimens strained to 0.52 and 0.85, figure 4.19, was attributed to $M_{23}C_6$ precipitation formation at the grain boundaries. There was evidence of precipitates in the specimen strained to 1.25 and annealed for 32 minutes; however, they did not occur to the extent observed in the two lower strained specimens and thus did not contribute to a measurable hardness increase. The effect of the precipitates was not detrimental to the softening kinetics for all of the annealed specimens, as complete recrystallization had occurred prior to precipitation. This is illustrated in figures 4.21 and 4.22 for specimens strained to 0.52 and annealed for 16 minutes and 32 minutes respectively. Complete recrystallization had occurred within a time of 16 minutes, figure 4.21; however, precipitation is only evident after a time of 32 minutes, figure 4.22. Figure 4.23 is a light microscope image, of the specimen annealed for 16 minutes, illustrating the absence of precipitates.

4.3.2 Selecting Annealing Intervals

The softening kinetics at a temperature of 900^0C are rapid in comparison to the kinetics at 800^0C, as discussed in section 4.2.1. For specimens deformed at Z2 there is a similar relationship between annealing temperature and softening kinetics, as shown in figures 4.19 and 4.20. Selecting a suitable time interval was complicated by the rapid softening kinetics at the higher annealing temperature. It is apparent that the annealing intervals used in figure 4.12 (section 4.2) were longer than required and thus the graphs only capture a large decrease in hardness between annealing times. Furthermore, there are only two data points between the deformed and fully recrystallized microstructure, producing graphs that appear to have similar softening kinetics. Thus annealing intervals for Z2 deformed specimens, annealed at 900^0C, were reduced in an attempt to capture the complete microstructural evolution. The reduced annealing intervals, as shown in figure 4.20, produce a smaller incremental hardness decrease from deformed to the fully recrystallized microstructure. However, differences in annealing time increments as short as 4 seconds were sufficient to induce significant recrystallization. Micrographs of the specimens strained to 0.85 and annealed at 900^0C for various times, figure 4.24 A-C, illustrate the complexity of selecting suitable annealing intervals. The microstructure of the specimen annealed for 16 seconds, figure 4.24 A, indicates that recrystallization has not yet occurred or is

still in the incubation stage. The decrease in hardness at a time of 16 seconds is also negligible (see figure 4.20). However, after annealing for 26 seconds, figure 4.24 B it is clear that recrystallization has occurred in certain areas (approximately 30% recrystallized based on visual identification). An appreciation of the rapid softening kinetics is shown in the micrograph of the specimen annealed for 30 seconds, figure 4.24 C. The microstructure appears to be completely recrystallized after annealing for 30 seconds. Thus, between an annealing time of 26 and 30 seconds the recrystallization kinetics have been extremely rapid. The noticeable decrease in hardness between the two annealing intervals is illustrated in figure 4.20. The specimens strained to 1.25 illustrate a similar response between annealing times of 15 and 30 seconds, see figure 4.25 A-C.

The sensitivity of the softening kinetics at the higher annealing temperature of 900^0C emphasises the accuracy required in measuring annealing times of the specimens. Thus, annealing time was carefully measured from time of placing the specimen into the salt bath to the point of quenching. The time taken for the specimen to heat-up to the annealing temperature, after being placed in the salt bath, was assumed to be negligible. There was approximately a 2 second delay in transferring the specimen from the salt bath to quenching. The temperature of the specimen was assumed to remain constant during the 2 second conversion period.

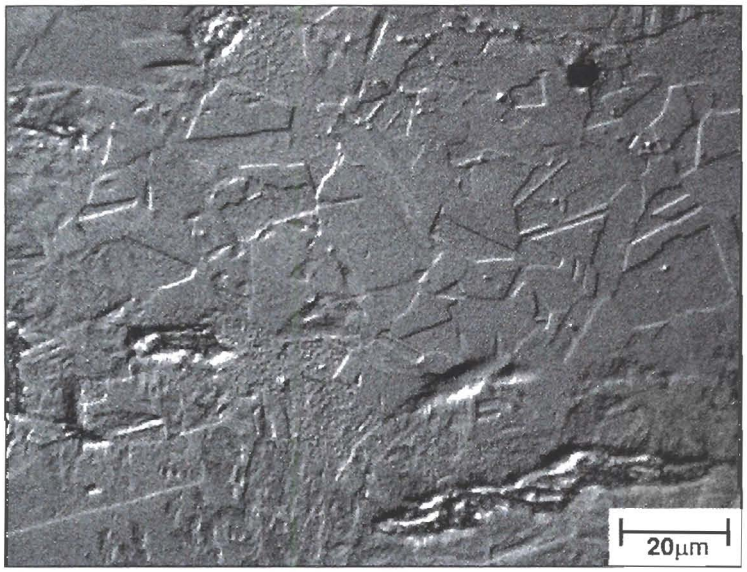

Figure 4.21:
Specimen strained to 0.52 and annealed for 16 minutes at 800^{0}C. Completely recrystallized with no evidence of precipitation.

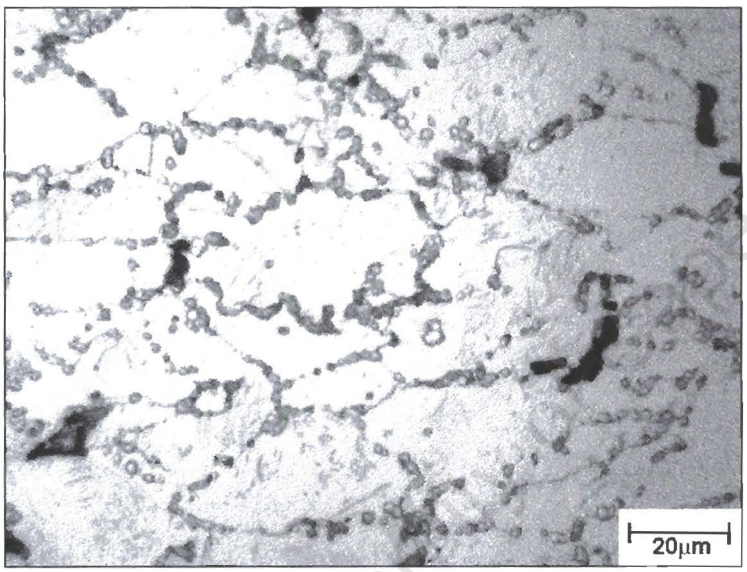

Figure 4.22:
Light microscope image showing regions of precipitation. It should be noted that the precipitates have been etched-out leaving holes at the grain boundaries. Thus, actual precipitates were not as large as they appear in the micrograph. Specimen strained to 0.52 and annealed at 800^{0}C for 32 minutes.

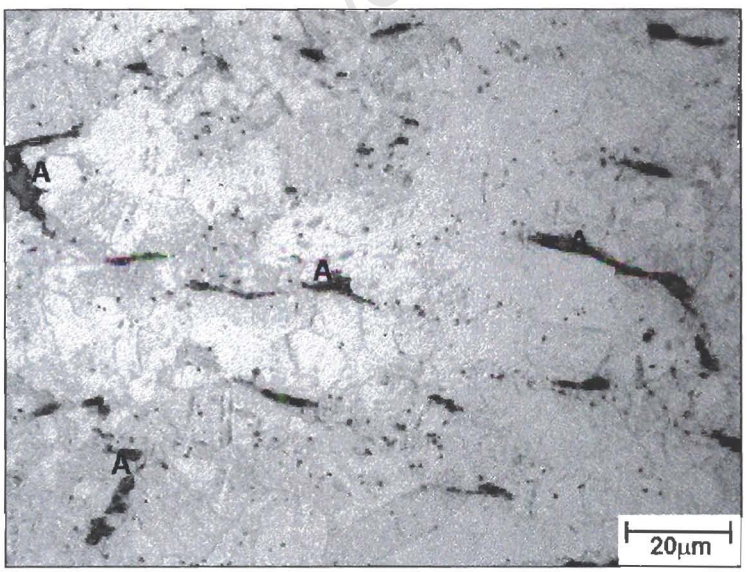

Figure 4.23:
Light microscope image of specimen in figure 4.20. Areas marked A are regions of ferrite stringers.

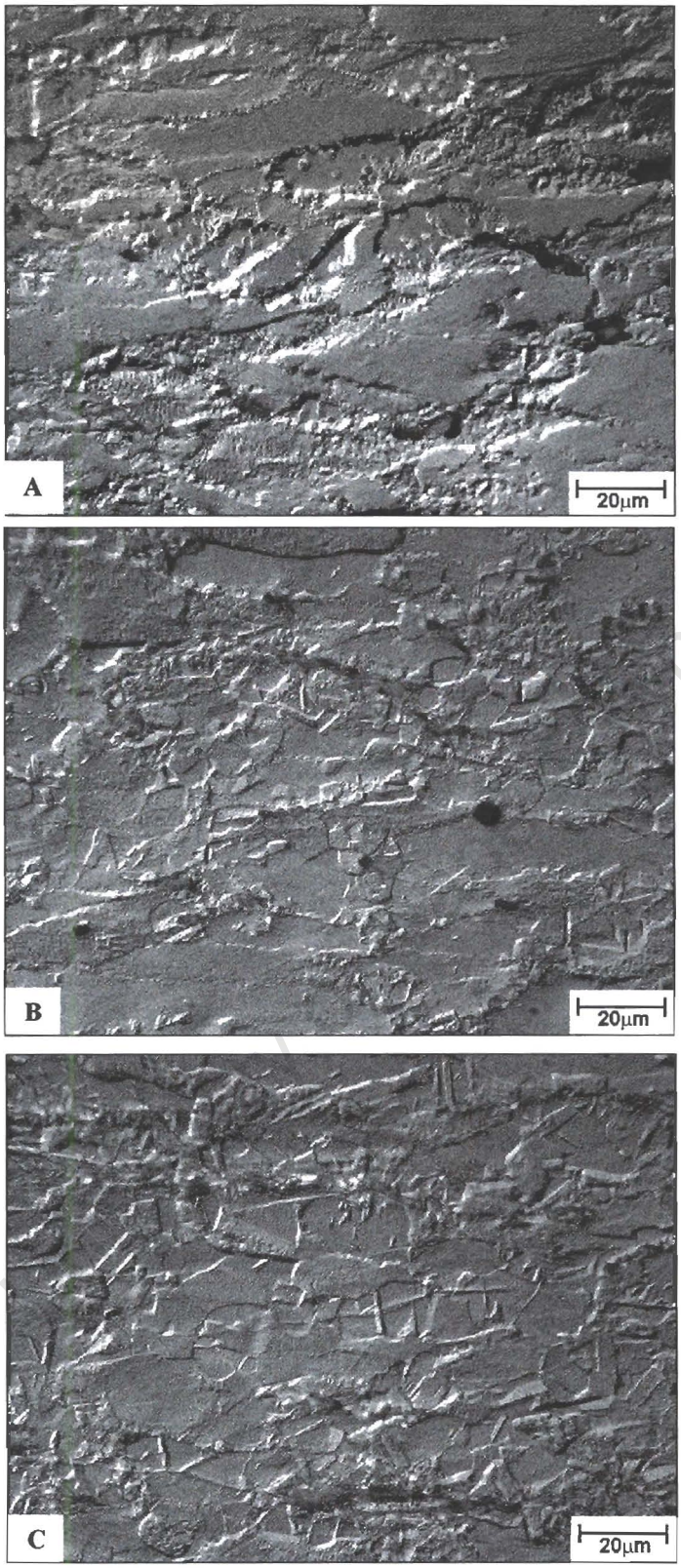

Figure 4.24 A-C: **Progress of recrystallization with time for specimens deformed at Z2, strain of 0.85, and annealed at 900^0C (A) still deformed after 16 seconds (B) approximately 30% recrystallized after 26 seconds (C) fully recrystallized after 30 seconds.**

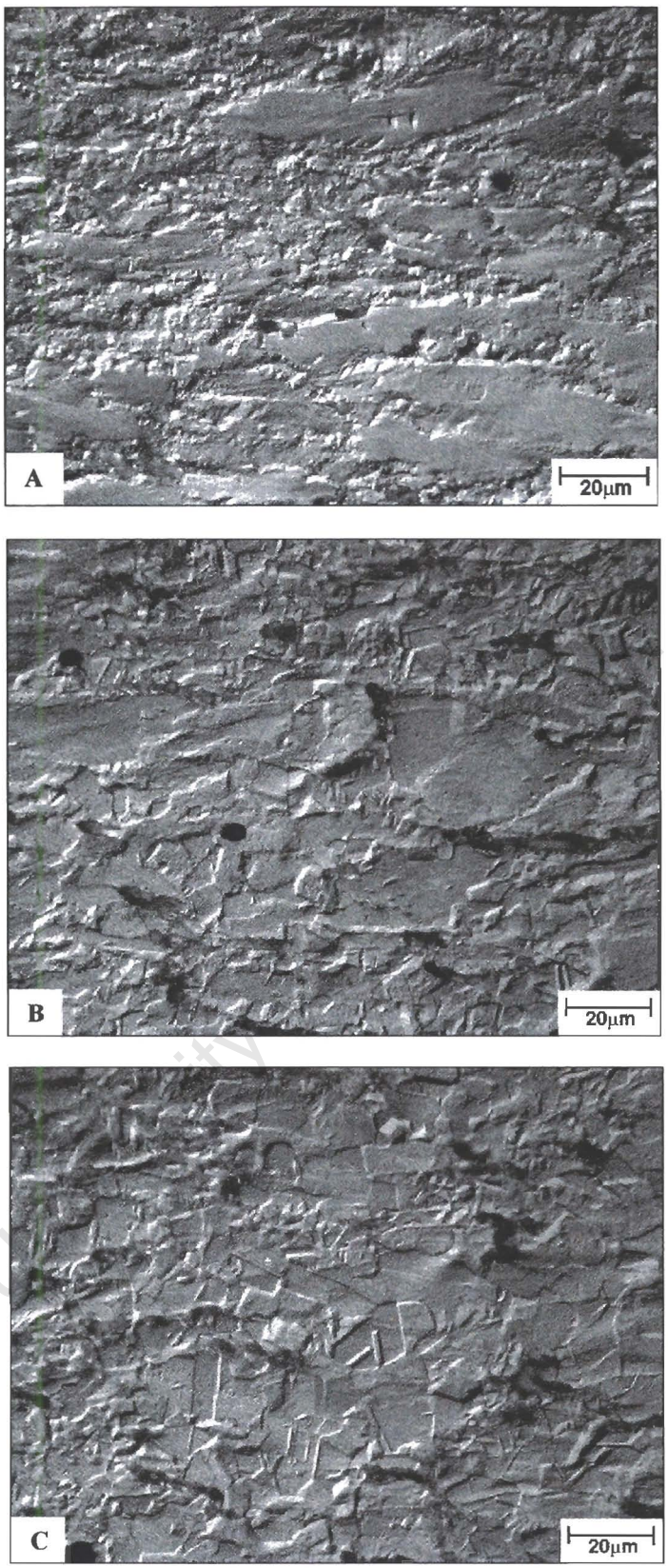

Figure 4.25 A-C: **Progress of recrystallization with time for specimens deformed at Z2, strain of 1.25, and annealed at 900^{0}C (A) microstructure appears deformed after annealing for 16 seconds (B) approximately 80% recrystallized after 26 seconds (C) fully recrystallized after 30 seconds.**

4.4 Recrystallized Fraction Analysis

4.4.1 Introduction

The Avrami constant is determined from graphs of volume fraction material recrystallized versus annealing time. The fraction of material recrystallized can be calculated from the hardness versus annealing time data, presented in figures 4.11 – 4.12 for Z1 and figures 4.19 – 4.20 for Z2, using equation 3.5 (see Chapter 2, section 3.7.1). However, it needs to be determined that hardness restoration is suitably correlated to fraction recrystallized. EBSD was used to quantify the relationship between hardness and recrystallization.

4.4.2 Evaluating Fraction Recrystallized using EBSD

EBSD analysis was performed on specimens deformed at Z1, strained to 0.52, 0.85 and 1.25, and annealed at 800^0C to establish the relationship between hardness restoration and recrystallization. The EBSD maps, figures 4.26 to 4.31, represent the microstructural development of specimens strained to 0.85 and annealed at 800^0C for the specified times. The red areas in figure 4.27 and 4.29 represent regions that the VMAP software has designated to be recrystallized based on the absolute reconstruction method. The HAGB have been defined as having a 15^0 misorientation and are displayed in black, whereas subgrain boundaries have been defined by a 2^0 misorientation and are displayed in blue. The grains are coloured in shades of grey and not Euler colours to enable the blue subgrains to be easily distinguishable.

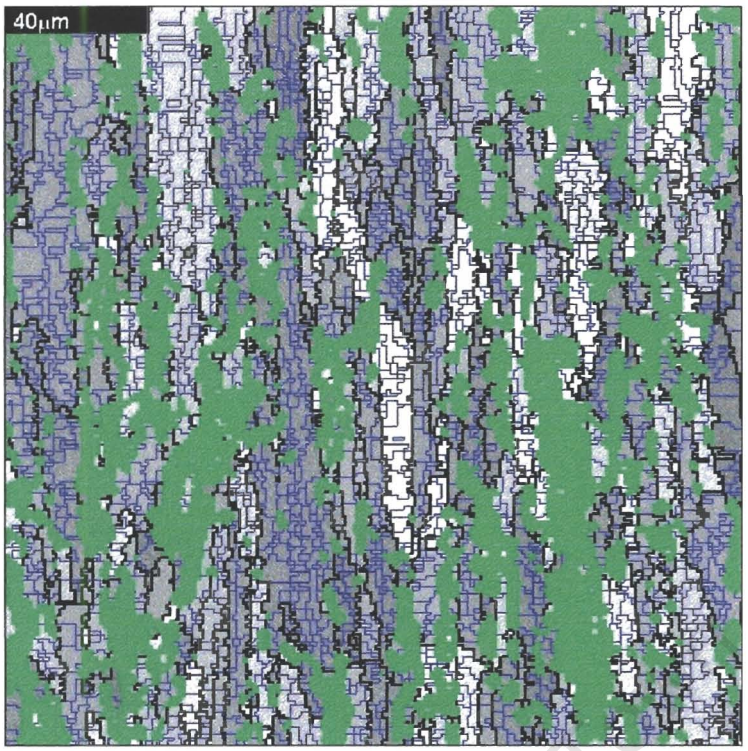

Figure 4.26: **Specimen strained to 0.85 and annealed for 2 minutes at 800^{0}C. The figure below shows the regions that VMAP software has designated recrystallized.**

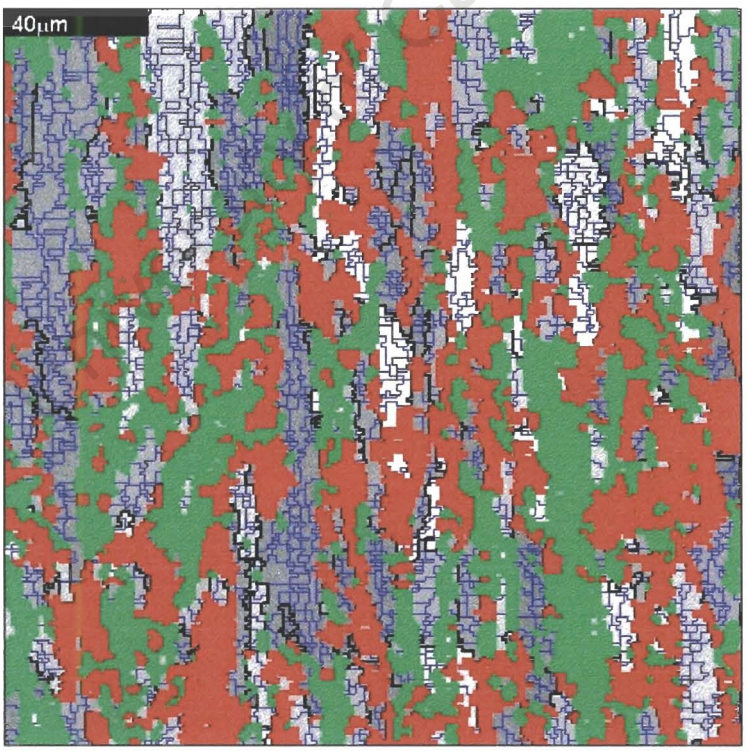

Figure 4.27: **Calculating recrystallized fraction for specimen strained to 0.85 and annealed at 800^{0}C for 2minutes. 25 % recrystallized (green and red colours represent non-indexed and recrystallized areas respectively).**

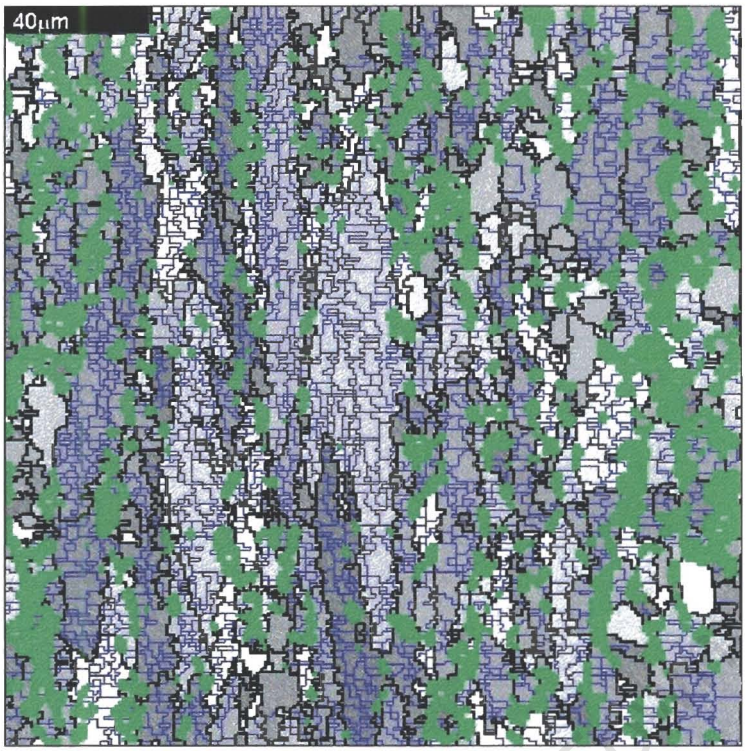

Figure 4.28: **Specimen strained to 0.85 annealed for 4 minutes at 800^{0}C; see figure below for recrystallized fraction.**

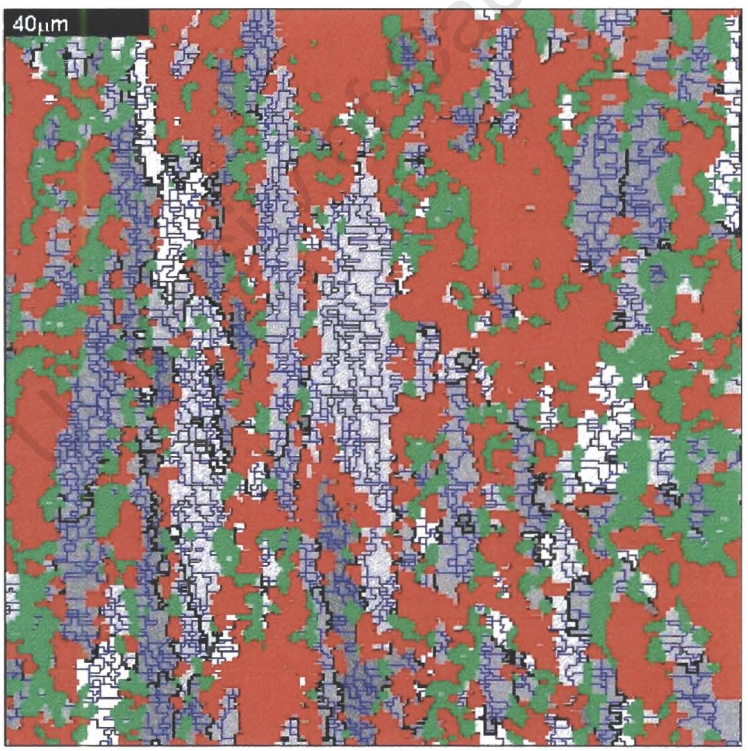

Figure 4.29: **Red areas represent regions that VMAP software has designated to be recrystallized for specimen strained to 0.85 annealed for 4 minutes at 800^{0}C, 35% recrystallized. Green areas are non-indexed points.**

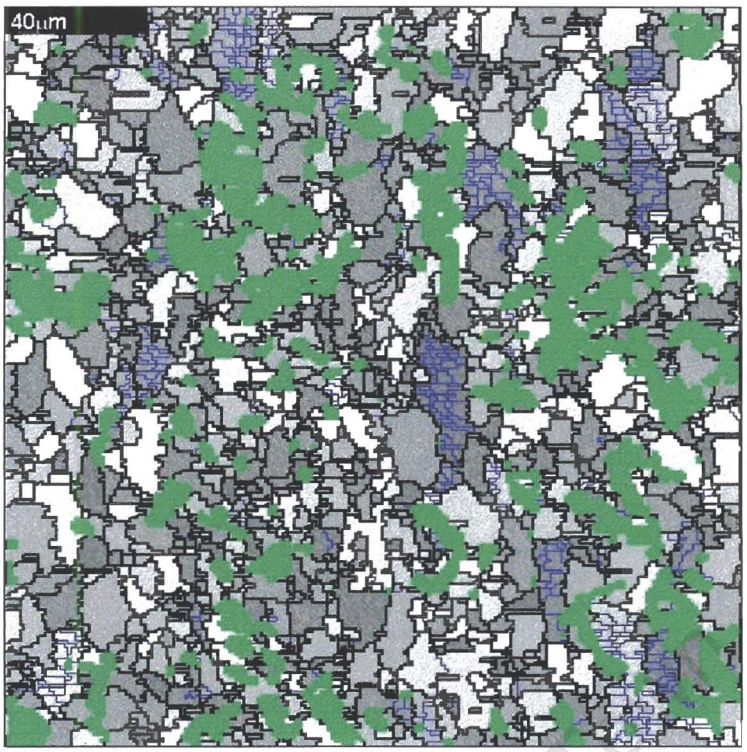

Figure 4.30: **Specimen strained to 0.85 annealed for 8 minutes at 800^{0}C; 76% recrystallized. Note that the corresponding map of red recrystallized areas is not shown in this instance as the map is coloured red apart from the grains containing the substructure (blue boundaries).**

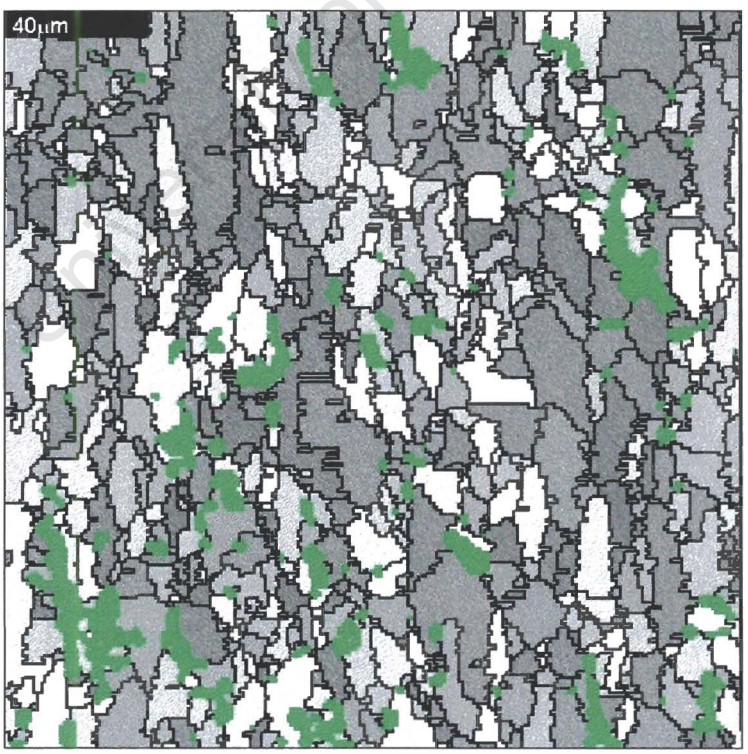

Figure 4.31: **Specimen strained to 0.85 annealed for 16 minutes at 800^{0}C, 100% recrystallized.**

4.4.3 Restoration of Hardness and Recrystallized Relationship

The relationship between restoration of hardness and fraction statically recrystallized is shown in figures 4.32 to 4.34 for the specimens deformed at Z1 and annealed at 800^0C. For all of the experimental strains shown in figures 4.32 to 4.34 the recrystallized fraction, calculated using EBSD, is higher than the hardness restoration fraction. The most noticeable difference between recrystallized and hardness fraction is during the early stages of annealing for all of the strain values. However, after the initial annealing stages (at approximately 30% hardness restoration) the graphs tend to converge to similar values. The graph of the specimens strained to 0.52, figure 4.32, shows a near perfect relationship between static recrystallization and hardness restoration. For the two higher strains, the difference, after 30% hardness restoration, is in the region of 10%. Figures 4.32 to 4.34 give evidence to suggest that the restoration of hardness is a good approximation of the recrystallized fraction and any deviations are within experimental error.

Barraclough and Sellars[36] performed a similar study on the relationship between recrystallization and hardness restoration. However, their results showed the opposite relationship to the results found in this study; restoration of hardness was approximately 20% higher than fraction recrystallized. The deviation was concluded to be a result of heterogeneity of deformation between recrystallized and unrecrystallized regions during hardness tests. The effect of recovery on static recrystallization had a minor effect on the non-linear relationship. An important consideration is that their results were specifically for torsion and it is expected that torsion tests will produce greater deformation heterogeneity than uni-axial testing. They concluded that hardness restoration enables estimates of deformation conditions on $t_{0.5}$ when the allowance is made for the non-linearity i.e. when restoration of hardness equals 75% the fraction recrystallized will be approximately 50%. It should also be noted that a point counting technique was used in their study to identify fraction recrystallized.

The correlation between hardness restoration and fraction recrystallized, in this study, is considerably better than the results of Barraclough and Sellars[36]. It is not proposed that EBSD provides an improved method of determining fraction recrystallized than a point counting technique. More importantly, a comparison of the results suggest that

the deformation technique needs to be considered when deriving a relationship between hardness restoration and fraction recrystallized; heterogeneity of deformation does exist to different extents for a given deformation mode. For the purposes of this study hardness restoration and fraction recrystallized are well correlated and are thus deemed equivalent. EBSD analysis is time consuming and therefore, due to the good relationship between recrystallized fraction and hardness restoration, it was not necessary to perform EBSD for every deformation and annealing condition. However, it should be borne in mind that the relationship would not be acceptable if dynamic or metadynamic recrystallization phenomenon impede predictive static recrystallization kinetics.

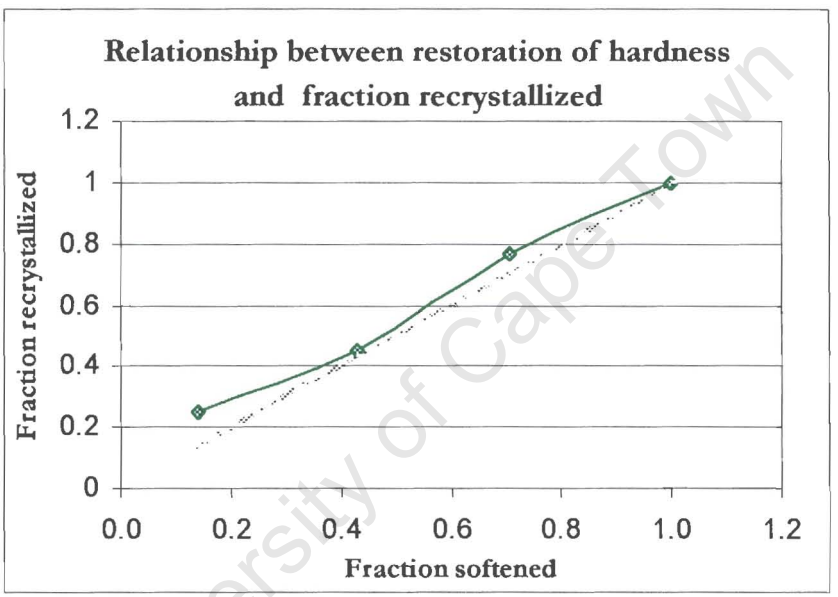

Figure 4.32: **Relationship between restoration of hardness and fraction statically recrystallized for specimens strained to 0.52 and annealed at 800^{0}C.**

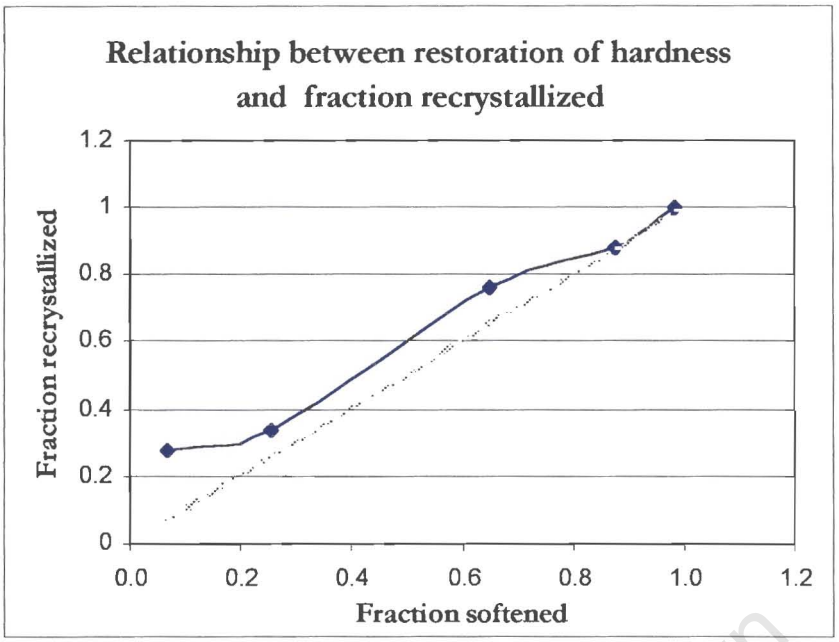

Figure 4.33: **Relationship for specimens strained to 0.85 and annealed at 800^{0}C.**

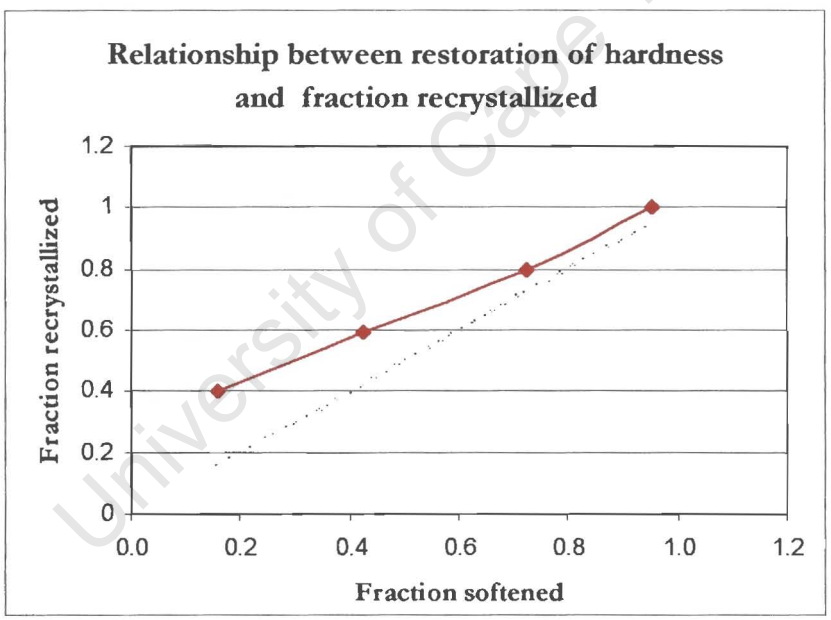

Figure 4.34: **Relationship for specimens strained to 1.25 and annealed at 800^{0}C.**

4.4.4 Softening Kinetics

Based on results from the previous section the characteristic sigmoidal graph of volume fraction material softened, X_s, with respect to annealing time can be derived from equation 3.5 (see section 3.7.1), using hardness restoration data. The hardness value corresponding to complete recrystallization, H_f, was determined using the extrapolation method presented in section 3.7.2. Table 4.2 presents the H_f results obtained from hardness versus annealing time graphs.

Deformation Condition	Strain	Annealing Temperature	Complete softening value, H_f (VHN)
Z1	0.52	800°C	197
Z1	0.85	800°C	197
Z1	1.25	800°C	196
Z1	0.52	900°C	189
Z1	0.85	900°C	191
Z1	1.25	900°C	196
Z2	0.52	800°C	206
Z2	0.85	800°C	203
Z2	1.25	800°C	211
Z2	0.52	900°C	206
Z2	0.85	900°C	203
Z2	1.25	900°C	208

Table 4.2: Results of final value of hardness before grain growth effects, H_f, for all experimental conditions.

The sigmoidal graphs of volume fractional recrystallized versus annealing time are shown in figures 4.35 to 4.38 for all deformation and annealing conditions used in this study. Also shown in figures 4.35 to 4.38 are the corresponding straight-line graphs, plotted according to the Avrami equation, used to determine the Avrami constant for the particular deformation and annealing condition. Although it has been suggested in the previous section that fraction recrystallized and fraction softened are well correlated for experiments in this study, it was decided that the term "fractional softening" would continue to be used, as opposed to fraction recrystallized, when referring to results obtained from hardness tests. This was done in order to avoid any confusion that may arise if further comparisons where necessary for different deformation conditions.

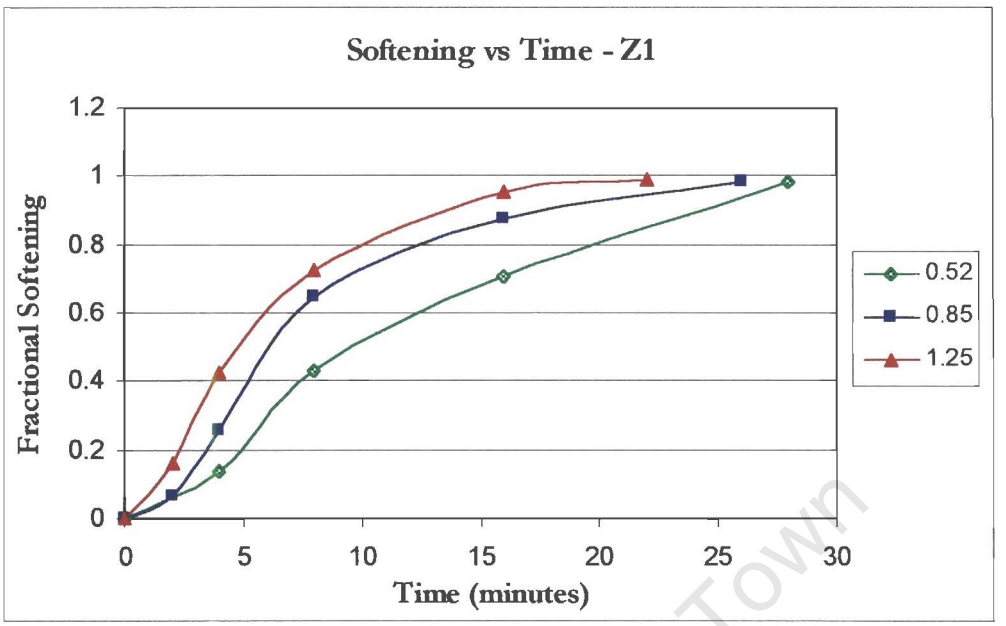

Figure 4.35 A: Effect of strain on the softening curves for specimens annealed at 800^{0}C.

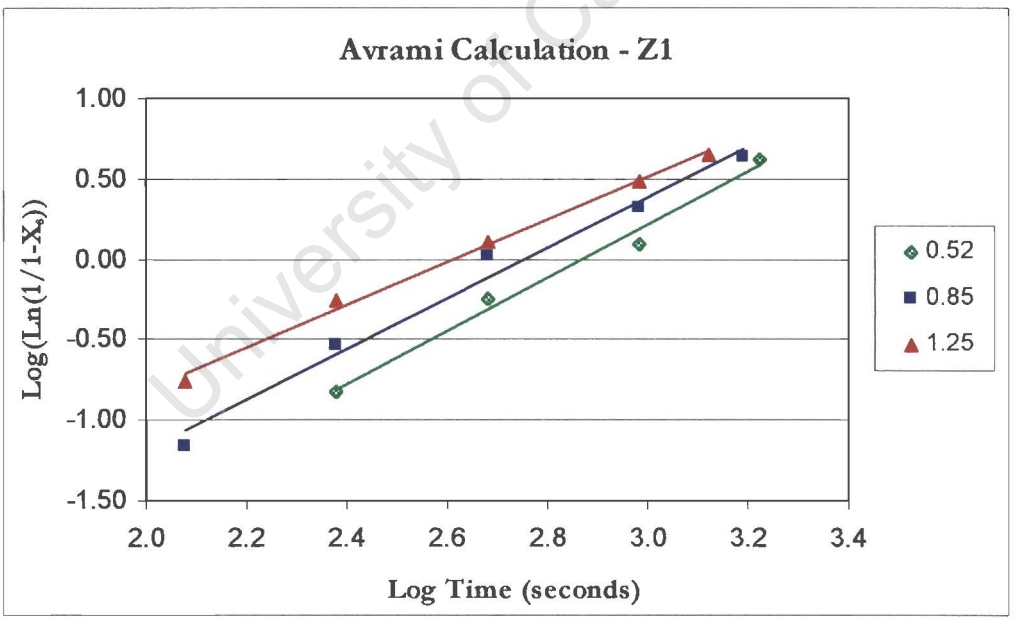

Figure 4.35 B: Softening data, for specimens annealed at 800^{0}C, plotted according to the Avrami equation. Gradient of straight lines determines Avrami constant.

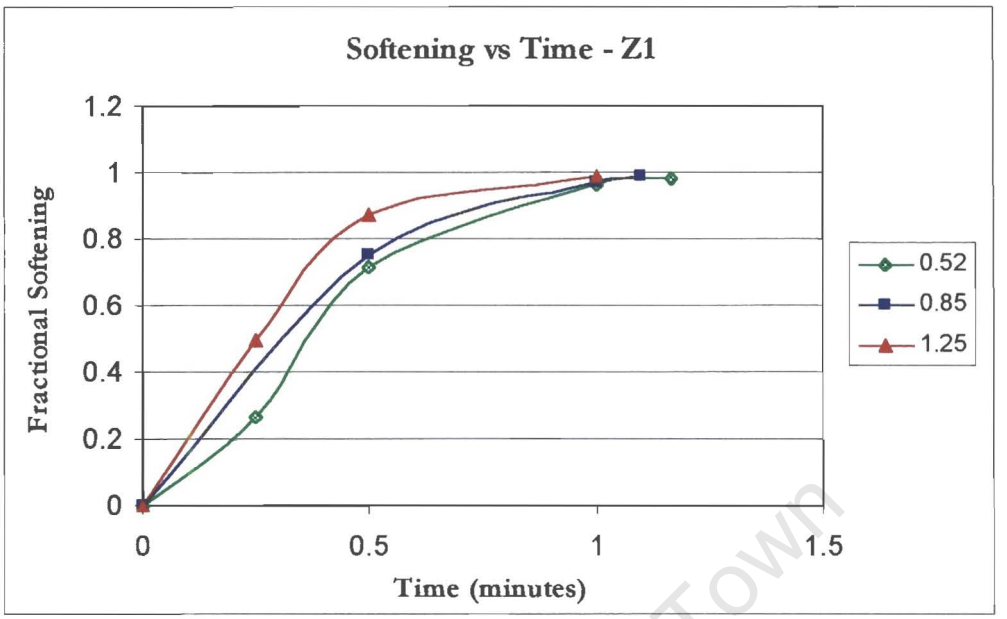

Figure 4.36 A: Effect of strain on the softening curves for specimens annealed at 900^{0}C.

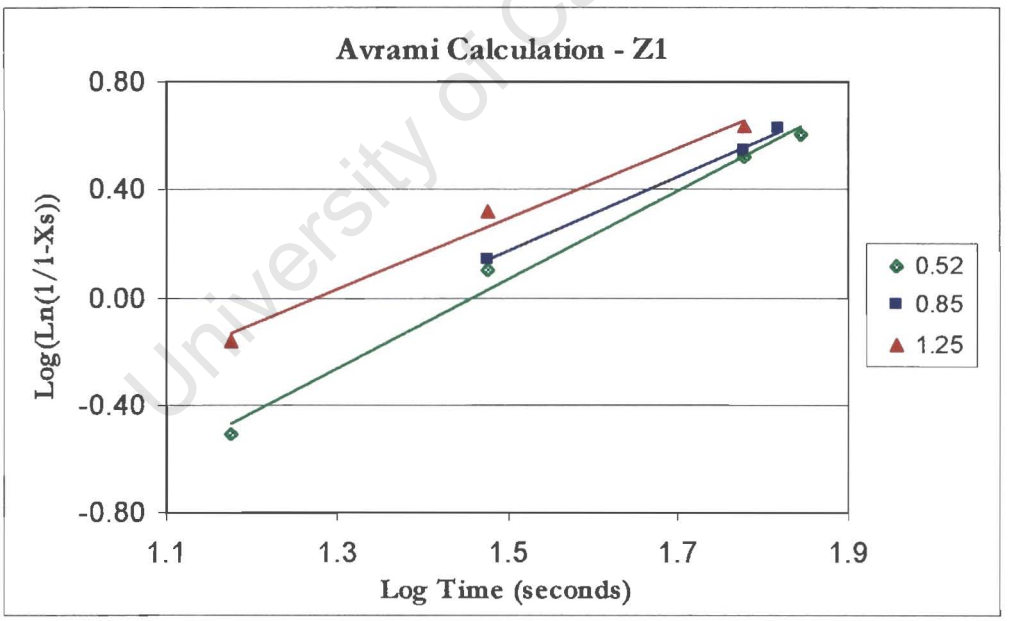

Figure 4.36 B: Softening data, obtained from figure 4.36 A, plotted according to the Avrami equation.

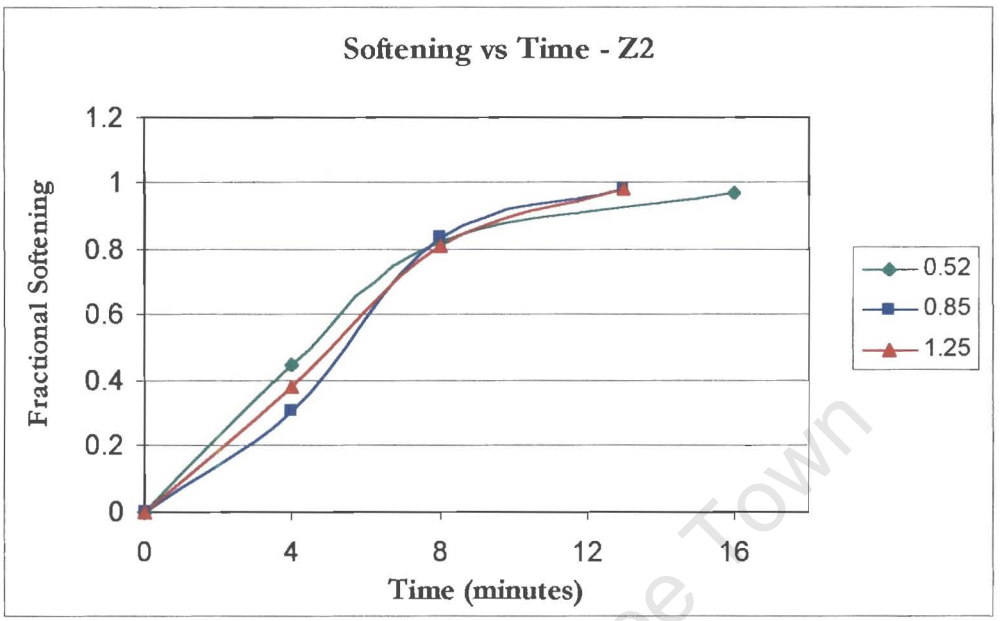

Figure 4.37 A: Softening kinetics for specimens annealed at 800^{0}C.

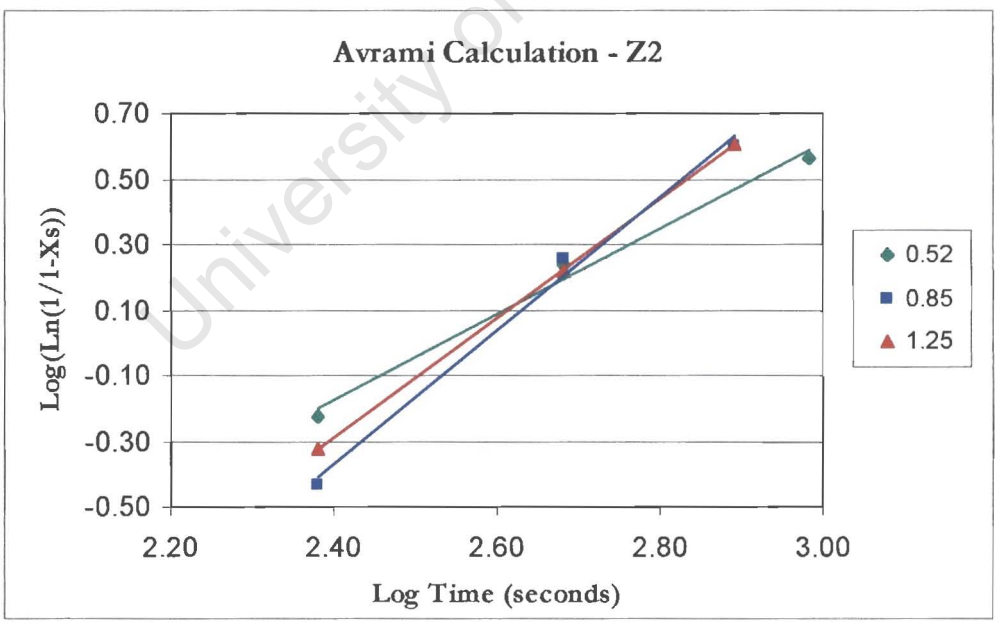

Figure 4.37 B: Data from figure 4.37 A, plotted according to the Avrami equation.

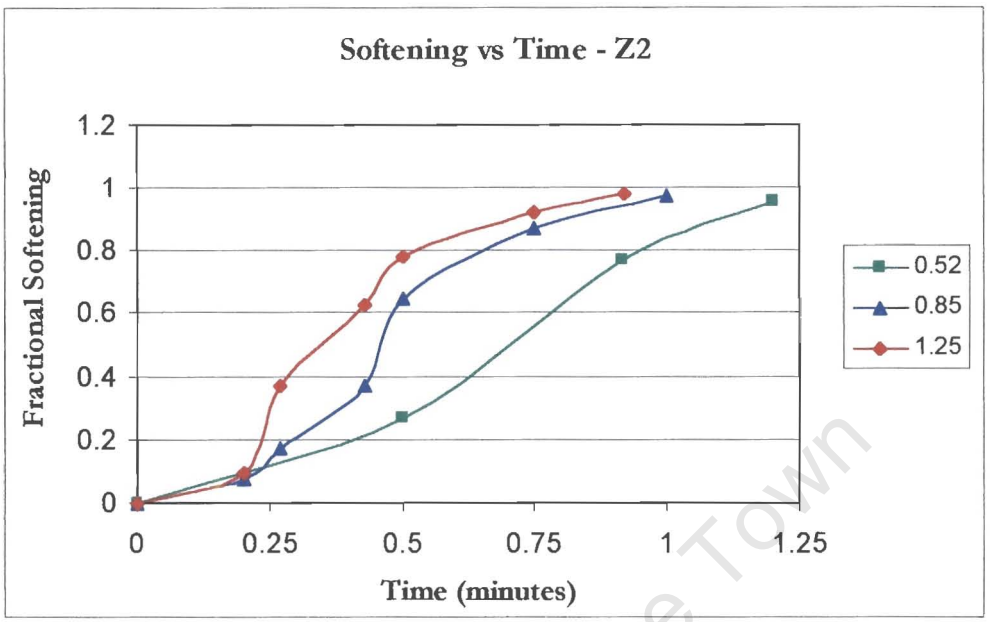

Figure 4.38 A: Softening kinetics for specimens annealed at 900°C.

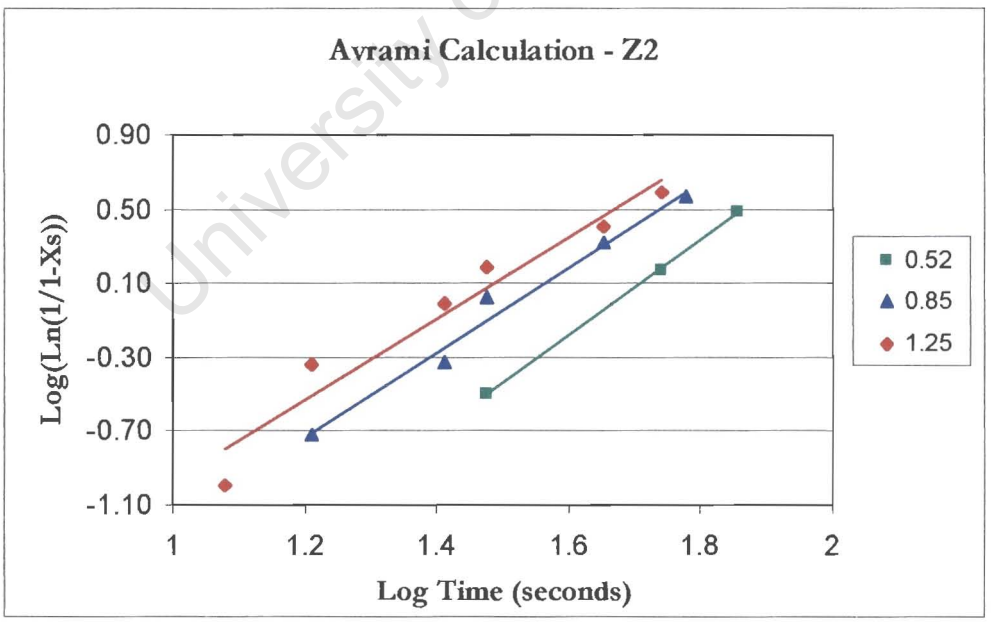

Figure 4.38 B: Data from figure 4.38 A, plotted according to the Avrami equation.

4.4.5 The Avrami Constant

The gradients of the straight-line graphs, figures 4.35 to 4.38, are used to derive the Avrami constant. The results of the experimentally determined constant are presented in Table 4.3a, for specimens deformed at Z1, and Table 4.3b, for Z2 deformed specimens.

Annealing Temperature (^{0}C)	*Strain*	*Avrami Constant, n*
800^{0}C	0.52	1.7
800^{0}C	0.85	1.6
800^{0}C	1.25	1.3
900^{0}C	0.52	1.7
900^{0}C	0.85	1.4
900^{0}C	1.25	1.3

Table 4.3a **Avrami constants for specimens deformed at Z1.**

Annealing Temperature (^{0}C)	*Strain*	*Avrami Constant, n*
800^{0}C	0.52	1.3
800^{0}C	0.85	2
800^{0}C	1.25	1.8
900^{0}C	0.52	2.4
900^{0}C	0.85	2.3
900^{0}C	1.25	2.2

Table 4.3b **Avrami constants for specimens deformed at Z2.**

The n values calculated in this study are in good agreement with those found by previous researchers[36,37,38,47,48,49,50]. An average of the entire range of n values determined in this study was 1.7. The n values presented in Table 4.3b, for specimens deformed at Z2, are generally higher than the n values for specimens deformed at Z1, table 4.3a. In this case the increase in n value is associated with a general decrease in time to recrystallization completion. This is unexpected as the stored energy in the Z2 specimens, deformed at 950^{0}C, is lower than the specimens deformed at 850^{0}C, Z1.

A comparison of figures 4.35a and 4.37a for specimens deformed at Z1 and Z2 respectively, but annealed at the same temperature of 800^0C, illustrates the effect of strain on the softening kinetics. Figure 4.35a effectively illustrates the increased softening kinetics for specimens deformed to higher strain values. However, in figure 4.37a there appears to be no relationship between the strain and the rate of softening. The lowest strained specimen, 0.52, has the highest rate of softening up to 80% volume fraction softened at a time of 8 minutes. The softening rate decreases rapidly between 80 and 100% volume fraction softened (complete softening is attained at a time of 16 minutes). However, the two higher strained specimens, with slower initial softening kinetics, achieve complete softening at a time of 13 minutes. A likely explanation for the behaviour of the specimens deformed at Z2 is the occurrence of recovery, dynamic recrystallization or metadynamic recrystallization processes.

It was also expected that the time to 50% recrystallization, $t_{0.5}$, would be affected by the occurrence of dynamic or metadynamic recrystallization and the results are thus presented in the following section.

4.5 Quantifying $t_{0.5}$

4.5.1 Introduction

The graphs of volume fraction material softened with respect to annealing time are used to calculate $t_{0.5}$ (see figures 4.35a to 4.38a). A trendline is fitted to each of the curves and the equation defining the trendline is then solved for y = 0.5 i.e. the time that 50% of the material had softened. Figure 4.39 illustrates the method that was used to identify $t_{0.5}$ for each deformation condition and annealing temperature.

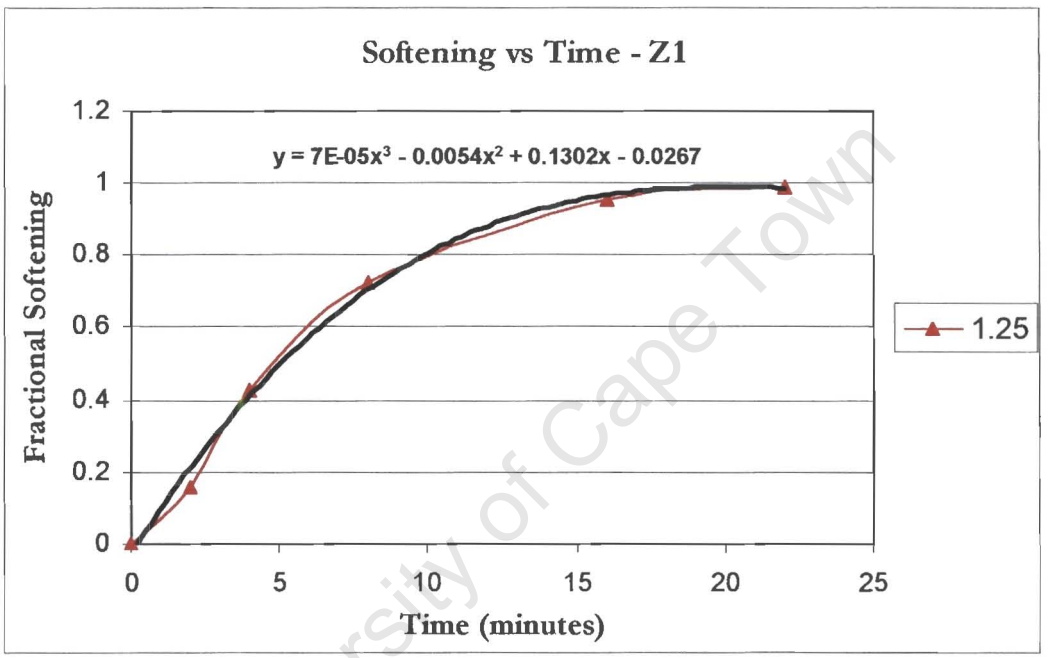

Figure 4.39: A trendline was fitted to each of the curves to identify $t_{0.5}$. The equation is then solved for y = 0.5.

4.5.2 Effect of Deformation Conditions on $t_{0.5}$

Figures 4.40 and 4.41 illustrate the relationship between the deformation conditions and $t_{0.5}$. Specimens deformed at Z1 and Z2, annealed at 800^{0}C, are shown in figure 4.40. The graph for specimens deformed at Z1 shows that the lowest strained specimen, 0.52, has a $t_{0.5}$ value of 625 seconds, compared to 295 seconds for the highest strained specimen. In terms of the stored energy and rate of softening kinetics, this relationship would be expected. The deviation from the strain and $t_{0.5}$ relationship is evident from the graph, in figure 4.40, for specimens deformed at Z2. The lowest strained specimen has a $t_{0.5}$ value of 264 seconds, compared to 306 for the highest strained specimen. Furthermore, the Z2 graph should have slower $t_{0.5}$ values

compared to the Z1 graph; it is clear from figure 4.40 that in this instance the static recrystallization kinetics have been affected by additional annealing phenomena.

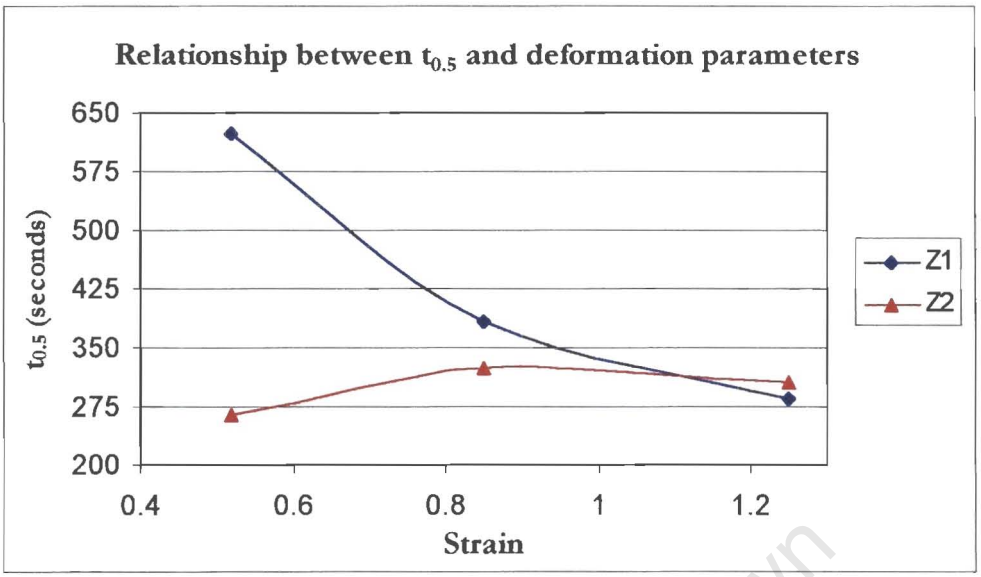

Figure 4.40 **Relationship between $t_{0.5}$ and strain for specimens deformed at Z1 and Z2 and annealed at 800^{0}C.**

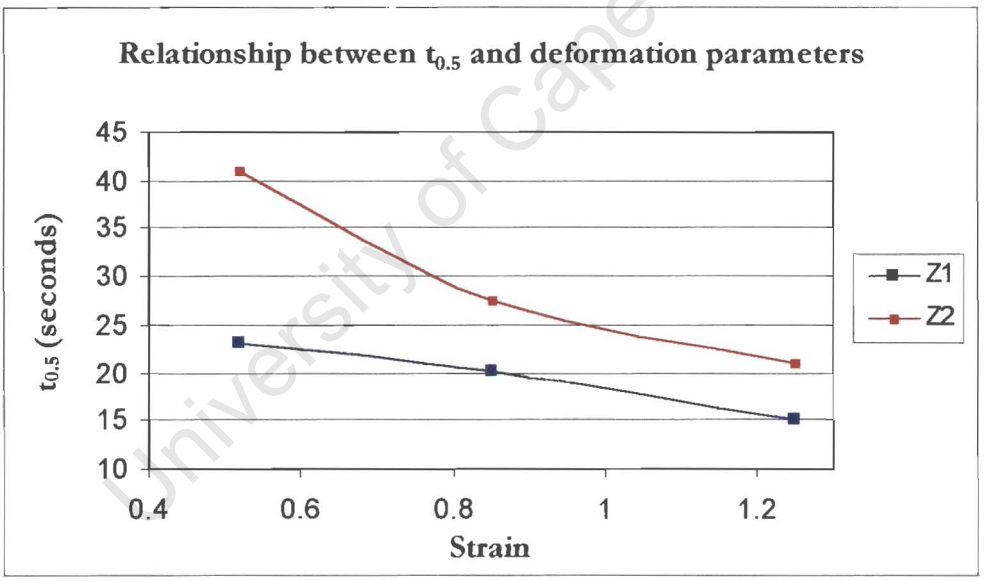

Figure 4.41: **Relationship between $t_{0.5}$ and strain for specimens deformed at Z1 and Z2 and annealed at 900^{0}C.**

4.5.3 Z2 relationship at 800^{0}C

A possible explanation for the behaviour of Z2 deformed specimens, annealed at 800^{0}C, is that deformation occurred in the steady state regime and specimens would thus possess similar stored energy characteristics. Therefore, during the annealing treatment the driving force for recrystallization would be equal, regardless of the

strain value. It is clear from figure 4.40 that there is not a significant difference in the $t_{0.5}$ value for an increase in strain. Previous researchers[36,37] have found a similar relationship between $t_{0.5}$ value and strain when deformation occurred within the steady state regime.

It has already been mentioned that the Gleeble was unable to provide accurate stress versus strain data for the deformation experiments and this was undoubtedly a shortcoming of this particular Gleeble apparatus. From the stress-strain curve it would be clear if the effective strain values were within the steady state regime. However, it is possible to evaluate the deformation microstructures using hardness comparisons. If it were assumed that the total change in hardness (deformed less fully recrystallized hardness) is related to the total reduction in stored energy, it would be expected that for specimens deformed in the steady state regime that the results would be approximately equal. Table 4.4 presents the results for the change in hardness for Z1 and Z2 deformed specimens annealed at 800^0C.

Strain	Total Hardness Change – Z1	Total Hardness Change – Z2
0.52	64	30
0.85	75	40
1.25	89	40

Table 4.4: Determination of total stored energy reduction, during annealing at 800^0C for Z1 and Z2 deformation conditions, in terms of hardness changes.

Table 4.4 shows that the hardness change for Z2 specimens does not increase incrementally with respect to strain. For comparative purposes the hardness change associated with Z1 specimens, not deformed within the steady state regime, show an increase with a rise in strain. The results presented in table 4.4 provide further evidence that Z2 specimens were deformed within the steady state regime.

4.5.4 Stored Energy Relationship

Deformation within the steady state regime, for Z2 deformed specimens, would explain the small difference in $t_{0.5}$ values with increasing strain. However, it would still be expected that the $t_{0.5}$ values would be higher than those for specimens deformed at Z1; the stored energy in Z2 deformed specimens is lower than Z1

specimens. Associated with deformation in the steady state regime, for Z2 specimens, would be dynamic and metadynamic recrystallization phenomenon. Although the occurrence of dynamic recrystallization would be expected to decrease the stored energy and thus the driving force following deformation, nuclei formed during the rolling period would be present in the microstructure at the commencement of the static period i.e. metadynamic recrystallization. Therefore, during annealing treatments, the incubation period would be avoided and the nuclei formed during deformation would continue to grow. The absence of the nucleation period would reduce the $t_{0.5}$ considerably and adversely affect Avrami results. A schematic showing the effect of the incubation period on $t_{0.5}$ is shown in figure 4.42.

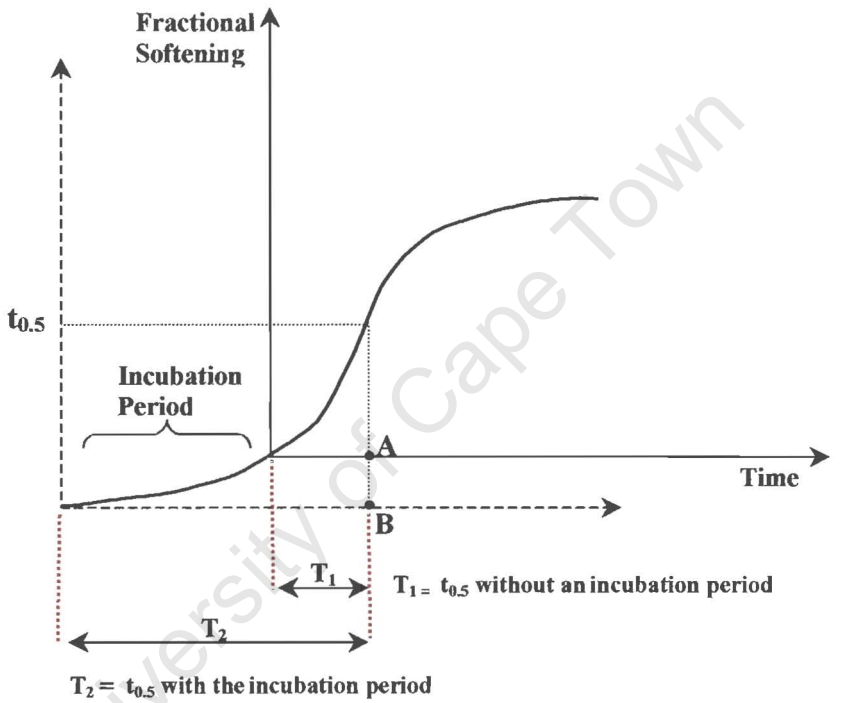

Figure 4.42: Schematic showing the effect of the incubation period on $t_{0.5}$

A comparison of Z1 and Z2 deformation microstructures are shown in figures 4.43 and 4.44 for specimens strained to 0.52 and 1.25 respectively. The deformed microstructures have significantly different appearances. The specimen deformed at Z1, figure 4.43a, is heavily deformed. However, for the specimen deformed at Z2, figure 4.43b, there are recrystallized regions. A similar phenomenon is illustrated in figure 4.44a-b for specimens strained to 1.25. These results suggest that dynamic recrystallization had occurred in specimens deformed at the higher temperature. It would therefore be expected that metadynamic recrystallization was present following deformation, as dynamic recrystallization nuclei would be present in the material.

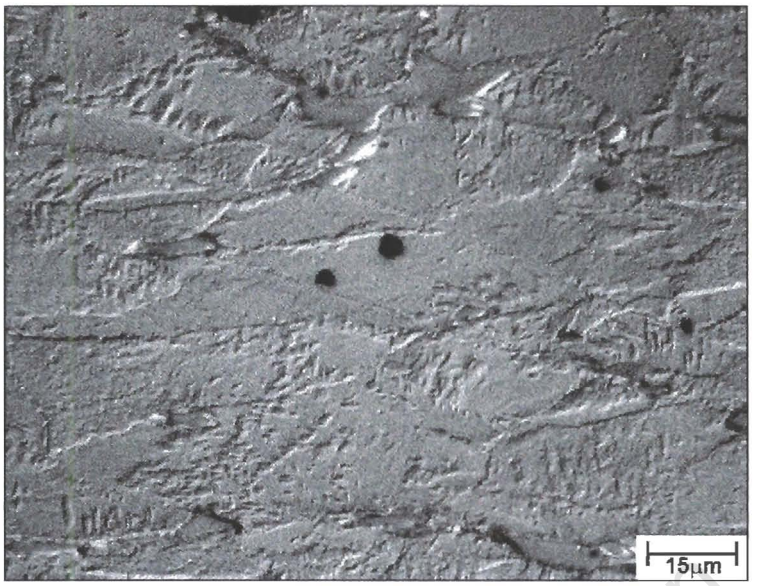

(a)

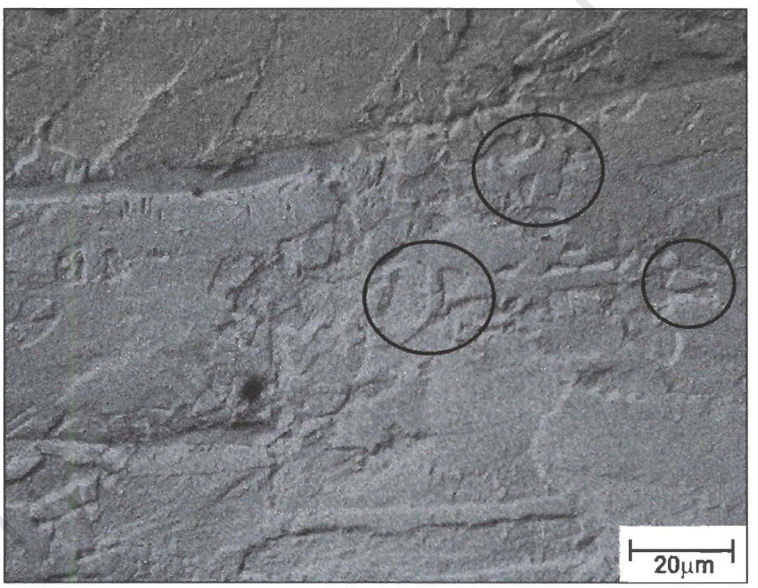

(b)

Figure 4.43: **A comparison of the as deformed microstructures for specimens strained to 0.52 and deformed at (a) Z1 and (b) Z2. The circled regions show an area of undeformed grains. This suggests that dynamic recrystallization has occurred and/or grain growth following deformation has taken place.**

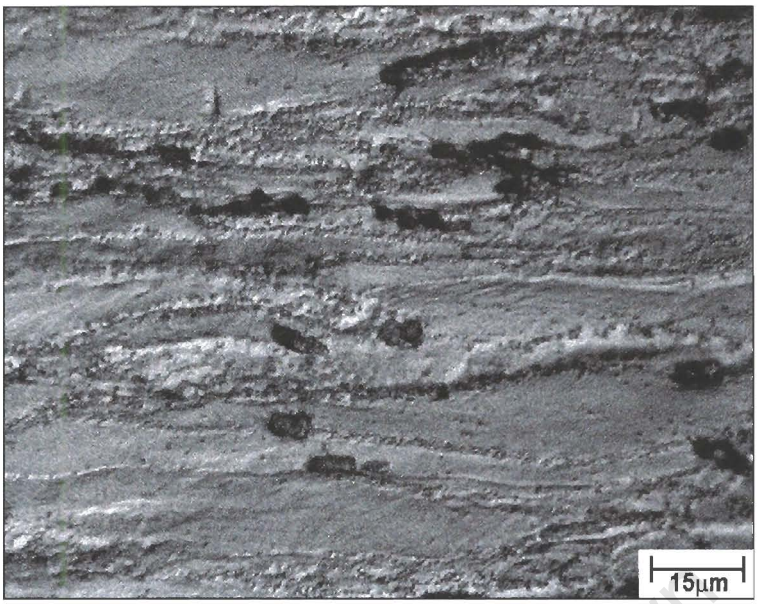

(a)

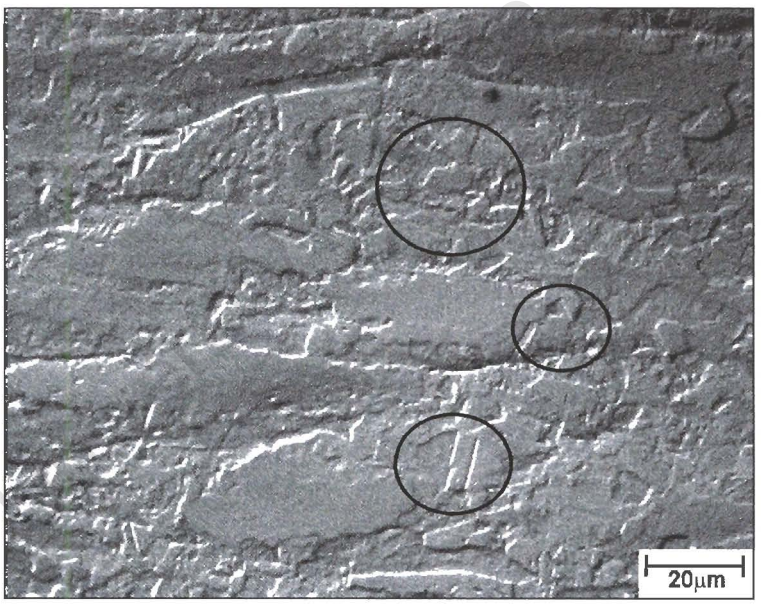

(b)

Figure 4.44: **A comparison of the as deformed microstructures for specimens strained to 1.25 and deformed at (a) Z1 and (b) Z2. Circled areas show recrystallized grains.**

4.5.5 Recrystallized Grains in Deformed Microstructure

EBSD maps, figures 4.45 to 4.48, were obtained to compare the deformed microstructures. It is evident from the EBSD maps for specimens deformed at 950^0C, figures 4.46 and 4.48 that there are areas of recrystallized grains.

It would be expected that dynamic recrystallized grains, figures 4.46 and 4.48, would contain some deformity; concurrent straining behind the migrating grain boundary would induce dislocations. Metadynamic nuclei would also be smaller in size than those appearing on the EBSD maps. This phenomenon suggests that growth of nuclei and/or previous dynamic recrystallized grains occurred in the short interval between deformation and quenching. For specimens deformed at the higher temperature of 950^0C the kinetics of recrystallization would be extremely rapid and it is possible that the time interval between deformation, in the Gleeble 1500, and quenching to a stable temperature could be sufficient to cause recrystallization. An appreciation of the recrystallization kinetics at a temperature of 900^0C are shown in figure 4.41 and it can be deduced that kinetics in the temperature regime are rapid; $t_{0.5}$ for specimens strained to 1.25 was 15 seconds. Therefore, at a temperature of 950^0C the kinetics would be considerably quicker, suggesting that 2 to 3 seconds could result in growth of nuclei immediately following deformation and effect subsequent annealing behaviour. The EBSD maps attained for the specimens deformed at Z1 and Z2, to compare the as deformed microstructures, enabled the recrystallized fraction to be calculated and the results are presented in table 4.5.

Strain	Percentage recrystallized for as deformed specimens– Z1	Percentage recrystallized for as deformed specimens– Z2
0.52	25	36
0.85	20	50
1.25	17	35

Table 4.5: A comparison of the as deformed recrystallized fractions, for specimens deformed at Z1 and Z2, obtained from EBSD analysis.

The method used in the VMAP software to calculate the volume fraction recrystallized will undoubtedly contain some errors due to the assumptions that are made in the program. Therefore, the values given in table 4.5 should not be interpreted as definitive values but rather from a comparative perspective. By

keeping all the parameters consistent when calculating the volume fraction recrystallized from EBSD software, important comparisons can be made between the as deformed microstructures. From table 4.5 it is evident that the specimens deformed at the higher temperature, Z2, have a higher as deformed recrystallization fraction. As has been mentioned it is not proposed that these are definitive values but it does suggest that the deformed microstructures contain greater areas of recrystallized regions in comparison to Z1. Figures 4.46 and 4.48 show grains within the deformed microstructure for Z2 specimens that have recrystallized. There is very little evidence of recrystallized grains in the specimens deformed at Z1 (see figures 4.45 and 4.47).

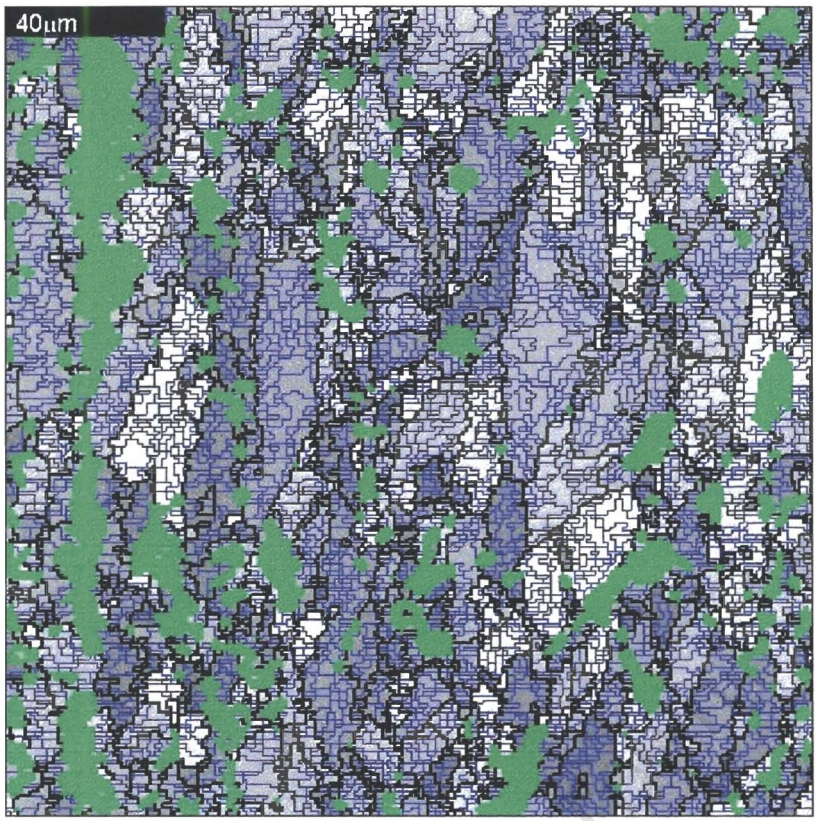

Figure 4.45: **Microstructure of deformed specimen strained to 0.52 and deformed at Z1. Green areas are non-indexed regions.**

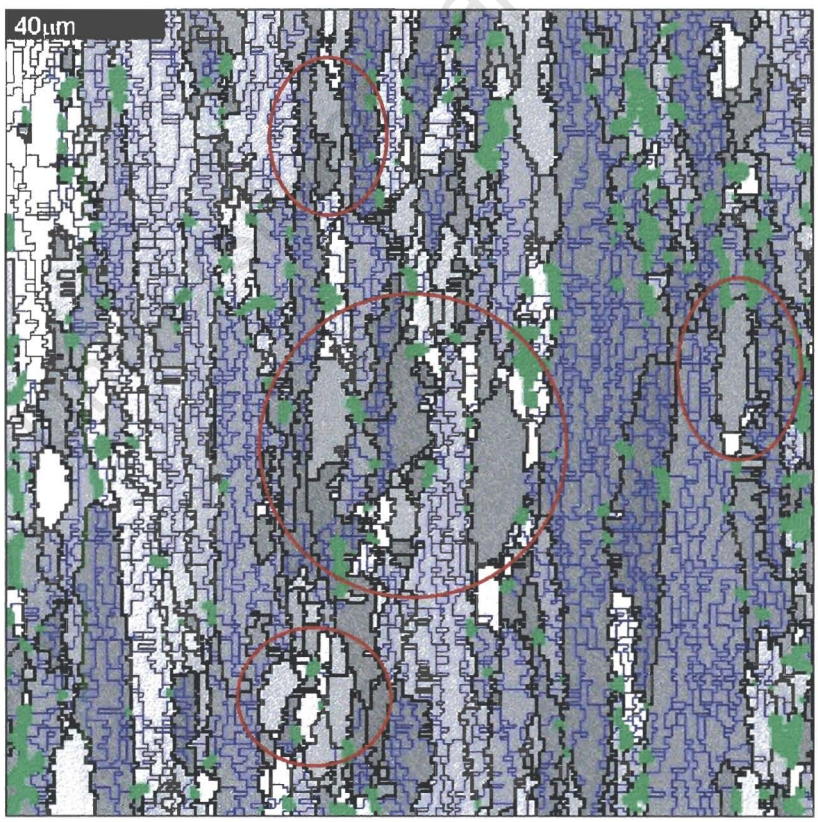

Figure 4.46: **Microstructure of deformed specimen strained to 0.52 and deformed at Z2. Circled areas show recrystallized grains.**

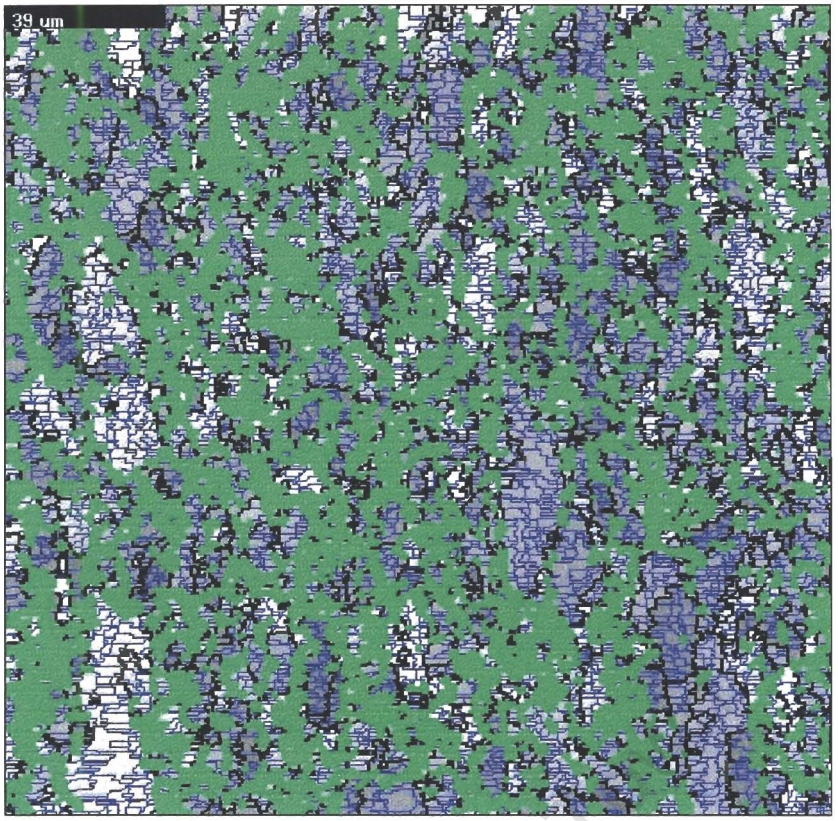

Figure 4.47: **Microstructure of deformed specimen strained to 0.85 and deformed at Z1. Green areas are non-indexed regions.**

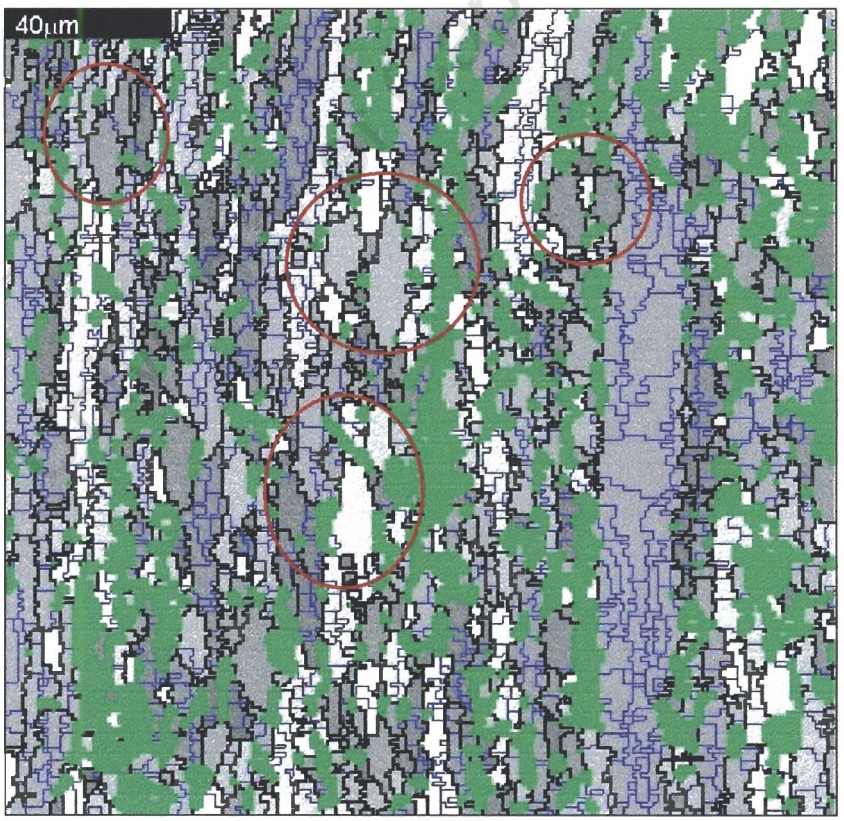

Figure 4.48: **Microstructure of deformed specimen strained to 0.85 and deformed at Z2. Circled areas show recrystallized grains.**

4.5.6 Z2 relationship at 900^0C

The relationship between $t_{0.5}$ and strain for specimens annealed at 900^0C is shown in figure 4.41. Specimens deformed at Z2, annealed at 900^0C, would be expected to exhibit similar characteristics as those specimens annealed at 800^0C due to deformation occurring in the steady state regime. However, it is evident from figure 4.41 that the relationship is contrary to expected results; $t_{0.5}$ values are higher than for the Z1 deformation condition and they also decrease as strain increases.

It has already been mentioned (section 4.2.1) that softening kinetics are rapid during annealing at 900^0C. The $t_{0.5}$ values, figure 4.41, are consequently short for both Z1 and Z2 deformed specimens. The method used to derive the $t_{0.5}$ values were based on certain assumptions, namely:

- Restoration of hardness is equivalent to fraction recrystallized.
- The final hardness value, H_f, in equation 3.5 is measured using an extrapolation process.
- The value of $t_{0.5}$ is obtained from a best-fit relationship.

These assumptions are satisfactory when describing the annealing kinetics in which there is a significant $t_{0.5}$ distinction between the different experimental strains.

However, for instances when the recrystallization kinetics are rapid a small error in the calculation process to determine $t_{0.5}$ will be significant. From figure 4.41, for Z2 deformation conditions, a time of only 7 seconds separates the $t_{0.5}$ values for specimens strained to 1.25 and 0.85. For the Z1 condition, there is only 3 seconds separating the $t_{0.5}$ value for 0.52 and 0.85 strained specimens. Therefore, it is not feasible to accurately quantify the kinetics for instances when 5 to 10 seconds significantly affects the results. It is evident that the results in figure 4.41 should be used with discretion when quantifying kinetics.

4.6 Determining the Strain Exponent

4.6.1 Introduction

Further evidence of the sensitivity of $t_{0.5}$ at high annealing temperatures is illustrated in the straight-line graphs of log $t_{0.5}$ versus log ε. The exponent of strain in the $t_{0.5}$ equation is determined from the gradient of the straight-line graphs. The behaviour of the specimens deformed at Z2 prevented a reliable exponent of strain to be determined. Therefore, the results presented in figure 4.49 exclude the data for this condition.

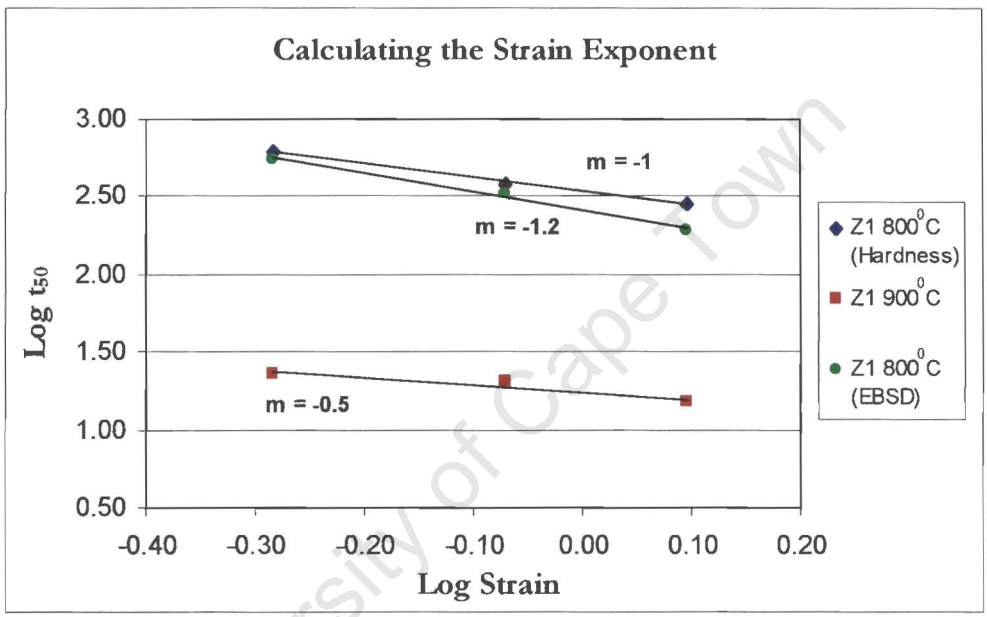

Figure 4.49: Graphical representation of the method used to calculate the strain exponent for the $t_{0.5}$ equation. The strain exponent has also been determined from EBSD data for comparative purposes.

4.6.2 Strain Exponent Dependence on $t_{0.5}$

Ideally, the strain exponent should be equal, or within experimental error, for each condition shown in figure 4.49. If it were assumed that the EBSD data (obtained from specimens deformed at Z1 and annealed at 800^0C) is accurate, then –1.2 would be the correct strain exponent. Calculating the strain exponent from softening curves, for the same specimens that the results for EBSD were obtained, gives a value of –1. These two values are within experimental error, as would be expected due to the fact that the graphs illustrating the relationship between fractional softening and

recrystallization are well correlated for this condition (see figures 4.32 to 4.34). However, it is evident from figure 4.49 that there is a significant deviation in the strain exponent results for Z1 specimens annealed at 900^0C. For rapid recrystallization kinetics the strain exponent is sensitive to small changes in $t_{0.5}$. It has already been mentioned that for specimens annealed at 900^0C the recrystallization rates were rapid and thus complicated the method of acquiring accurate $t_{0.5}$ data. The $t_{0.5}$ values ranged from 15 seconds, for the highest strained specimen, to 26 seconds for the lowest (specimens deformed at Z1). A change of two seconds, for example, in the specimen strained to 1.25 would lower the strain exponent by 0.15, from –0.5 to –0.35. It is evident that a high degree of accuracy is required for specimens annealed at 900^0C as a difference in one second can have a significant effect. The $t_{0.5}$ values for the specimens annealed at Z1 and annealed at 800^0C are comparatively higher and therefore have less effect on strain exponent results. A change of over 40 seconds in the $t_{0.5}$ value is required in this case to cause a change of 0.15 in the strain exponent.

4.6.3 Industrial Solution

From the results presented in figure 4.49 there is insufficient data to derive a common strain exponent value for the conditions used in this study. The complex nature of the deformation and annealing phenomena prevented a reliable empirical relationship to be established based on the Avrami approach. Deformation within the steady state regime and rapid recrystallization kinetics were particularly limiting to the determination of an accurate strain exponent.

There are shortcomings of the Avrami approach in predicting microstructural evolution, evident from results presented in this study. Thus it is not reasonable to expect that a single equation is able to predict microstructural behaviour for any deformation and annealing conditions experienced in the rolling application. The Avrami equation will incorrectly predict behaviour when deformation occurred in the steady state regime. The equation will predict a reduction in the time for complete recrystallization as the strain increases, however, in reality there is no change in the recrystallization time with an increase in strain for deformation within the steady state regime. For rapid recrystallization kinetics it is not feasible to accurately describe the recrystallization behaviour and therefore it is difficult to validate the results for this condition. Based on these facts it is suggested that the Avrami approach to modelling

needs to be considered from a less rigid perspective of a single equation describing complete microstructural behaviour during a rolling application.

From an industrial perspective, there needs to be an understanding between the mill operator and the information provided by the metallurgist. The mill operator is principally concerned with microstructural evolution in the interpass period and the final microstructural conditions after rolling is completed. For rapid recrystallization kinetics, which are difficult to model, the interpass time may be considerably longer than the time taken for complete recrystallization. Therefore, it would be sufficient for the mill operator to know that recrystallization will be complete within the interpass time.

A similar approach would need to be applied for instances when deformation occurs within the steady state regime. For a material deformed within the steady state, the kinetics should be approximately equal during annealing at a specific temperature. Thus, an extensive experimental matrix would need to be developed that describes steady state annealing behaviour for all deformation conditions and annealing temperatures encountered during the industrial rolling schedule.

Despite the inability in this study to determine a reliable strain exponent that can be universally applied, the detailed microstructural evolution that can be obtained from the current approach is helpful to mill operators and metallurgists involved with development work. Although it is deemed that the capability of predicting microstructural development is limited, more explicit knowledge of the material behaviour during rolling is invaluable to mill operators.

4.6.4 Alternative Approach

Based on the above suggestions, the constants in the various equations (for those regimes that are able to be modelled according to the Avrami equation) need to be considered specific to a particular deformation regime and process. Using this approach there will not be definite material constants but particular material, process and deformation condition constants i.e. for deformation at Z1 the exponents will be different for Z2 conditions. This approach implies that it is not possible to predict

microstructural evolution from a single equation, but rather from multiple equations describing specific regimes.

It should also be noted that the input variables, such as temperature, strain and strain rate, are directly related to the accuracy of a predictive model. Thus, it is not feasible to implement a predictive model without comprehensive data feedback from the material that is being rolled.

There have been attempts to improve upon the Avrami approach using more detailed microstructural models[59, 60]. However, these models have focussed on a very small scale (over 5 to 10 grains) to explain microstructural evolution. The models are based on manually counting dislocations, relating this information to stored energy values and predicting grain growth based on stored energy in neighbouring grains. However, it is unreasonable to model large scale rolling procedures on such a fine scale. Thus, the Avrami approach is more applicable to large scale applications, but it has to be accepted that there will be certain shortcomings that will need to be accounted for in the predictions.

Chapter 5

Conclusions

Specimens have been deformed to simulate industrial rolling mill conditions in an attempt to establish a methodology for microstructural prediction. This chapter summarises the major findings and the conclusions that can be made from this study.

The difficulty in identifying recrystallized grains was considerably improved by using EBSD. Visual identification was somewhat useful, however, it is not possible to determine the extent of deformation within a grain. EBSD was able to identify recrystallized grains within the deformed microstructure, which was useful in providing evidence of recrystallization occurring in the time period between deformation and quenching to a stable temperature. In specimens that dynamically recrystallized it would have been difficult to visually identify the difference between dynamically recrystallized grains and those grains that recrystallized during the quenching period. Dynamic recrystallized grains would have contained some deformity that would have been difficult to visually identify; however, EBSD was able to show that there were certain recrystallized grains that were completely strain free. It therefore, might not have been possible, without EBSD, to deduce that recrystallization had taken place during the quenching period in this instance.

The EBSD software, which provides recrystallized fraction data, should be used with discretion. The software uses certain assumptions that can over or under estimate actual recrystallization fractions; results should be used with caution when quoting specific recrystallized values. However, it is beneficial to use the software data from a comparison perspective, but the boundary conditions must remain constant for each map.

Hardness restoration and fraction recrystallized were well correlated for the specimens that were examined. This relationship can only be extended for other conditions provided that no prior dynamic or metadynamic events have distorted the deformed microstructures. This follows from the fact that the deformed

microstructure is of significant importance when modelling static recrystallization behaviour. The annealing response is directly related to the deformed microstructure and thus requires careful consideration.

The recrystallization kinetics are rapid for annealing temperatures of 900^0C. The $t_{0.5}$ values are consequently short and difficult to determine. It is not feasible from an industrial perspective to accurately model the kinetics for temperatures in this regime as a factor of 1 to 2 seconds can significantly alter the results. It is sufficient for the mill operator to know that recrystallization will be complete within a short time period.

Deformation within the steady state regime limits the applicability of the Avrami equation. However, all specimens strained within the steady state regime will have approximately equal softening kinetics during the annealing interval. Thus it is possible for a computer model to have a routine that takes into account recrystallization kinetics for specific steady state deformation conditions annealed at a particular temperature. This would require extensive experimental work to consider all steady state deformation conditions and annealing temperatures encountered in the industrial hot rolling application.

The Avrami approach contributes to an improved understanding of a materials annealing response following deformation. However, it is not possible to model all annealing phenomena during an industrial process based simply on a single equation. The material dependent constants will vary for particular deformation conditions and annealing events. Thus a combination of equation would be required, coupled with sub-routines that would predict annealing behaviour for conditions that could not be modelled using an empirical relationship.

Chapter 6

Future Work

The following suggestions are made to facilitate future work involving microstructural predictive studies based on the Avrami approach.

- The deformation matrix should resemble the conditions expected during the industrial rolling application.

- EBSD analysis should be performed on all as-deformed specimens to glean a complete understanding of the deformed microstructures. The annealing response is directly related to the deformed state and thus requires detailed analysis.

- An understanding between the mill operator and metallurgist is required to develop a predictive approach that is feasible for industrial applications.

- Steady state deformation regimes need to be identified prior to performing extensive annealing treatments i.e. it not necessary to perform annealing treatments on specimens strained to three or four different strain values if they were all deformed within the steady state regime. The recrystallization response will be similar for each strain in this instance.

- For annealing conditions that result in rapid recrystallization kinetics (recrystallization completed in 0-30 seconds) it is not necessary to perform extensive experiments to accurately describe the microstructural behaviour. In such instances, it would be sufficient to identify the annealing conditions that result in rapid recrystallization kinetics and report that recrystallization occurs rapidly and within the interpass time encountered during the industrial rolling application.

References

[1] **Stainless Steels**, edited by P. Lacombe, B. Baroux and G. Beranger, Les Editions de Physique Les Ulis, France, 1993.

[2] F.B. Pickering, **Relationship between Microstructure and Properties in Stainless Steels**, Micon 78: Optimization of Processing, Properties and Service Performance Through Microstructural Control, ASTM, 1969, p. 263.

[3] P. Marshall, **Austenitic Stainless Steels – Microstructure and Mechanical Properties**, Elsevier Applied Science Publishers, England, 1984.

[4] **Stainless Steels – ASM Speciality Handbook**, edited by J.R. Davies, International Handbook Committee, American Society for Metals, 1994.

[5] F.B. Pickering, **The Metallurgical Evolution of Stainless Steel**, ASM and the Metals Society, U.S.A., 1969.

[6] C.L. Cole and J.D. Jones, **Stress Relief of Austenitic Stainless Steels**, Stainless Steels, Iron and Steel Institute, England, 1968.

[7] R. Honeycombe and H.K.D.H. Bhadesia, **Steels-Microstructure and Properties**, Edward Arnold Publishers, 2nd Edition, 1995.

[8] D. Peckner and I.M. Bernstein, **Handbook of Stainless Steels**, Mc-Graw Hill Inc., U.S.A., 1997.

[9] C.M. Sellars, **Modelling Microstructural Development during Hot Rolling**, Materials Science and Technology, 6, 1990, p. 1072.

[10] J.H. Beynon and C.M. Sellars, **Modelling of Plastic Deformation and its Engineering Applications**, edited by S.I. Andersen et al., Riso National Laboratory, Denmark, 1992.

[11] F.J. Humphreys & M. Hatherley, **Recrystallization and Related Annealing Phenomena**, Pergamon, Oxford, 1995.

[12] W. Roberts, H. Boden and B. Ahlblom, **Dynamic Recrystallization Kinetics**, Metal Science, 1979, p. 195.

[13] C.M. Sellars and J.A. Whiteman, **Recrystallization and Grain Growth in Hot Rolling**, Metal Science, 1979, p. 187.

[14] R.D. Doherty et al, **Current Issues in Recrystallization: a Review**, Materials Science and Engineering, A238, 1997, p. 219.

[15] Hsun Hu, B.B. Rath and R.A. Vandermeer, **An Historical Perspective and Overview of the Annealing Studies of Cold Worked Metals**, Recrystallization '90, edited by T. Chandra, The Minerals, Metals and Materials Society, U.S.A., 1990, p. 3.

[16] H.J. McQueen and J.J. Jonas, **Recovery and Recrystallization during High Temperature Deformation**, Treatise on Materials Science and Technology, Vol. 6, Plastic Deformation of Metals, edited by R.J. Arsenault, Academic Press, U.S.A., 1975, p. 393.

[17] W. Blum and H.J. McQueen, **Dynamics of Recovery and Recrystallization**, Materials Science Forum, Vol. 217-222, Transtec Publications, Switzerland, 1996, p. 31.

[18] H.J. McQueen, E. Evangelista and N.D. Ryan, **Dynamic Recrystallization and Recovery: Mechanical and Kinetic Behaviour, Nucleation and Growth Mechanisms**, Recrystallization '90, edited by T. Chandra, The Minerals, Metals and Materials Society, U.S.A., 1990, p. 89.

[19] R.W.K. Honeycombe, **Plastic Deformation of Metals**, 2nd Edition, Edward Arnold, Great Britain, 1984.

[20] P. Cotteril and P.R. Mould, **Recrystallization and Grain Growth in Metals**, Surrey University Press, Great Britain, 1976.

[21] D.T. Llewellyn, **Work Hardening Effects in Austenitic Stainless Steel**, Materials Science and Technology, Vol. 13, 1997, p. 389.

[22] L.E. Murr, **Interfacial Phenomena in Metals and Alloys**, Addison-Wesley, Reading, 1975, p. 131 (from reference 11).

[23] N.D. Ryan and H.J. McQueen, **Comparative Kocks Mecking Analysis of the Dynamic Recovery of 304 and 309**, Advances in Hot Deformation Textures and Microstructures, edited by J.J. Jonas et al, The Minerals, Metals and Materials Society, 1994, p. 445.

[24] A.A. Vieira, D.B. Santos, R.A.N.M. Barbosa, **Dynamic Recrystallization in Austenitic Stainless Steel**, Recrystallization '90, edited by T. Chandra, The Minerals, Metals & Materials Society, U.S.A., 1990, p. 295.

[25] A. Belyakov, H. Miura, T. Sakai and R. Kaibyshev, **Dynamic Recrystallization Under Warm and Hot Deformation of a 304 Stainless Steel**, The Fourth International Conference on Recrystallization and Related Phenomena, edited by T. Sakai and H.G. Suzuki, Japan Institute of Metals, 1999, p. 247.

[26] H.J. McQueen, **Initiating Nucleation of Dynamic Recrystallization**, Primarily in Polycrystals, Materials Science and Engineering A, 101, 1998, p. 149.

[27] P. Bocher and J.J. Jonas, **Characteristics of Nucleation and Growth during the Dynamic Recrystallization of a 304 Stainless Steel**, The Fourth International Conference on Recrystallization and Related Phenomena, edited by T. Sakai and H.G. Suzuki, Japan Institute of Metals, 1999, p. 25.

[28] N.D. Ryan, H.J. McQueen and E. Evangelista, **Dynamic Recovery and Strain Hardening in the Hot Deformation of Type 317 Stainless Steel**, Materials Science and Engineering, 81, 1986, p. 259.

[29] Sung-I1 Kim and Yeon-Chul Yoo, **Dynamic Recrystallization behaviour of AISI 304 Stainless Steel**, Materials Science and Engineering, A311, 2001, p. 108.

[30] M.J. Luton and C.M. Sellars, **Dynamic Recrystallization in Nickel and Nickel-Iron Alloys During High Temperature Deformation**, Acta Metallurgical, Vol.17, 1969, p. 1033.

[31] T. Sakai and J.J. Jonas, **Dynamic Recrystallization: Mechanical and Microstructural Considerations**, Overview No.35, Acta Metallurgica, Vol.32, No.2, 1984, p. 189.

[32] T. Sakai, M.G. Akben and J.J. Jonas, **Dynamic Recrystallization During the Transient Deformation of a Vanadium Microalloyed Steel**, Vol.31, No.4, 1983, p. 631.

[33] J.P. Sah, G.J. Richardson and C.M. Sellars, **Grain Size Effects During Dynamic Recrystallization of Nickel**, Metal Science, Vol.8, 1974, p. 325.

[34] N.D. Ryan, H.J. McQueen and J.J. Jonas, **The Deformation Behaviour of Type 304, 316 and 317 Austenitic Stainless Steels During Hot Torsion**, Canadian Metallurgical Quarterly, Vol.22, No.3, 1983, p. 369.

[35] R.A. Petkovic, M.J. Luton and J.J. Jonas, **Recovery and Recrystallization of Carbon Steel between Intervals of Hot Rolling**, Canadian Metallurgical Quarterly, Vol.14, No.2, 1975, p. 137.

[36] D.R. Barraclough and C.M. Sellars, **Static Recrystallization and Restoration after Hot Deformation of Type 304 Stainless Steel**, Metal Science, 1979, p. 257.

[37] D.J. Towle and T. Gladman, **Recrystallization of Austenitic Stainless Steels after Hot Rolling**, Metal Science, 1979, p. 246.

[38] A.A. Vieira, D.B. Santos, R.A.N.M. Barbosa, **Static Recrystallization after Hot Rolling of Austenitic Stainless Steels**, Recrystallization '90, edited by T. Chandra, The Minerals, Metals & Materials Society, U.S.A., 1990, p. 361.

[39] R.A.P. Djaic and J.J. Jonas, **Recrystallization of High Carbon Steel between Intervals of High Temperature Deformation**, Metallurgical Transactions, Vol.4, 1973, p. 621.

[40] M. Hatherly, **The Origin of Recrystallization Textures**, Recrystallization '90, edited by T. Chandra, The Minerals, Metals & Materials Society, U.S.A., 1990, p. 59.

[41] R.D. Doherty, **The Deformed State and Nucleation of Recrystallization**, Metal Science, Vol.8, 1974, p. 132.

[42] B. Hutchinson, **Nucleation of Recrystallization**, Scripta Metallurgica et Materialia, Vol. 27, 1992, p. 1471.

[43] F.J. Humphreys, **Recrystallization and Recovery**, Materials Science and Technology, A Comprehensive Treatment, edited by R.W. Cahn, P. Haasen and E.J. Kramer, Vol.15, 1991, p. 371.

[44] A. Laasraoui and J.J. Jonas, **Recrystallization of Austenite after Deformation at High Temperatures and Strain Rates-Analysis and Modelling**, Metallurgical Transactions A, Vol. 22A, 1991, p. 151.

[45] T. Furu, K. Marthinsen and E. Nes, **Modelling Recrystallization**, Materials Science and Technology, Vol.6, 1990, p. 1093.

[46] F.J. Humphreys, **A Network Model for Recovery and Recrystallization**, Scripta Metallurgica, Vol.27, 1992, p. 1557.

[47] R.A.N.M. Barbosa and C.M. Sellars, **Static Recrystallization of Type 316L Stainless Steel Under Hot Working Conditions**, Materials Science Forum, Vols. 113-115, 1993, p. 461.

[48] N.D. Ryan and H.J. McQueen, **Comparison of Static Softening in 300 Series Stainless Steels Under Iso- and Anisothermal Conditions**, Materials Science and Technology, Vol.7, 1991, p. 818.

[49] N.D. Ryan, E. Evangelista and H.J. McQueen, **Static Recrystallization Associated with Hot Working of Austenitic Stainless Steels**, Materials Science Forum, Vols. 113-115, 1993, p. 515.

[50] L.P. Karjalainen, J. Perttula and P. Kantanen, **Modelling of Multipass Hot Rolling Constitutive Equations and Softening Behaviour of Steels**, Proc. of the General Cost 512 Workshop on Modelling in Materials Science and Processing, Switzerland, 1996, p. 193.

[51] P. Fabregue, J.Tormo, P. Choquet and B.J. Thomas, **Microstructural Evolution of Austenitic Stainless Steels During Hot Rolling**, Proc. of Int. Conf. on Stainless Steels, Chiba, ISIJ, 1991, p. 494.

[52] S. Kikuchi, **Diffraction of Cathode Rays by Mica**, Imp. Acad, Tokyo, Proc., Vol.4, 1928, p. 271.

[53] J.A. Venables, C.J. Harland, **Electron Backscattering Patterns – A New Technique for Obtaining Crystallographic Information in the Scanning Electron Microscope**, Philos. Mag. 27, 1973, p.1193.

[54] V. Randle, **Microtexture Determination and its Applications**, Institute of Metals, Great Britain, 1992.

[55] D.P. Field, **Quantification of Partially Recrystallized Polycrystals using Electron Backscatter Diffraction**, Materials Science and Engineering A190, 1995, p. 241.

[56] M.P. Black & R.L. Higginson, **An Investigation into the use of EBSD to Measure Recrystallized Fraction**, Scripta Materialia, Vol.4, No.2, 1999, p. 125.

[57] N.C. Krieger Laasen, **Automatic Recognition of Recrystallized Grains in Partially Recrystallized Samples from Crystal Orientation Maps**, Proc. of the 12th International Conference on Texture of Materials, 1999, p. 854.

[58] G. Floweday, MSc Thesis, University of Cape Town, 2001.

[59] F.J. Humphreys, **Modelling Microstructural Evolution during Annealing**, Materials Science and Engineering, Vol. 8, 2000, p. 893.

[60] F.J. Humphreys and P.J. Hurley, **Modelling Recrystallization – Questions of Size and Scale**, Recrystallization and Grain Growth, Proc. of the First Joint International Conference, editors G. Gottstein and D.A. Molodov, 2001, p. 683.

Appendix A

Reference	Pass	Location (m)	Time (s)	Entry Temp(^{0}C)	Exit Temp (^{0}C)	Entry Gauge (mm)	Exit Gauge (mm)	Strain	Strain Rate (s^{-1})	Interpass Time (s)
A1	1	1.84	0.7	715.5	940.2	23.4	16.7	0.388	17.08	
A2	1	8.24	3.5	957.4	966.0	23.4	16.8	0.382	17.20	
A3	1	11.63	4.9	967.0	966.0	23.4	16.9	0.376	16.87	
A4	1	19.30	7.4	964.0	959.5	23.5	17.0	0.372	29.95	
A5	1	27.24	9.3	964.0	964.4	23.6	17.2	0.365	30.35	
A6	1	36.65	11.5	959.6	962.0	23.7	17.2	0.368	30.31	
A7	1	44.11	13.3	960.0	965.0	23.6	17.1	0.370	26.35	
A8	1	53.24	16.0	957.0	960.0	23.6	17.2	0.367	23.41	
A9	1	61.92	18.7	954.0	949.0	23.7	17.2	0.369	23.51	
A10	1	70.43	21.3	945.0	944.0	23.8	17.3	0.369	23.45	
A11	1	78.95	23.7	944.0	947.0	23.7	17.2	0.366	23.45	
A12	1	87.50	26.3	935.0	941.9	23.6	17.2	0.367	23.47	
A13	1	96.06	29.5	925.7	960.0	23.6	17.2	0.367	11.97	
A14	1	97.38	30.5	924.0	960.0	23.4	17.1	0.361	8.67	
A14	2	4.04	1.7	926.7	830.2	17.2	12.7	0.355	19.17	1.7
A13	2	4.04	1.7	926.7	830.2	17.2	12.7	0.355	19.17	2.7
A12	2	12.90	5.5	939.7	917.9	17.2	12.5	0.364	19.70	9.7
A11	2	23.85	8.4	947.3	938.3	17.2	12.5	0.367	35.53	15.3
A10	2	36.65	11.5	958.0	949.0	17.2	12.5	0.363	35.37	20.7
A9	2	47.74	14.1	961.0	952.0	17.1	12.5	0.364	35.59	25.9
A8	2	59.68	16.8	967.0	958.0	17.1	12.5	0.362	35.34	31.4
A7	2	70.77	19.5	971.0	961.0	17.2	12.6	0.363	35.30	36.7
A6	2	84.42	22.7	974.0	964.0	17.2	12.5	0.363	35.36	41.7
A5	2	95.51	25.3	977.0	964.0	17.2	12.6	0.359	35.07	46.5
A4	2	106.60	27.8	977.0	964.0	16.9	12.6	0.345	34.59	51.0
A3	2	117.57	30.8	977.0	963.6	17.0	12.5	0.348	21.91	56.4
A2	2	121.51	32.6	974.0	955.7	16.8	12.6	0.334	17.04	59.7
A1	2	133.69	38.7	954.0	948.0	17.0	12.6	0.350	8.70	68.5
A1	3	3.93	1.7	934.2	923.0	12.6	9.5	0.330	21.47	1.7
A2	3	16.20	6.8	940.0	936.0	12.6	9.3	0.344	28.55	12.9
A3	3	21.37	8.1	947.3	949.1	12.5	9.3	0.348	42.61	16.0
A4	3	36.27	10.6	961.7	971.0	12.5	9.2	0.350	68.38	21.5
A5	3	52.31	12.8	967.0	977.0	12.6	9.3	0.349	70.70	26.3
A6	3	67.24	14.8	971.0	977.0	12.5	9.3	0.347	70.83	30.9

Reference	Pass	Location (m)	Time (s)	Entry Temp(^{0}C)	Exit Temp (^{0}C)	Entry Gauge (mm)	Exit Gauge (mm)	Strain	Strain Rate (s^{-1})	Interpass Time (s)
A7	3	83.65	17.0	971.0	977.0	12.5	9.2	0.347	70.79	36.3
A8	3	100.07	19.2	970.6	973.0	12.5	9.3	0.344	70.27	41.1
A9	3	114.99	21.2	965.0	970.0	12.5	9.3	0.343	70.22	45.9
A10	3	131.40	23.4	961.0	964.0	12.5	9.3	0.344	70.21	50.7
A11	3	148.75	25.9	955.0	957.0	12.5	9.3	0.349	56.17	56.2
A12	3	162.73	29.0	944.4	938.0	12.5	9.3	0.345	31.61	62.2
A13	3	179.48	36.5	901.0	889.1	12.9	9.4	0.374	20.72	73.5
A14	3	181.61	37.8	893.3	902.0	12.9	9.4	0.374	11.11	74.8
A14	4	3.80	1.8	878.1	776.5	9.4	7.4	0.277	22.55	1.8
A13	4	3.80	1.8	878.1	776.5	9.4	7.4	0.277	22.55	3.1
A12	4	20.83	8.0	910.2	891.1	9.3	7.2	0.293	46.59	16.8
A11	4	42.27	11.3	947.8	936.0	9.2	7.3	0.275	79.47	23.2
A10	4	61.62	13.4	961.0	951.0	9.2	7.3	0.268	99.45	27.8
A9	4	84.63	15.6	967.0	960.9	9.3	7.4	0.263	100.46	32.2
A8	4	101.47	17.2	970.0	963.9	9.2	7.3	0.265	101.02	35.8
A7	4	122.51	19.2	973.0	968.0	9.3	7.3	0.269	101.59	40.0
A6	4	145.66	21.4	976.0	971.0	9.3	7.3	0.268	101.51	44.4
A5	4	162.40	23.0	976.0	971.0	9.2	7.4	0.256	92.04	48.0
A4	4	185.71	25.7	973.0	966.4	9.2	7.4	0.261	71.19	52.9
A3	4	201.01	28.1	962.0	951.6	9.2	7.4	0.257	52.00	57.8
A2	4	209.59	30.0	943.7	936.4	9.3	7.4	0.256	37.11	61.0
A1	4	229.98	39.1	894.2	892.0	9.6	7.5	0.297	10.78	75.3
A1	5	3.24	1.3	847.4	815.4	7.4	6.2	0.204	21.44	1.3
A2	5	23.72	8.0	883.2	903.3	7.4	6.1	0.232	52.09	17.2
A3	5	31.83	9.6	881.0	917.4	7.5	6.1	0.242	53.31	20.6
A4	5	51.63	13.4	887.7	939.7	7.3	6.1	0.201	48.87	26.8
A5	5	75.59	18.0	937.7	951.0	7.3	6.1	0.201	48.78	34.1
A6	5	97.47	22.2	894.8	955.0	7.3	6.1	0.203	48.93	39.9
A7	5	121.68	26.6	914.0	958.0	7.3	6.2	0.192	57.69	46.6
A8	5	145.88	29.9	956.5	961.0	7.3	6.2	0.197	72.25	51.9
A9	5	169.32	32.9	962.0	961.0	7.3	6.2	0.200	72.83	56.5
A10	5	191.20	35.7	962.0	955.0	7.3	6.1	0.203	73.43	61.4
A11	5	216.20	38.9	955.0	948.0	7.3	6.2	0.193	71.74	66.7
A12	5	239.67	41.9	938.4	922.3	7.3	6.1	0.192	66.93	73.1
A13	5	261.63	46.4	895.8	865.7	7.3	6.2	0.192	23.42	83.8
A14	5	264.33	47.7	888.0	854.6	7.3	6.2	0.186	18.73	85.1